

Experimental Biology and Medicine

Chief Editor

Steven Richard Goodman

University of Tennessee
Health Science Center,
Memphis, USA



SEBM Executive Council

PRESIDENT

Stephiana Cormier '26
Louisiana State University, USA

PRESIDENT ELECT

Micheal Lehman '26
Kent State University, USA

PAST-PRESIDENT

Thomas Thompson '25
University of Cincinnati College of Medicine

TREASURER

Holly A. LaVoie '24
University of South Carolina
School of Medicine

TREASURER-ELECT

Jian Feng '24
State University of New York at
Buffal

Publication Committee

Robert T Mallet '25, Chairperson
Stephanie A Cormier '24,
Muriel Lambert '25,
Aleksander F Sikorski '24

Society for Experimental Biology and Medicine
3220 N Street NW, #179
Washington DC 20007, USA
Executive Director – ed@sebm.org
Editor-in-Chief – ebm@sebm.org

www.sebm.org

Editorial Board

EDITOR-IN-CHIEF

Steven Richard Goodman
University of Tennessee Health Science Center

DEPUTY EDITOR

Nicola Conran
University of Campinas

GLOBAL EDITORS

Africa

Gordon Awandare
University of Ghana

Asia

Shaw-Jeng Tsai
National Cheng Kung University

Europe

Farzin Farzaneh
King's College London

Latin America

Nicola Conran
University of Campinas

Australia/Oceania

Sulev Kõks
Murdoch University

Anatomy/Pathology

Associate Editor

Ian Zagon
Penn State University College of Medicine

William Banks
Alexander V. Ljubimov

Patricia J. McLaughlin
Artur Pasternak

Biomedical Engineering

Associate Editor

F. Kurtis Kasper
University of Texas Health Science Center at
Houston

Angela Pannier

Artificial Intelligence/Machine Learning Applications to Biomedical Research

Associate Editor

Huixiao Hong
US Food and Drug Administration

Xiaohui Fan
Ping Gong
Ruili Huang
Fred Prior

Paul Rogers
Tielu Shi
Wenming Xiao

Bionanoscience

Associate Editor

Juan Melendez
University of Albany

Nathaniel Cady
Hassan A. Elfawal
Jonathan F. Lovell
Ya-Ping Sun

Maria Tomassone
Siyang Zheng

Biochemistry and Molecular Biology

Associate Editor

Muriel A. Lambert
Rutgers New Jersey Medical School

Brian D. Adams
Bin Guo

J. Patrick O'Connor

Cell and Developmental Biology

Associate Editor

Leszek Kotula
SUNY Upstate Medical University

David Dean
Harold I. Saavedra

Yigang Wang
Warren Zimmer

Bioimaging

Associate Editor

Shuliang Jiao
Florida International University

Kamran Avanaki
Zygmunt Gryczynski
Xinmai Yang

Xincheng Yao
Baohong Yuan
Weizhao Zhao

Clinical Trials

Associate Editor

Giuseppe Pizzorno
University of Tennessee Health Science
Center/Erlanger Health System

Daniel Vaena

Endocrinology and Nutrition

Associate Editor

Nancy D. Turner
Michigan State University

Clinton Allred
Demin Cai
Sam Dagogo-Jack
Weiqun Wang

Malcolm Watford
Chia-Shan Wu

Environmental Health/Biomarkers/Precision Medicine

Associate Editor

William Slikker, Jr.
Retired

Gary Steven Friedman
Donald Johann
Igor Pogribny

Genomics, Proteomics, and Bioinformatics

Associate Editor

Sulev Kõks
Murdoch University

Mark Geraci
Paul Potter

John P Quinn
Giovanni Stracquandano

Immunology/Microbiology/Virology

Associate Editor

Flávio Guimarães Da Fonseca
Federal University of Minas Gerais

Andrea Doria
Farzin Farzaneh

Kam Hui
Francois Villinger

Mechanisms of Aging

Associate Editor

Shigemi Matsuyama
Case Western Reserve University

Ricki Colman
Aolin Allen Hsu
Akihiro Ikeda

Masaru Miyagi
Vincent Monnier

Neuroscience

Associate Editor

Michael Neal Lehman
Kent State University

Lique M. Coolen
Terrence Deak
Max L Fletcher

Sandra Mooney
Gregg Stanwood
Richard M Xu

Pharmacology/Toxicology

Associate Editor

Santosh Kumar
University of Tennessee Health Science Center

Guzel Bikbova
Pawel Brzuzan
Laetitia Dou
Jianxiong Jiang
Youngmi Jung
Li-Fu Li

Jonathan Shannahan
Manish Tripathi
Chaowu Xiao
Wuxiang Xie
Qihe Xu

Physiology and Pathophysiology

Associate Editor

Robert T. Mallet
University of North Texas Health Science Center

Rong Ma
Gabor Tigyi
Shaw-Jenq Tsai

Samuel Verges
Lei Xi
Chunyu Zeng

Population Health

Associate Editor

Ashish Joshi
School of Public Health, University of Memphis

Stem Cell Biology

Associate Editor

Jian Feng
State University of New York at Buffalo

Vania Broccoli
Jose Cibelli
Guoping Fan

Antonis Hatzopoulos
Dan S. Kaufman
Chun-Li Zhang

Structural Biology

Associate Editor

Tom Thompson
University of Cincinnati

Andrew P. Hinck
James Horn
Rhett Kovall

Vincent Luca
Rick Page

Synthetic Biology

Associate Editor

Tara Deans
University of Utah

Ahmad Khalil
Aditya M. Kunjapur
Kevin Solomon

Systems Biology and Microphysiological Systems

Associate Editor

Andre Levchenko
Yale University

Salman Khetani
Deok-Ho Kim

Translational Research

Associate Editor

Chia-Ching (Josh) Wu
National Cheng Kung University

Jing An
Hyacinth Idu Hyacinth
Monica M. Jablonski

Chulso Moon
Esther Obeng
Athena Starland-Davenport

EBM eBook Copyright Statement

The copyright in the text of individual articles in this eBook is the property of their respective authors or their respective institutions or funders. The copyright in graphics and images within each article may be subject to copyright of other parties. In both cases this is subject to a license granted to Frontiers.

The compilation of articles constituting this eBook is the property of Frontiers.

Each article within this eBook, and the eBook itself, are published under the most recent version of the Creative Commons CC-BY licence. The version current at the date of publication of this eBook is CC-BY 4.0. If the CC-BY licence is updated, the licence granted by Frontiers is automatically updated to the new version.

When exercising any right under the CC-BY licence, Frontiers must be attributed as the original publisher of the article or eBook, as applicable.

Authors have the responsibility of ensuring that any graphics or other materials which are the property of others may be included in the CC-BY licence, but this should be checked before relying on the CC-BY licence to reproduce those materials. Any copyright notices relating to those materials must be complied with.

Copyright and source acknowledgement notices may not be removed and must be displayed in any copy, derivative work or partial copy which includes the elements in question.

All copyright, and all rights therein, are protected by national and international copyright laws. The above represents a summary only. For further information please read Frontiers' Conditions for Website Use and Copyright Statement, and the applicable CC-BY licence.

ISSN 1535-3702
ISBN 978-2-8325-4977-3
DOI 10.3389/978-2-8325-4977-3

Table of contents

Anatomy/Physiology

Feature

Original Research

- 07 **Topical naltrexone increases aquaporin 5 production in the lacrimal gland and restores tear production in diabetic rats**
David Diaz, Joseph P. Sassani, Ian S. Zagon and Patricia J. McLaughlin

Bionanoscience

Highlight

Original Research

- 17 **Internalization of transferrin-tagged *Myxococcus xanthus* encapsulins into mesenchymal stem cells**
Anna N. Gabashvili, Natalya A. Alexandrushkina, Elizaveta N. Mochalova, Daria V. Goliusova, Ekaterina N. Sapozhnikova, Pavel I. Makarevich and Petr I. Nikitin

Clinical Trials

Original Research

- 28 **Establishment and validation of a 5-factor diagnostic model for obstructive and non-obstructive azoospermia based on routine clinical parameters**
Xiaoyu Zhu, Yin Liu, Ying Huang, Hongxia Tan, Meifang He and Dong Wang

Endocrinology and Nutrition

Correction

- 37 **Corrigendum: Epigallocatechin gallate decreases plasma triglyceride, blood pressure, and serum kisspeptin in obese human subjects**
Saimai Chatree, Chantacha Sitticharoon, Pailin Maikaew, Kitchaya Pongwattanapakin, Issarawan Keadkraichaiwat, Malika Churintaraphan, Chanakarn Sripong, Rungnapa Sriwichitchai and Sompol Tapechum

Mechanisms of Aging

Correction

- 38 **Corrigendum: Quercetin suppresses ovariectomy-induced osteoporosis in rat mandibles by regulating autophagy and the NLRP3 pathway**
Yue Xiong, Cheng-Wei Huang, Chao Shi, Liang Peng, Yu-Ting Cheng, Wei Hong and Jian Liao

Original Research

41

Pharmacology and Toxicology**Cannabidiol alleviates carbon tetrachloride-induced liver fibrosis in mice by regulating NF- κ B and PPAR- α pathways**

Run Ma, Na Xie, Yuanhui Shu, Yafeng Wu, Ping He, Yining Xiang, Yan Zhou and Yuping Wang

Mini Review

53

Pharmacology and Toxicology**Highlight****Inhalation exposure-induced toxicity and disease mediated via mTOR dysregulation**

Akshada Shinde and Jonathan Shannahan

Original Research

62

Physiology and Pathophysiology**Vaporization of perfluorocarbon attenuates sea-water-drowning-induced acute lung injury by deactivating the NLRP3 inflammasomes in canines**

Cheng-Cheng Su, Zhao-Rui Zhang, Jin-Xia Liu, Ji-Guang Meng, Xiu-Qing Ma, Zhen-Fei Mo, Jia-Bo Ren, Zhi-Xin Liang, Zhen Yang, Chun-Sun Li and Liang-An Chen



OPEN ACCESS

*CORRESPONDENCE

Patricia J. McLaughlin,
✉ pxm9@psu.edu

RECEIVED 20 March 2024

ACCEPTED 19 April 2024

PUBLISHED 02 May 2024

CITATION

Diaz D, Sassani JP, Zagon IS and McLaughlin PJ (2024), Topical naltrexone increases aquaporin 5 production in the lacrimal gland and restores tear production in diabetic rats. *Exp. Biol. Med.* 249:10175. doi: 10.3389/ebm.2024.10175

COPYRIGHT

© 2024 Diaz, Sassani, Zagon and McLaughlin. This is an open-access article distributed under the terms of the [Creative Commons Attribution License \(CC BY\)](https://creativecommons.org/licenses/by/4.0/). The use, distribution or reproduction in other forums is permitted, provided the original author(s) and the copyright owner(s) are credited and that the original publication in this journal is cited, in accordance with accepted academic practice. No use, distribution or reproduction is permitted which does not comply with these terms.

Topical naltrexone increases aquaporin 5 production in the lacrimal gland and restores tear production in diabetic rats

David Diaz¹, Joseph P. Sassani², Ian S. Zagon¹ and Patricia J. McLaughlin^{1*}

¹Department of Neural and Behavioral Science, Penn State University College of Medicine, Hershey, PA, United States, ²Department of Ophthalmology, Penn State Health, Hershey, PA, United States

Abstract

Diabetes mellitus is a prevalent disease that is often accompanied by ocular surface abnormalities including delayed epithelial wound healing and decreased corneal sensitivity. The impact of diabetes on the lacrimal functional unit (LFU) and the structures responsible for maintaining tear homeostasis, is not completely known. It has been shown that the Opioid Growth Factor Receptor (OGFr), and its ligand, Opioid Growth Factor (OGF), is dysregulated in the ocular surface of diabetic rats leading to overproduction of the inhibitory growth peptide OGF. The opioid antagonist naltrexone hydrochloride (NTX) blocks the OGF-OGFr pathway, and complete blockade following systemic or topical treatment with NTX restores the rate of re-epithelialization of corneal epithelial wounds, normalizes corneal sensitivity, and reverses dry eye in diabetic animal models. These effects occur rapidly and within days of initiating treatment. The present study was designed to understand mechanisms related to the fast reversal (<5 days) of dry eye by NTX in type 1 diabetes (T1D) by investigating dysregulation of the LFU. The approach involved examination of the morphology of the LFU before and after NTX treatment. Male and female adult Sprague-Dawley rats were rendered hyperglycemic with streptozotocin, and after 6 weeks rats were considered to be a T1D model. Rats received topical NTX twice daily to one eye for 10 days. During the period of treatment, tear production and corneal sensitivity were recorded. On day 11, animals were euthanized and orbital tissues including conjunctiva, eyelids, and lacrimal glands, were removed and processed for histologic examination including immunohistochemistry. Male and female T1D rats had significantly decreased tear production and corneal insensitivity, significantly decreased number and size of lacrimal gland acini, decreased expression of aquaporin-5 (AQP5) protein and decreased goblet cell size. Thus, 10 days of NTX treatment restored tear production and corneal sensitivity to normal values, increased AQP5 expression, and restored the surface area of goblet cells to normal. NTX had no effect on the number of lacrimal gland acini or the number of conjunctival goblet cells. In summary, blockade of the OGF-OGFr pathway with NTX reversed corneal and lacrimal

gland complications and restored some components of tear homeostasis confirming the efficacy of topical NTX as a treatment for ocular defects in diabetes.

KEYWORDS

lacrimal functional unit, lacrimal glands, naltrexone, type 1 diabetes, corneal surface

Impact statement

In this study, our experiments confirmed that type 1 diabetes results in decreased tear fluid and decreased corneal sensitivity, with dysregulation in the lacrimal functional unit (i.e., decreases in lacrimal gland number and aquaporin 5 secretion, and number of conjunctival goblet cells). Topical NTX application restores tear production and corneal sensitivity, and increases the amount of aquaporin-5 expression in lacrimal gland acinar cells, but does not alter the defective morphology of the lacrimal functional unit suggesting that the rapid reversal of dry eye is related to corneal nerve sensitivity.

Introduction

More than 38 million people in the United States are diagnosed with diabetes and another 38% of the adult population in 2023 has pre-diabetes [1]. There is an increased risk for this multifactorial disease in African Americans, Hispanics, and Pacific Islanders, as well as the overall aging community [1, 2]. Despite pharmaceutical control of diabetes, nearly 50% of persons will experience at least one complication related to tear production [3, 4]. Dry eye disease (DED) is characterized as an inflammatory disorder of unknown origin, with a multifactorial etiology, which presents with persistent low tear tear-film production, increased frequency of corneal ulcerations, irritated corneal surface, and altered mucin expression [3–5]. Diabetes is also accompanied by ocular surface disease including delayed epithelial wound healing and decreased corneal sensitivity [6–8]. Previous research in the laboratory has reported that type 1 diabetic (T1D) rats have elevated serum and corneal tissue levels of this inhibitory neuropeptide called Opioid Growth Factor (OGF) [7]. Chemically termed methionine-enkephalin, OGF also has been shown to be elevated in humans with diabetes [9, 10]. Our studies have documented that OGF binds to the nuclear-associated receptor OGFr which results in reduced cell replication in the corneal surface [11]. Blockade of these effects using the opioid antagonist NTX either systemically or topically results in reversing many of the epithelial associated complications of type 1 or type 2 diabetes including decreased corneal surface sensitivity, delayed corneal wound healing, and dry eye [12–14]. Recent investigations in our laboratory have reported the dysregulation

of the OGF-OGFr axis corresponds with the onset and severity of dry eye in both male and female hyperglycemic rats [7, 15]. Twice daily topical administration of NTX for 6 weeks reversed the dry eye and restored the homeostasis of the corneal surface in these T1D animals [16].

In order to begin assessing the mechanisms related to NTX-related reversal of reduced tear production in diabetes, we investigated the morphology of the lacrimal functional unit (LFU) in untreated diabetic rats and in diabetic animals treated with NTX. Tear production results from secretions of the LFU, first defined in 2007 by International Dry Eye Workshop to include lacrimal glands, conjunctiva, corneal surface, Meibomian glands, and eyelids as well as the vasculature and nervous system connections [17] are explored by McKown et al. [18]. Knowledge about the morphological status of the lacrimal gland and its function in the secretion of ocular mucins is important in understanding DED [19, 20]. The different roles of the lacrimal gland in rodent versus human DED are still debated [21], but there is considerable agreement regarding the importance of inflammation and other aspects of the pathophysiology of the lacrimal gland to deciphering the causes and treatments of DED [18, 19]. Information on the LFU status in hyperglycemia and/or diabetes is sparse but researchers have shown that hyperglycemia induces dry eye through alterations in the LFU, as well as autonomic neural pathways, particularly the norepinephrine-adrenergic receptor-mitochondrial pathway [22]. The specific role of the OGF-OGFr axis in inducing or perpetuating tear flow is unknown. Nevertheless, blockade of the OGF-OGFr axis has an immediate impact on dry eye associated with diabetes, and as this study demonstrates, topical NTX treatment can reverse complications such as dry eye is within days. Our *hypothesis* is that the morphology of the LFU, specifically conjunctival goblet cells, and lacrimal gland acini, are dysregulated in size and function in diabetes and contribute to dry eye and corneal insensitivity. Moreover, we postulate that treatment with NTX will reverse histopathologic and immunohistochemical abnormalities induced in the lacrimal gland in diabetes, which eventuate in dry eye.

Materials and methods

Animals and treatment

The study design was approved by the Penn State College of Medicine Institutional Animal Use Committee (IACUC) and

followed regulations stated by the ARVO guideline for Use of Animals in Ophthalmic and Vision Research.

Male and female rats weighing approximately 150 g and 140 g, respectively, were purchased from Charles River Laboratories, Wilmington MA and housed in standard animal facilities receiving 12–12 h light-dark cycle, 14–18 changes of air hourly, and controlled humidity and temperature. Rats were placed 2 per cage and food and water were available *ad libitum*.

Hyperglycemia was induced as previously reported [13–15]. Briefly, animals were fasted for 4 h and then given an intraperitoneal injection with 50 mg/kg streptozotocin (STZ; Sigma-Aldrich) dissolved in citrate buffer, pH 4.5, on two consecutive days. Tail vein glucose was measured using a glucometer after 72 h; readings greater than 300 mg/dL were designated as hyperglycemic. At this time, rats were arranged such that hyperglycemic rats of the same sex were housed together in order to accommodate extra cage changes required by the increased urination. Animals that did not become hyperglycemic within 5 days of STZ injection were removed from the study.

After more than 6 weeks of hyperglycemia, animals were designated as type 1 diabetic (T1D) [23] and randomly assigned to a cohort treated with topical NTX drops (50 μ L) twice daily for 10 days; these animals were designated T1D-NTX. A single drop containing 5×10^{-5} M NTX was administered without anesthesia to the right eye only at 8–9 a.m. and 5–6 p.m. daily. T1D rats receiving vehicle-containing drops were designated as T1D and non-diabetic normal rats as Normal, were administered 50 μ L of vehicle within the same time period. Male and female rats were treated comparably.

For comparison and to insure that the effects of NTX were not harmful and related to diabetes, a separate cohort of Normal animals received NTX drops (Normal-NTX) or vehicle for 10 days. Tear volume was measured at baseline and at 5 and 10 days after drops.

To confirm rigor and reproducibility, four independent experiments using male rats and three independent experiments with female rats were conducted in a sequential manner. Ocular tissues from 12 diabetic males, 14 diabetic females, 8 non-diabetic normal males, and 9 non-diabetic Normal females were evaluated.

Ocular surface complications: *in vivo* measurements

Tear production and corneal sensitivity were measured in both male and female rats after 6 weeks of hyperglycemia. Measurements were made before initiating the NTX treatment (time 0) and at 5 and 10 days of NTX treatment; recordings at 5 and 10 days were taken prior to the morning treatment. All measurements were recorded on unanesthetized animals following published procedures [13–15].

Schirmer tests

Briefly, tear production was measured using Schirmer strips cut at 1 mm \times 17 mm length and placed into the lower lid cul-de-sac for 60 s. The wetting distance was measured to the half-millimeter using the manufacturer's scale.

Corneal surface sensitivity

Corneal surface sensitivity was measured using the blink reflex and the Cochet-Bonnet aesthesiometer (Boca Raton, FL). The amount of force (g/mm²) required to induce blinking was considered indicative of corneal sensitivity with greater pressure values indicative of insensitivity. Decreasing lengths of the filament were touched to the center of the cornea to elicit a blink reflex. The length of the filament required to induce a blink reflex was recorded; the procedure was repeated 3 times and averaged. The length was then converted to g/mm² using the manufacturers provided conversion chart.

Morphological changes in the LFU in diabetic rats

One day after NTX treatment was concluded, all rats in the study were humanely euthanized using a Euthanex carbon dioxide apparatus followed by decapitation. Orbital tissues were excised including the globes, eyelids containing Meibomian glands, conjunctiva, Harderian glands and external lacrimal glands. Tissues were fixed either in 4% paraformaldehyde for 1 h at 20°C followed by 12 h in 30% sucrose at 2–8°C or fixed in Hartman's Fixative for 12 h at 20°C and embedded in paraffin. Fresh-frozen tissues were frozen in chilled isopentane and stored at –80°C until cryosectioned. Tissues were stored for less than 10 days before processing for immunohistochemistry.

LFU morphology

Overall LFU morphology was assessed in paraffin-embedded hematoxylin and eosin (H&E) or periodic acid Schiff (PAS) stained sections (6–8 μ m) of lacrimal glands and eyelids containing Meibomian glands and goblet cells. Goblet cell number and size were assessed in PAS-stained conjunctival tissues measuring 200 μ m of conjunctiva starting at the deepest portion of the conjunctival crypt; goblet cells below 150 μ m² were excluded from counts. The number and size of acini in the Meibomian and lacrimal glands were measured in PAS-stained sections. Briefly, acini were counted from stained images that were imported into ImageJ software. Original images were photographed at \times 40 magnification on an Olympus BX50 microscope. The number of acini (\geq 24) within defined areas (200 μ m in diameter) was counted using at least 3 sections per animal and 3 animals per group for each sex.

Immunohistochemical (IHC) staining

Frozen sections (14–16 μm) of lacrimal glands were stained with validated antibodies for aquaporin-5 (AQP5; 1:100; ThermoFisher) followed by secondary antibodies using Alexafluor 568 (1:1000; ThermoFisher). IHC staining was assessed using confocal microscopy on an Olympus IX81 with Fluoview (FV1000) at $\times 40$ magnification.

Data analysis

IHC staining was measured using optical density. ImageJ software was calibrated as indicated by ImageJ protocols. Mean intensity of samples was normalized to the number of DAPI positive cells in the area captured. Data from the independent experiments were combined for each sex and analyzed using ANOVA (two-way or three-way) with a Tukey *post hoc* test for multiple comparisons. Throughout the study, data are expressed as SEM. All analyses were performed using GraphPad Prism version 9.0 (GraphPad Software, Inc.); $p < 0.05$ was considered statistically significant.

Results

Clinical signs

Male rats weighed approximately 146 ± 9 g at the time of inducing hyperglycemia. Eight weeks later Normal male rats weighed 493 ± 52 g and T1D animals weighed significantly less ($p < 0.01$) than Normals (approximately 328 ± 45 g). Female rats weighed 143 ± 6 g prior to inducing hyperglycemia, and following STZ injections at 8 weeks weighed 262 ± 10 g and 224 ± 5 g ($p < 0.01$) for Normal and T1D rats, respectively. Blood glucose levels at 72 h after STZ were approximately 480 mg/dL for rats injected with STZ (i.e., hyperglycemic) and for the non-injected Normal rats, glucose levels were ~ 120 mg/dL. NTX eyedrops had no effect on body weight or blood glucose levels in both sexes; data corroborated previous studies in this regard [7, 15, 16].

Mean tear volume and corneal sensitivity

After 6–7 weeks of hyperglycemia, tear production measurements as indicated by the length of wetting of the Schirmer strip were taken at baseline and after 5 and 10 days of NTX treatment for both males and females in all Normal, T1D, and treated cohorts; values are presented in Figure 1. Three-factor ANOVAs between condition (T1D, normal), treatment (NTX, vehicle), and sex were performed. At time 0, there were no interactions involving treatment, but both male and female T1D mice had Schirmer scores that were significantly less than

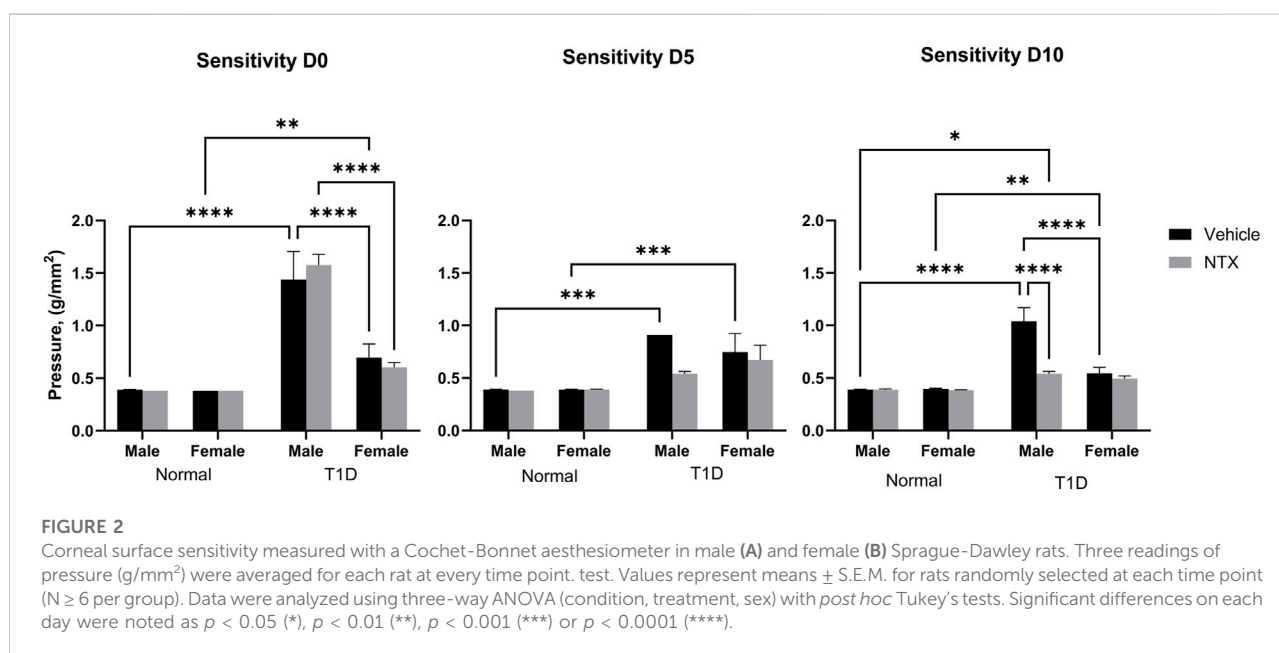
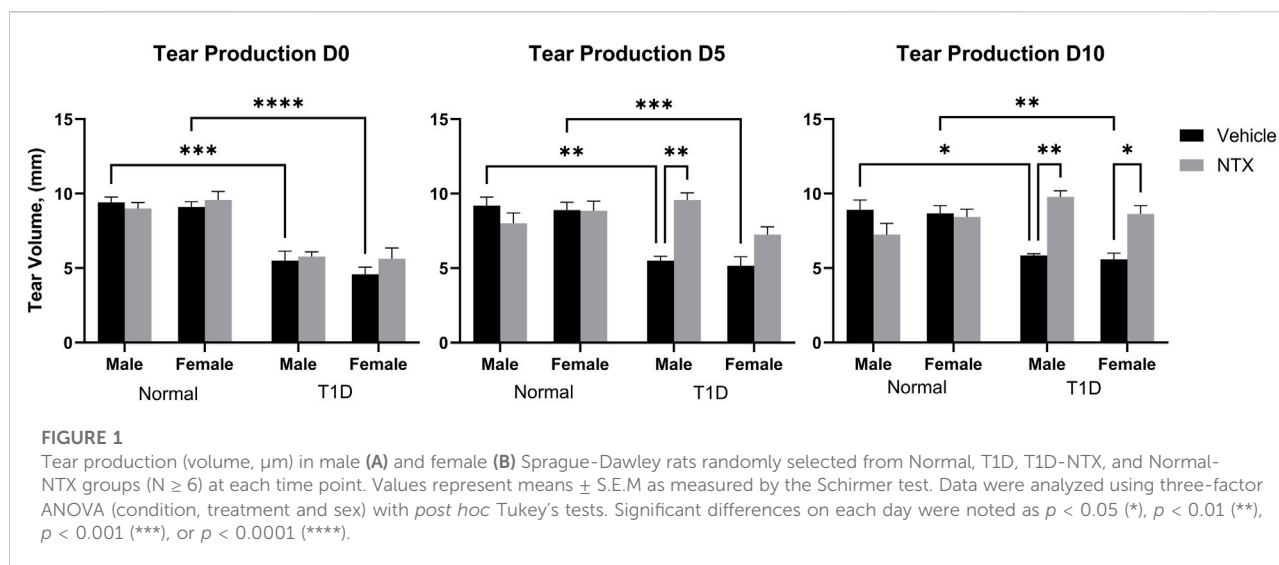
respective Normal rats of corresponding sex. Baseline Schirmer scores for male T1D rats were 5.5 ± 0.6 mm, a significant ($p < 0.001$) reduction of approximately 42% from normal values of 9.7 ± 0.6 mm. Baseline Schirmer scores for female T1D rats were 5.625, 38.26% less than Normal females ($p < 0.0001$). Three-factor ANOVA performed on day 5 showcased a significant interaction within condition ($F(1, 47) = 18.38$; $p < 0.0001$), treatment ($F(1, 47) = 8.008$; $p = 0.0068$) and between Condition \times treatment ($F(1, 47) = 18.03$; $p = 0.0001$). Within 5 days of NTX treatment, T1D male rats receiving NTX had substantially improved Schirmer scores that were significantly elevated above T1D rats receiving vehicle ($p < 0.01$) and comparable to Normal male rat values. Female T1D rats receiving NTX improved but did not reach significant levels in their Schirmer scores. After 10 days of NTX treatment, both male and female T1D rats receiving NTX had significantly higher ($p < 0.01$ for males; $p < 0.05$ for females) Schirmer scores that did not differ from Normal sex counterparts. T1D rats receiving vehicle continued to display reduced Schirmer values.

Corneal sensitivity was analyzed with a three-factor ANOVA (Figure 2). At baseline (time 0), Normal male and female rats had comparable pressure values of 0.39 g/mm force. T1D male rats required significantly ($p < 0.0001$) greater force to elicit a blink response. Female T1D rats at baseline required 0.65 g/mm force to elicit a blink; these values differed from both male T1D and Normal female rats. After 5 days of NTX treatment, male and female T1D rats receiving NTX had sensitivity scores comparable to Normals, but did not differ substantially from T1D rats receiving vehicle. After 10 days of NTX treatment, T1D male and female rats continued to have depressed sensitivity (i.e., elevated pressure scores). However, NTX treatment stabilized sensitivity in male T1D rats such that these animals had sensitivity scores that were significantly less ($p < 0.0001$) than T1D counterparts receiving vehicle.

Morphology of the lacrimal functional unit

External lacrimal gland

The number, size, and shape of lacrimal gland acini in PAS-stained sections are presented in Figure 3 for male and female Normal and diabetic rats. As captured in the images (Figure 3A), male diabetic rats had fewer ($p < 0.05$; $n = 14$ acini per $100 \mu\text{m}^2$) acini per lacrimal gland (Figure 3B) that were significantly smaller ($p < 0.0001$) in area than those in Normal male rats (Figure 3C). Regarding surface area of acini for male rats, Normal animals had mean areas of $1,415 \pm 33 \mu\text{m}^2$ in comparison to T1D rats with mean acini areas of $1,106 \pm 27 \mu\text{m}^2$. Ten days of NTX treatment did not alter the number (data not shown) or size of acini. Two-factor ANOVA revealed a significant interaction between sex vs. treatment ($F(2, 444) = 5.215$; $p = 0.0058$) followed by *post hoc* comparisons that reveals the acinar size



in female T1D-NTX rats was significantly smaller than for male T1D-NTX rats ($p < 0.001$). No differences in the number of acini were recorded for female rats in the Normal or T1D cohorts (Figure 3B), but the average surface area for lacrimal glands was smaller (Figure 3C) in T1D and T1D-NTX female rats relative to Normal females. Similar to males, 10 days of NTX treatment had no effect on the morphology of acini from female diabetic rats.

The function of lacrimal gland acini is to produce and release fluid in order to lubricate, protect, and cleanse the corneal surface. One of the major proteins in the aqueous tear film is aquaporin-5. Reduced levels of tear film aquaporin-5 are associated with dry eye and/or other epithelial surface

pathologies [24]. Aquaporins aid in transporting water across cell membranes. Aquaporin-5 is located in salivary and lacrimal glands, as well as corneal epithelium and alveolar type 1 cells. In the current experiments, AQP5 was measured by optical density in tissue (Figure 4A). Optical density measurements supported the visual images of lacrimal glands. Values were significantly decreased in stained sections from male ($p < 0.0001$) and female ($p < 0.01$) T1D rats relative to sex-matched Normals (Figure 4B). Within 10 days of topical NTX application, aquaporin secretion was substantially increased ($p < 0.001$) in T1D-NTX male rats, but not in female T1D-NTX rats. A two-factor ANOVA did not show a significant interaction between sex and treatment, but did

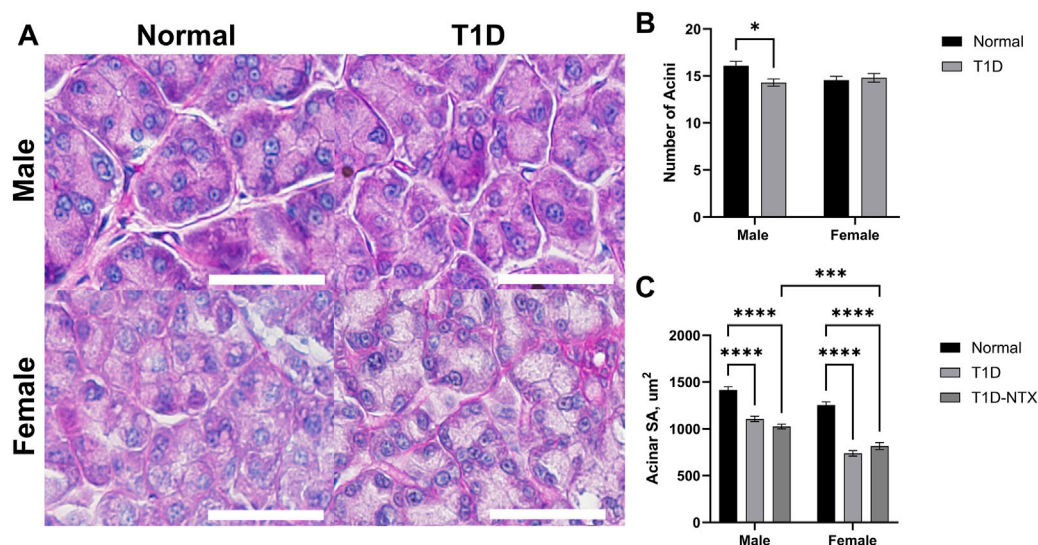


FIGURE 3

Morphology of lacrimal glands in male and female Sprague-Dawley rats. (A) Morphological images of lacrimal glands showing acini in male and female Normal and T1D rats. Tissues were stained with hematoxylin and eosin and photographed using an Olympus BX50 microscope at $\times 40$ magnification. Bar = $50\ \mu\text{m}$. (B) Histograms representing the number of acini (mean \pm SEM). (C) The mean area of individual acini (μm^2) for males and females in each cohort are recorded from areal measurements for >60 acini taken from images of at least 6 lacrimal glands per group for each sex. Data were analyzed with multiple factor ANOVA. There was a significant interaction between sex and treatment. Significantly different at $p < 0.05$ (*), $p < 0.001$ (***) and $p < 0.0001$ (****).

reveal that treatment had a significant effect ($F(2, 66) = 17.02$; $p < 0.0001$) on AQP5 presence in lacrimal gland tissue. Post hoc comparisons showed female T1D-NTX rats differed significantly from T1D-NTX male rats at $p < 0.05$ and had comparable AQP5 values as T1D female rats.

Size and number of conjunctival goblet cells

Goblet cells produce and secrete mucins that are an important component of the precorneal tear film by helping it to adhere to the ocular surface [20]. The mucin also is a repository for immunoregulation [22]. Goblet cells in the conjunctiva were stained with hematoxylin and eosin and exhibited changes in the surface area in T1D rats in comparison to Normal animals of the same sex (Figures 5A–C). Goblet cell number was measured $200\ \mu\text{m}$ from the deepest part of the conjunctival crypts, it was comparable between Normal and T1D rats of both sexes (Figure 5B). The surface area (Figure 5C) calculated from measurements of 65–100 cells in each treatment cohort revealed that the stained surface secretions in both male and female T1D rats were approximately $293.5 \pm 10\ \mu\text{m}^2$ whereas both sexes of Normal rats had cells with mean surface areas of approximately $446.1 \pm 14\ \mu\text{m}^2$ ($p < 0.0001$). NTX treatment for 10 days increased the surface area for both male ($p < 0.01$) and female ($p < 0.0001$) T1D-NTX rats. A significant two-way interaction between sex and treatment was noted ($p = 0.0065$),

followed by *post hoc* comparisons which revealed that female rats treated with NTX had significantly more mucin ($p < 0.01$) than male T1D-NTX rats.

Meibomian surface area

The surface area of the Meibomian glands, a representation of size and secretory capacity, were significantly smaller in both male T1D and female T1D rats relative to Normals (data not shown). The mean surface areas for Normal males and females were $4,884 \pm 334\ \mu\text{m}^2$ and $5,167 \pm 229\ \mu\text{m}^2$, respectively with approximately a 27% decrease in size in both male and female T1D glands. There were marginal increases in surface recorded in female T1D receiving 10 days of NTX, with no increase in area in male T1D rats.

Discussion

This study analyzed morphological and functional alterations in the LFU of diabetic rats treated with topical NTX. The LFU is essential in producing and maintaining a healthy tear film to help preserve ocular surface homeostasis. Previous studies have shown that diabetes produced altered morphology in the LFU structures, with decreased secretory granules in the lacrimal gland, decreased conjunctival goblet cell density, and decreased acinar size in Meibomian glands

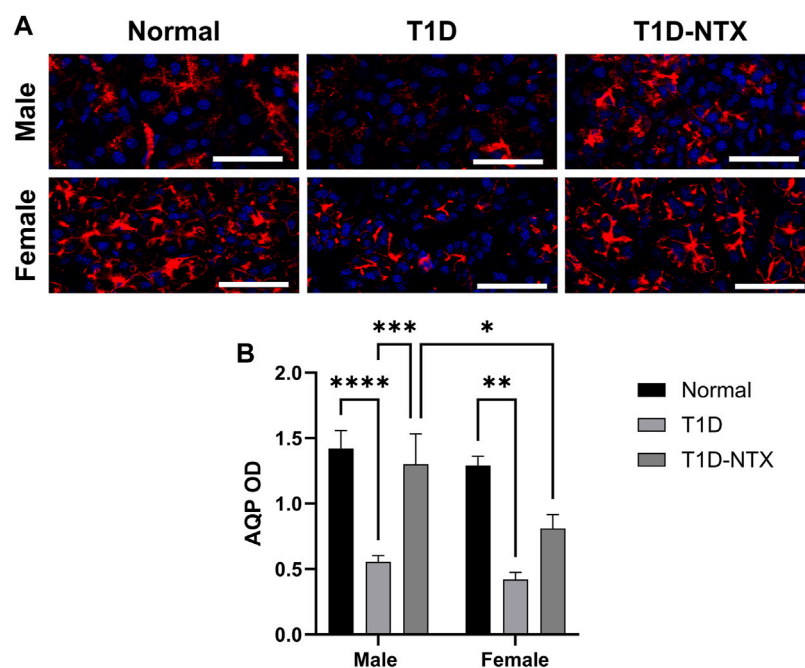


FIGURE 4

Aquaporin 5 expression in lacrimal glands of male and female normal and T1D rats. **(A)** Immunohistochemical images of aquaporin 5 expression in lacrimal glands of male and female Normal, T1D, and T1D-NTX rats. Tissues were stained with anti-aquaporin 5 (1:100) and AlexaFluor568 (1:1000) and images captured using Olympus IX81 confocal microscopy at $\times 40$ magnification. Bar = 50 μm . **(B)** Histogram values represent means \pm SEM for optical density measurements. Two-way ANOVA showed no significant interaction between sex and treatment. Primary factors were significantly different at $p < 0.05$ (*), $p < 0.01$ (**), $p < 0.001$ (***), and $p < 0.0001$ (****).

[25–27]. We found morphological alterations in the diabetic LFU after 6–7 weeks of hyperglycemia, with topical NTX altering only goblet cell deficits after 10 days of treatment. Topical treatment increased AQP5 expression levels in the lacrimal gland which we associated with increased tear secretion.

Conjunctival goblet cells aid in the production of the mucin layer of the tear film, which are responsible for providing a protective barrier against pathogens and providing lubrication [28]. Mucins have altered production and expression in dry eye syndrome with studies using a MUC5AC knock out mouse model to simulate dry eye disease in animals [29]. Our results revealed that topical NTX caused a restoration in the size of the conjunctival goblet cell and was interpreted as an increased production of cellular projects.

Similarly, diabetic Meibomian glands also showcased a decrease in acinar size. The Meibomian glands are responsible for the lipid layer of the tear film, which studies have shown to be dysregulated in persons with diabetes [30]. The lipid layer prevents desiccation and is described in the pathology of desiccative dry eye disease. Both the mucin and lipid layers of the tear film would not be directly responsible for the reflexive tear secretion produced by the Schirmer strips. This is a response caused by afferent corneal nerves being stimulated, causing parasympathetic activation of the lacrimal gland to “flush” irritants out of the corneal surface.

Our results support previous studies showcasing atrophied acini in the diabetic lacrimal gland that may reflect decreased cell size and/or secretory function [24, 31]. Studies have shown that diabetic rats have smaller secretory vesicles, decreased levels of cations, and decreased total protein [24, 32]. Topical naltrexone treatment did not alter the morphology of the lacrimal gland after 10 days. To investigate if there was an alteration in the secretory function of the lacrimal gland, we stained for AQP5. AQP5 is a water channel protein that plays a role in the generation of saliva, pulmonary secretions, and tears. Reduced expression of AQP5 has been measured in patients with Sjögren syndrome, and autoimmune disorder which commonly presents with dryness in the eyes and mouth [33]. Treatment with topical NTX increased expression levels of AQP5 in the lacrimal gland, which we attribute to stimulation by autonomic nerves causing the corneal reflex. Topical naltrexone may be modulating corneal nerve sensitivity or promoting nerve growth to allow for normal signaling. Topical analgesic drugs used in another study, showcased a similar increase in tear production and increase in AQP5 within the lacrimal gland, suggesting that corneal nerves can be affected by topical treatment [34].

Corneal stimulation activates polymodal nociceptors which trigger autonomic fibers responsible for lacrimal gland secretion.

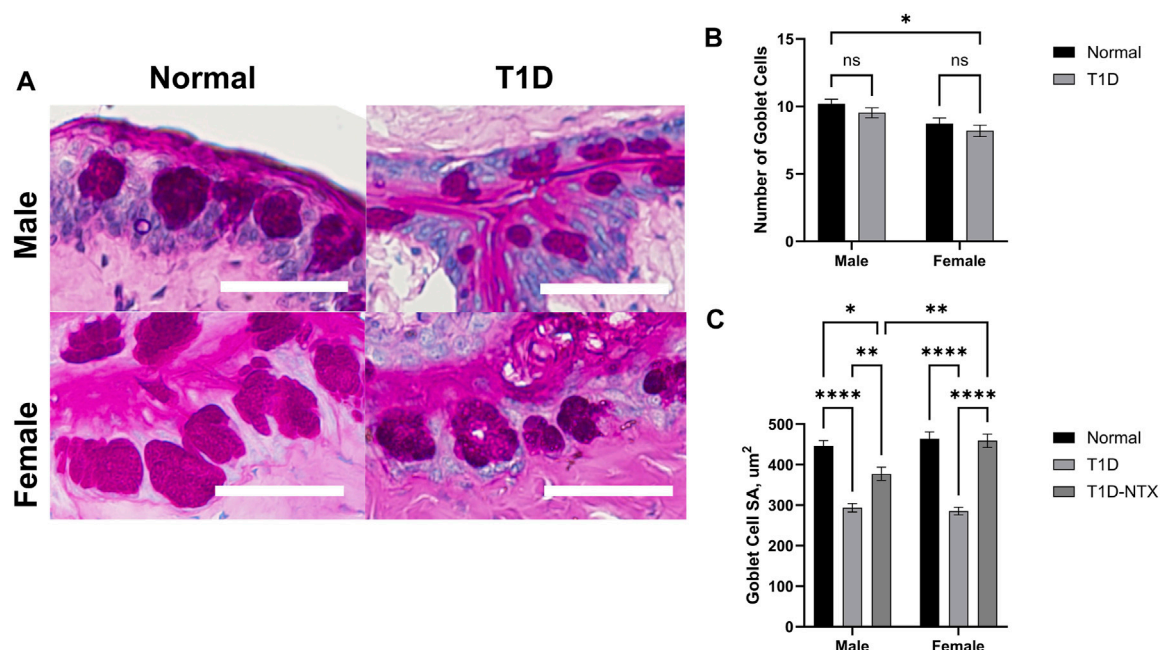


FIGURE 5

Analysis of goblet cells in the conjunctiva of male and female Normal and T1D rats. (A) Morphological images of the conjunctiva showing PAS-stained goblet cells. Images were taken using an Olympus BX50 microscope at $\times 40$ magnification. Bar = $50\ \mu\text{m}$. (B) Histograms of the number (mean \pm SEM) of goblet cells in Normal and T1D rats. (C) Histograms of (means \pm SEM) of the surface area (μm^2) of individual goblet cells. Analyses of variance indicated no significant interaction between sex and treatment for the number of goblet cells, but a significant interaction between sex and treatment ($p = 0.006$) for area. Post-hoc analyses showed differences at $p < 0.05$ (*), $p < 0.01$ (**), and $p < 0.0001$ (****).

The cornea is the most densely innervated and sensitive tissue in the body [35]. Peripheral neuropathy is common complication in diabetics, described as nerve damage that preferentially targets sensory axons, it can also occur in the cornea causing a decrease in corneal nerve density, decreased wound healing, and has been associated with dry eye disease [36–38]. Studies have suggested that corneal nerve density can increase within 1–2 weeks of topical treatment, with increases in corneal wound healing [39, 40]. We have previously shown that topical naltrexone increased corneal wound healing and increased corneal sensitivity, which we believe could be due to nerve regeneration or the release of neurotrophic factors by the corneal epithelial cells [13].

Type-1 diabetes in rats resulted in decreased LFU size, showcasing smaller acini in the meibomian and lacrimal glands, and reduced goblet cells within the conjunctival crypts. Ten-day topical NTX treatment resulted with increased goblet cell size, but did not show any changes to meibomian and lacrimal gland morphology. The increased tear production was attributed to increased secretory function within the lacrimal gland, inferred by the increased AQP5 staining expression. We suspect the reduced size in LFU structures is caused by decreased secretory function, which may be due to reduced signaling by autonomic pathways. NTX binds on corneal epithelial cells and blocks OGF from binding to its ligand, OGF. Blockage of this

negative growth pathway may result in decreased corneal regeneration, causing a poor signaling from corneal afferent nerves. Alternatively, naltrexone could indirectly promote the release of neurotrophic factors by altering corneal epithelium responsible for their production, creating interactions where denervation alters corneal epithelium and corneal epithelium can influence the survival of corneal nerves [41, 42]. Topical naltrexone does not seem to be affecting the LFU directly, instead it may be causing alterations to corneal nerve signaling pathways to cause downstream increased tear production.

Conclusion

In conclusion, our results indicate that type-1 diabetes alters the LFU morphology, and decreases lacrimal gland secretory function. The data clearly show increased tear production and AQP5 expression after NTX treatment. Future studies will investigate corneal nerve density in naltrexone treated diabetic rats. Naltrexone can block the growth inhibitor effects of a dysregulated OGF-OGFr axis which could be involved with delayed nerve growth in diabetic corneas. By looking at neurotrophic abundance or corneal nerve density we hope to elucidate the mechanism of naltrexone in dry eye.

Author contributions

DD: conceptualization, data curation, data analysis, data interpretation, writing-original draft, and final review. JS: conceptualization, data interpretation, and writing – review and editing. IZ: conceptualization, data interpretation, writing – review and editing, and funding acquisition. PM: conceptualization, data interpretation and confirmation of authenticity, project administration and supervision, writing – original draft, review and editing, and funding acquisition. All authors contributed to the article and approved the submitted version.

Data availability statement

The raw data supporting the conclusion of this article will be made available by the authors, without undue reservation.

Ethics statement

The animal study was approved by the Penn State University Institutional Care and Use Committee. The study was conducted

in accordance with the local legislation and institutional requirements.

Funding

The author(s) declare that financial support was received for the research, authorship, and/or publication of this article. The present study was supported by grant EY029223 from the National Eye Institute of the National Institutes of Health and the Shockey Family Foundation.

Conflict of interest

PM, IZ, and JS have intellectual property owned by Penn State Research Foundation that involves naltrexone treatment of the ocular surface for treatment of dry eye but receive no financial compensation or royalties.

The remaining author declares that the research was conducted in the absence of any commercial or financial relationships that could be construed as a potential conflict of interest.

References

- Centers for Disease Control and Prevention. *National diabetes statistics report* (2023). Available from: <https://www.cdc.gov/diabetes/data/statistics-report/index.html> (Accessed November 29, 2023).
- American Diabetes Association. *New report highlights diabetes research advances and achievements* (2024). Available from: <https://diabetes.org/newsroom/press-releases/new-report-highlights-diabetes-research-advances-and-achievements> (Accessed February 28, 2024).
- Lutty GA. Effects of diabetes on the eye. *Invest Ophthalmol Vis Sci* (2013) **54**: 81–7. doi:10.1167/iovs.13-12979
- Cousen P, Cackett P, Bennett H, Swa K, Dhillon B. Tear production and corneal sensitivity in diabetes. *J Diabetes its Complications* (2007) **21**:371–3. doi:10.1016/j.jdiacomp.2006.05.008
- Stephens DN, McNamara NA. Altered mucin and glycoprotein expression in dry eye disease. *Optom Vis Sci* (2015) **92**:931–8. doi:10.1097/oxp.0000000000000664
- McLaughlin PJ, Sassani JW, Kloczek MS, Zagon IS. Diabetic keratopathy and treatment by modulation of the opioid growth factor (OGF)-OGF receptor (OGFr) axis with naltrexone: a review. *Brain Res Bull* (2010) **81**:236–47. doi:10.1016/j.brainresbull.2009.08.008
- Zagon IS, Sassani JW, Purushothaman I, McLaughlin PJ. Dysregulation of the OGF-OGFr pathway correlates with elevated serum OGF and ocular surface complications in the diabetic rat. *Exp Biol Med* (2020) **245**:1414–21. doi:10.1177/1535370220940273
- Kloczek MS, Sassani JW, McLaughlin PJ, Zagon IS. Naltrexone and insulin are independently effective but not additive in accelerating corneal epithelial healing in type I diabetic rats. *Exp Eye Res* (2009) **89**:686–92. doi:10.1016/j.exer.2009.06.010
- Negri M, Fallucca F, Tonnarini G, Mariani P, D'alessandro M, Pachi A. High levels of circulating met-enkephalin in pregnant and menstruating type 1 diabetic women. *Gynecol Endocrinol* (1990) **4**:25–31. doi:10.3109/09513599009030688
- Negri M, Tonnarini G, D'Alessandro M, Fallucca F. Plasma met-enkephalin in type I diabetes. *Metabolism* (1992) **41**:460–1. doi:10.1016/0026-0495(92)90200-t
- Zagon IS, Sassani JW, Kane ER, McLaughlin PJ. Homeostasis of ocular surface epithelium in the rat is regulated by opioid growth factor. *Brain Res* (1997) **759**: 92–102. doi:10.1016/s0006-8993(97)00238-2
- Kloczek MS, Sassani JW, McLaughlin PJ, Zagon IS. Topically applied naltrexone restores corneal reepithelialization in diabetic rats. *J Ocul Pharmacol Ther* (2007) **23**:89–102. doi:10.1089/jop.2006.0111
- Zagon IS, Kloczek MS, Sassani JW, McLaughlin PJ. Dry eye reversal and corneal sensation restoration with topical naltrexone in diabetes mellitus. *Arch Ophthalmol* (2009) **127**:1468–73. doi:10.1001/archophthalmol.2009.270
- Zagon IS, Sassani JW, Immonen JA, McLaughlin PJ. Ocular surface abnormalities related to type 2 diabetes are reversed by the opioid antagonist naltrexone. *Clin Exp Ophthalmol* (2014) **42**:159–68. doi:10.1111/ceo.12144
- Purushothaman I, Zagon I, Sassani J, McLaughlin PJ. Ocular surface complications result from dysregulation of the OGF-OGFr signaling pathway in female diabetic rats. *Exp Ther Med* (2021) **22**:687. doi:10.3892/etm.2021.10119
- Zagon IS, Sassani JW, Purushothaman I, McLaughlin PJ. Blockade of OGFr delays the onset and reduces the severity of diabetic ocular surface complications. *Exp Biol Med* (2021) **246**:629–36. doi:10.1177/1535370220972060
- International Dry Eye Workshop. The definition and classification of dry eye disease report by the Subcommittee of the International Dry Eye Workshop (2007). *Ocul Surf* (2007) **2**:75–92. doi:10.1016/s1542-0124(12)70081-2
- McKown RL, Wang N, Raab RW, Karnati R, Zhang Y, Williams PB, et al. Lacritin and other new proteins of the lacrimal functional unit. *Exp Eye Res* (2009) **88**:848–58. doi:10.1016/j.exer.2008.09.002
- Conrady CD, Joos ZP, Patel BCK. Review: the lacrimal gland and its role in dry eye. *J Ophthalmol* (2016) **2016**:1–11. doi:10.1155/2016/7542929
- Davidson HJ, Kuonen VJ. The tear film and ocular mucins. *Vet Ophthalmol* (2004) **7**:71–7. doi:10.1111/j.1463-5224.2004.00325.x
- Schechter JE, Warren DW, Mircheff AK. A lacrimal gland is a lacrimal gland, but rodent's and rabbit's are not human. *Ocul Surf* (2010) **8**:111–34. doi:10.1016/s1542-0124(12)70222-7
- Zhang S, Wang Q, Qu M, Chen Q, Bai X, Zhang Z, et al. Hyperglycemia induces tear reduction and dry eye in diabetic mice through the norepinephrine- α_1 adrenergic receptor-mitochondrial impairment axis of lacrimal gland. *Am J Pathol* (2023) **193**:913–26. doi:10.1016/j.ajpath.2023.03.015
- Ghasemi A, Jeddi S. Streptozotocin as a tool for induction of rat models of diabetes: a practical guide. *EXCLI J* (2023) **22**:274–94. doi:10.17179/excli2022-5720

24. Hu S, Di G, Cao X, Liu Y, Wang Y, Zhao H, et al. Lacrimal gland homeostasis is maintained by the AQP5 pathway by attenuating endoplasmic reticulum stress inflammation in the lacrimal gland of AQP5 knockout mice. *Mol Vis* (2021) **27**: 679–90.
25. Shetty R, Saeed T, Rashed H, Adeghate E, Singh J. Effect of diabetes mellitus on acinar morphology, peroxidase concentration, and release in isolated rat lacrimal glands. *Curr Eye Res* (2009) **34**:905–11. doi:10.3109/02713680903184268
26. Mahadevan G, Hatti AS, Shashikala P, Kumar SA, Barki R. Conjunctival impression cytology and its varying patterns in controlled and uncontrolled diabetic patients. *J Clin Ophthalmol Res* (2023) **11**:140–5. doi:10.4103/jcor.jcor_147_21
27. Guo Y, Zhang H, Zhao Z, Luo X, Zhang M, Bu J, et al. Hyperglycemia induces meibomian gland dysfunction. *Invest Ophthalmol Vis Sci* (2022) **63**:30. doi:10.1167/iov.63.1.30
28. Blalock TD, Spurr-Michaud SJ, Tisdale AS, Heimer SR, Gilmore MS, Ramesh V, et al. Functions of MUC16 in corneal epithelial cells. *Invest Ophthalmol Vis Sci* (2007) **48**:4509–18. doi:10.1167/iov.07-0430
29. Floyd AM, Zhou X, Evans C, Rompala OJ, Zhu L, Wang M, et al. Mucin deficiency causes functional and structural changes of the ocular surface. *PLoS One* (2012) **7**:e50704. doi:10.1371/journal.pone.0050704
30. Lin X, Xu B, Zheng Y, Coursey TG, Zhao Y, Li J, et al. Meibomian gland dysfunction in Type 2 diabetic patients. *J Ophthalmol* (2017) **2017**:3047867. doi:10.1155/2017/3047867
31. Xue J, Zhang B, Dou S, Zhou Q, Ding M, Zhou M, et al. Revealing the angiopathy of lacrimal gland lesion in Type 2 diabetes. *Front Physiol* (2021) **12**: 731234. doi:10.3389/fphys.2021.731234
32. Changrani NR, Chonkar A, Adeghate E, Singh J. Effects of streptozotocin-induced type 1 diabetes mellitus on total protein concentrations and cation contents in the isolated pancreas, parotid, submandibular, and lacrimal glands of rats. *Ann N Y Acad Sci* (2006) **1084**:503–19. doi:10.1196/annals.1372.019
33. Chivasso C, D'Agostino C, Parisi D, Soyfoo MS, Delporte C. Involvement of aquaporin 5 in Sjögren's syndrome. *Autoimmun Rev* (2023) **22**:103268. doi:10.1016/j.autrev.2023.103268
34. Cammalleri M, Amato R, Olivieri M, Pezzino S, Bagnoli P, DalMonte M, et al. Effects of topical gabapentin on ocular pain and tear secretion. *Front Pharmacol* (2021) **12**:671238. doi:10.3389/fphar.2021.671238
35. Guerrero-Moreno A, Baudouin C, Melik Parsadaniantz S, Reaux-Le Goazigo A. Morphological and functional changes of corneal nerves and their contribution to peripheral and central sensory abnormalities. *Front Cel Neurosci* (2020) **14**: 610342. doi:10.3389/fncel.2020.610342
36. Zhao H, Ye Y, Ren Y-R, Chen B-H. Corneal alteration and pathogenesis in diabetes mellitus. *Int J Ophthalmol* (2019) **12**:1939–50. doi:10.18240/ijo.2019.12.17
37. Mansoor H, Tan HC, Lin MT-Y, Mehta JS, Liu Y-C. Diabetic corneal neuropathy. *J Clin Med* (2020) **9**:3956. doi:10.3390/jcm9123956
38. Feldman EL, Callaghan BC, Pop-Busui R, Zochodne DW, Wright DE, Bennett DL, et al. Diabetic neuropathy. *Nat Rev Dis Primers* (2019) **5**:41. doi:10.1038/s41572-019-0092-1
39. Wu M, Downie LE, Grover LM, Moakes RJA, Rauz S, Logan A, et al. The neuroregenerative effects of topical decorin on the injured mouse cornea. *J Neuroinflammation* (2020) **17**:142. doi:10.1186/s12974-020-01812-6
40. Yang S, Zhang Y, Zhang Z, Dan J, Zhou Q, Wang X, et al. Insulin promotes corneal nerve repair and wound healing in type 1 diabetic mice by enhancing wnt/ β -catenin signaling. *Am J Pathol* (2020) **190**:2237–50. doi:10.1016/j.ajpath.2020.08.006
41. Mastropasqua L, Massaro-Giordano G, Nubile M, Sacchetti M. Understanding the pathogenesis of neurotrophic keratitis: the role of corneal nerves. *J Cell Physiol* (2017) **232**:717–24. doi:10.1002/jcp.25623
42. Lambiase A, Sacchetti M. Neurotrophic factors and corneal nerve regeneration. *Neural Regen Res* (2017) **12**:1220–4. doi:10.4103/1673-5374.213534



OPEN ACCESS

*CORRESPONDENCE

Petr I. Nikitin,
✉ petr.nikitin@nsc.gpi.ru

RECEIVED 20 November 2023

ACCEPTED 23 April 2024

PUBLISHED 07 May 2024

CITATION

Gabashvili AN, Alexandrushkina NA, Mochalova EN, Goliusova DV, Sapozhnikova EN, Makarevich PI and Nikitin PI (2024), Internalization of transferrin-tagged *Myxococcus xanthus* encapsulins into mesenchymal stem cells.

Exp. Biol. Med. 249:10055.

doi: 10.3389/ebm.2024.10055

COPYRIGHT

© 2024 Gabashvili, Alexandrushkina, Mochalova, Goliusova, Sapozhnikova, Makarevich and Nikitin. This is an open-access article distributed under the terms of the [Creative Commons Attribution License \(CC BY\)](https://creativecommons.org/licenses/by/4.0/). The use, distribution or reproduction in other forums is permitted, provided the original author(s) and the copyright owner(s) are credited and that the original publication in this journal is cited, in accordance with accepted academic practice. No use, distribution or reproduction is permitted which does not comply with these terms.

Internalization of transferrin-tagged *Myxococcus xanthus* encapsulins into mesenchymal stem cells

Anna N. Gabashvili¹, Natalya A. Alexandrushkina^{2,3}, Elizaveta N. Mochalova^{1,4,5}, Daria V. Goliusova^{6,7}, Ekaterina N. Sapozhnikova⁴, Pavel I. Makarevich^{2,3} and Petr I. Nikitin^{1*}

¹Prokhorov General Physics Institute of the Russian Academy of Sciences, Moscow, Russia, ²Institute for Regenerative Medicine, Medical Research and Education Center, Lomonosov Moscow State University, Moscow, Russia, ³Faculty of Medicine, Lomonosov Moscow State University, Moscow, Russia, ⁴Moscow Center for Advanced Studies, Moscow, Russia, ⁵Nanobiomedicine Division, Sirius University of Science and Technology, Sirius, Russia, ⁶Koltzov Institute of Developmental Biology of the Russian Academy of Sciences, Moscow, Russia, ⁷Laboratory of Cell Biology, Lopukhin Federal Research and Clinical Center of Physical-Chemical Medicine of FMBA, Moscow, Russia

Abstract

Currently, various functionalized nanocarrier systems are extensively studied for targeted delivery of drugs, peptides, and nucleic acids. Joining the approaches of genetic and chemical engineering may produce novel carriers for precise targeting different cellular proteins, which is important for both therapy and diagnosis of various pathologies. Here we present the novel nanocontainers based on vectorized genetically encoded *Myxococcus xanthus* (Mx) encapsulin, confining a fluorescent photoactivatable mCherry (PAmCherry) protein. The shells of such encapsulins were modified using chemical conjugation of human transferrin (Tf) prelabeled with a fluorescein-6 (FAM) maleimide acting as a vector. We demonstrate that the vectorized encapsulin specifically binds to transferrin receptors (TfRs) on the membranes of mesenchymal stromal/stem cells (MSCs) followed by internalization into cells. Two spectrally separated fluorescent signals from Tf-FAM and PAmCherry are clearly distinguishable and co-localized. It is shown that Tf-tagged Mx encapsulins are internalized by MSCs much more efficiently than by fibroblasts. It has been also found that unlabeled Tf effectively competes with the conjugated Mx-Tf-FAM formulations. That indicates the conjugate internalization into cells by Tf-TfR endocytosis pathway. The developed nanoplatform can be used as an alternative to conventional nanocarriers for targeted delivery of, e.g., genetic material to MSCs.

KEYWORDS

encapsulins, fluorescence, photoactivatable label, imaging flow cytometry, targeted delivery nanosystem

Impact statement

The paper is dedicated to engineering of a novel genetically encoded vectorized encapsulin-based nanocontainer system. Encapsulin shells are extremely robust structures, resistant to high temperature and denaturation, and they also protect the payloads inside the shell reliably. Encapsulins also have very developed surface area which allows both loading various molecules inside and functionalizing the shells using vector groups. Therefore, encapsulins are very promising to serve as selective targeting nanocarriers. The data obtained allowed us to conclude that the interaction between Mx-Tf-FAM and MSCs was associated with Tf-TfR internalization pathway.

Introduction

Mesenchymal stromal/stem cells (MSCs) are cells capable of mesodermal cell lineages differentiation. These cells can differentiate into osteocytes, chondrocytes, adipocytes, and muscle cells [1]. The possibility of obtaining MSCs from different biological niches, their low immunogenic and modulating features [2] enable autologous and allogeneic transplantation of these cells. MSCs are employed for the treatment of various pathologies such as bone and cartilage diseases [3, 4], cardiovascular diseases [5, 6], neurological disorders [7–9], bronchial diseases [10], and many others. Despite some success of therapy with MSCs, the clinical application of these cells is restricted by the phenotypic plasticity. These cells lose stemness *ex vivo*, resulting in reduced therapeutic potential [11]. Various genetic modifications of MSCs can partially overcome this issue.

It is considered that MSCs transduction using, for example, lentiviral vectors is quite effective. However, this method of cell modification is not always applicable due to safety concerns associated with the possibility of insertional mutagenesis, as well as possible immunogenicity of viral antigens [12]. In addition, lentiviral gene delivery systems have a relatively small transgene cargo capacity [13].

There are also numerous methods of nonviral gene delivery to MSCs. Some approaches are realized by violating the integrity of cell membranes as a result of microinjection or electroporation [14, 15], or using cell penetrating peptide [16]. Other methods are based on the use of various nanocarriers, such as inorganic materials, lipids, polymers, etc., [17, 18]. These techniques are safer, but, with rare exceptions, may cause a decrease in cell viability [19]. Therefore, the development of new gene delivery tools, devoid of the described disadvantages, is an extremely urgent task. Here, we describe a new targeted delivery system that employ the *Myxococcus xanthus* (Mx) encapsulins as vector nanocontainers. Encapsulins are bacterial capsid-like, high molecular weight structures consisting of a protein shell and a cargo protein contained within. The encapsulin shells are extremely stable, have different diameters, and reliably protect the cargo proteins. The proteins carried by

encapsulins are diverse and differ in their functions [20]. Since the discovery of encapsulins in 1994, the focus of their investigation has gradually shifted towards using these structures as nanocontainer systems. A number of encapsulin-based delivery systems were developed. For example, *Thermotoga maritima* (*T. maritima*) encapsulin-based system that selectively binds glucose-regulated protein 78 in human HepG2 carcinoma cells [21]. A similar system was developed for targeted delivery of encapsulins loaded with mini SOG (mini-Singlet Oxygen Generator) to HER2⁺ breast cancer cells [22]. A possibility of RNA or DNA loading into encapsulin shells was also demonstrated in recent works [23, 24].

The wild type Mx encapsulin (Supplementary Figure S1) consists of a protein shell (EncA) self-assembled of 180 identical monomeric proteins (32.5 kDa each) confining three ferritin-like cargo proteins (EncB, 17 kDa; EncC, 13 kDa; EncD, 11 kDa) [25]. We replaced Mx EncBCD ferritin-like native cargo with an irreversibly photoactivatable derivative of mCherry (PAmCherry) fluorescent protein as we previously described [26]. We further modified the Mx shells with human transferrin (Tf) preliminary labeled with a fluorescent dye of fluorescein-6 (FAM) maleimide to provide selective binding to the transferrin receptors (TfRs) on MSCs. The binding selectivity of the resulting vector system (Mx-Tf-FAM) to MSCs was confirmed by the laser scanning confocal microscopy and imaging flow cytometry. It was also demonstrated that free Tf competed for binding with the Mx-Tf-FAM conjugates. That indicated the conjugate internalization into the cells by receptor-mediated endocytosis.

The current study demonstrates a biodegradable, non-toxic and non-viral nanocarrier system that selectively binds to TfRs on the membranes of MSCs followed by rapid internalization into cells via Tf-TfR pathway. Such Tf-mediated targeting may be useful not only for the delivery of genetic material to MSCs, but also for therapeutic purposes in the treatment of cancer. For example, to deliver siRNA (small interfering RNA) to TfRs overexpressing tumor cells.

Materials and methods

Cell cultures

The procedures performed with patient tissue samples were in accordance with the Declaration of Helsinki and approved by the Local Ethics Committee, Medical Research, and Education Center, Lomonosov Moscow State University (IRB00010587), protocol #4 (2018). Samples of human adipose-derived MSCs were collected from the Cryobank of the Institute for Regenerative Medicine of Lomonosov Moscow State University (collection ID MSC_AD_MSU¹, accessed on

¹ www.human.depo.msu.ru

17 November 2023). Informed consent was obtained from all subjects involved in the study.

MSCs were cultured on DMEM/F12 supplemented with 10% FBS (HyClone, Cytiva, Washington, D.C., United States), 2 mM L-glutamine, and antibiotics (100 U/mL penicillin, 0.1 mg/mL streptomycin) in T-75 cell culture flasks. Human fibroblasts were kindly provided by the Laboratory of Cell Biology of Lopukhin Center of Physical-Chemical Medicine of FMBA of Russia. 293T EncA_PamCherry cells and fibroblasts were cultured in DMEM in T-25 flasks with addition of 100 U/mL penicillin, 0.1 mg/mL streptomycin, 2 mM L-glutamine and 10% FBS. All cell cultures were grown under standard conditions (5% CO₂ and 37°C). All reactants were purchased from Gibco (New York, NY, United States) and laboratory plastic was purchased from Corning (New York, NY, United States).

Mesenchymal stem cells differentiation

MSCs differentiation into chondroblasts, adipocytes, and osteoblasts was carried out using a commercial StemPro[®] Differentiation kit according to the manufacturer's instruction [27–29]. After the differentiation was completed, the resulting chondroblasts, adipocytes, and osteoblasts, and were stained using Alcian Blue (Sigma-Aldrich, St. Louis, MI, United States), OilRed O (Sigma-Aldrich), and Alizarin Red (Sigma-Aldrich), respectively. A Primo Vert light inverted microscope (Zeiss, Baden-Württemberg, Germany) was used to obtain images of the stained cells.

Flow cytometry

For the flow cytometry, MSCs were labeled with conjugated primary antibodies for MSCs positive (CD105, CD73, and CD90) and negative (CD19, CD45, CD34, CD14, and HLA-DR) markers using the MSC Phenotyping Cocktail Kit, anti-human (Miltenyi Biotec, Bergisch Gladbach, and Germany) according to the standard protocol [30]. The expression of markers was assessed with a flow cytometer-sorter (FACS Aria III, BD Biosciences, Franklin Lakes, NJ, USA). Dead cells were excluded from the analysis by staining with SytoxBlue Dead Cell stain (Invitrogen, Waltham, MA, United States); cell debris, and duplexes were excluded based on the forward and side light scattering parameters.

Imaging flow cytometry

24 h prior to the experiment MSCs were cultured in a 96-well plate (~7,000 cells/well, Corning) in 100 µL of DMEM/F12 medium supplemented with 10% FBS. For Tf competition binding assay, Mx-Tf-FAM encapsulins in PBS (50 ng/µL) mixed

with free soluble Tf (in fivefold excess) were added to the cells. After 1.5 h incubation the cells were washed three times with DPBS to remove the unbound Mx-Tf-FAM and Tf. Next, the cells were detached from the plastic, precipitated (500× g, 5 min), and resuspended in 0.1 mL of 4% PFA in PBS (pH 7.4). Cytometric assays were performed using an ImageStream X Mark II imaging flow cytometer (Amnis, Luminex Corporation, Austin, TX, United States), which is a powerful tool for investigation of binding [31, 32]. The present studies were carried out using a ×40 objective, 488-nm (175 mW) laser for fluorescence excitation, and at 785-nm laser light (0.5 mW) for side scatter measurements.

Laser scanning confocal microscopy

The cell imaging was performed using an A1R MP+ (Nikon, Tokyo, Japan) instrument (405 and 561 nm laser wavelengths, oil immersion objective lenses Apo TIRF 60×/1.49) or Eclipse Ti2 (Nikon, Tokyo, Japan) (405, 561, and 642 nm laser wavelengths, Apo 25×/1.1 water immersion objective lenses) laser scanning confocal microscopes. The scanning was performed using the ThorImageLS 2.4 Software (Thorlabs, Newton, NJ, United States) and Nikon NIS elements 4.50 software (Nikon, Tokyo, Japan). To process the images the ImageJ2 Fiji software was used.

Immunoprecipitation

293T EncA_PamCherry cells were placed into 6-wells plates in 2 mL of DMEM culture medium (1.5 × 10⁶ cells/well), FLAG-tagged Mx encapsulins were isolated from 293T EncA_PamCherry cells after 24 h of cultivation using Anti-FLAG M2 Affinity gel (Sigma Aldrich) according to the manufacturer's instruction as described earlier [26].

Dynamic light scattering

The hydrodynamic diameter of purified Mx encapsulins was measured via ZetaSizer Nano ZS (Malvern, UK) at 25°C using standard glass cuvettes containing 1,000 µL of eluate solution in TBS according to a procedure recommended the manufacturer [33].

Western blot analysis

Briefly, 293T EncA_PamCherry cells were, and the resulting lysate was centrifuged for 20 min at 14,000 × g. Buffer 5× was added to various amounts (2 µL, 5 µL, 10 µL, and 20 µL) of the cell lysate, then heated at 95°C, and after that cooled on ice. The lysate was loaded onto gel and electrophoresed for 25 min at 80 V

and then for 1.5 h at 100 V. The gel was moved into a transfer buffer. The activated nitrocellulose membrane was placed over the gel. The transfer procedure was fulfilled for 1 h at 100 V in a chamber filled with transfer buffer. The membrane was thoroughly washed in PBST to remove the transfer buffer. The membrane was incubated with 5% non-fat milk in PBST solution for 2 h to prevent nonspecific binding and then washed again. The membrane was incubated with anti-Flag Tag antibodies (1:1,000, BioLegend, San Diego, United States) for 2 h followed by washing three times with DPBS. Next, secondary antibodies (1:1,000, goat anti-mouse IgG, Santa Cruz Biotechnology, Dallas, United States) conjugated with alkaline horseradish peroxidase were added. The results were readout by a ChemidocMP Imaging system (BioRad, Hercules, United States).

Conjugation with fluorescent dye and engineering of Tf-FAM labeled Mx encapsulins

At first, apo transferrin (10 mg, Merck, Rahway, NJ, United States) was dissolved in 2 mL of DPBS (pH = 6.8). Fluorescein-6 maleimide (Lumiprobe, Russia) in the amount of 2 μ L (20 mg/mL in DMSO) was added and mixed overnight at constant stirring at ambient temperature. After that, the resulting solution was purified five times using centrifugal concentrator 30 kDa cut off filters (Millipore Billerica, United States) and adjusted to 1 mL in PBS (pH = 7.4). Then, 10 μ L of 6-Maleimidohexanoic acid N-hydroxysuccinimide ester at concentration of 0.5 mg/mL in water:DMSO 1:1 was mixed with Tf-FAM followed by 1 h incubation at ambient temperature. The solution was also purified five times by 30 kDa cut off filters and resolved in 1 mL PBS (pH = 6.8). At last, the isolated Mx encapsulins were also diluted in PBS at pH = 6.8 and mixed 1:1 by weight in 1 mL of the reaction mixture overnight. The produced conjugates were washed seven times using 100 kDa cut off filters and PBS (pH = 7.4). The 500 ng/ μ L Mx-Tf-FAM stock solution was kept at 4°C.

Cellular uptake of Mx and Mx-Tf-FAM encapsulins

MSCs and human fibroblasts were seeded on a 2-well μ -Dish for confocal microscopy (Ibidi, Martinsried, Germany) in the amount of 1×10^4 cells/dish and cultured for 24 h prior the assay. Following the cultivation, 30 μ L of Mx or Mx-Tf-FAM samples in PBS aligned according to protein concentration was added to the cells to the final concentration of ~290 ng/ μ L. The cells were incubated at 5% CO₂ and 37°C for 30 and 90 min. After that, the culture medium was removed. The cells were washed thoroughly with DPBS to

remove unbounded encapsulins. The cells were studied using a Nikon Eclipse Ti2 confocal microscope.

Results

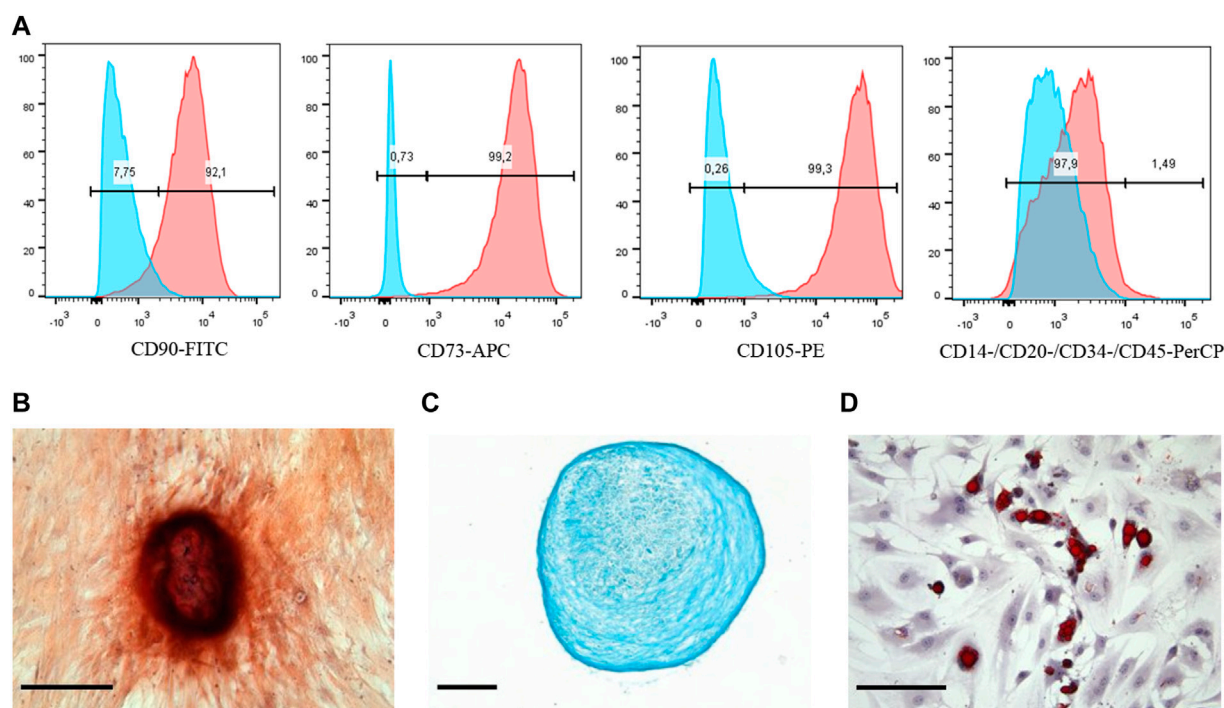
Characterization of MSCs

At first, the markers on the cell surface were detected using the flow cytometry. The data obtained showed that the expression profile of CD markers was typical for MSCs. The cells were positive for the main MSCs markers (CD73, CD90, and CD105) and negative for such markers as CD14, CD20, CD34, and CD45 (Figure 1A). Besides, it is well-known that MSCs have a potential for multidirectional differentiation into a different cell type (chondrocytes, adipocytes and osteoblasts). We used commercially available kits that allowed implementation of *in vitro* MSCs differentiation. As can be seen in Figure 1B, MSCs exhibited positive Alizarin Red staining after osteogenic induction; positive Alcian blue (as shown in Figure 1C) and Oil Red O (as demonstrated in Figure 1D) staining after chondrogenic and adipogenic induction, respectively. Thus, the mesenchymal identity (i.e., the ability for multilineage differentiation and CD markers expression profile) of MSCs was confirmed. The images of the negative control cells for each staining are demonstrated in Supplementary Figure S2.

Isolation and characterization of Mx encapsulins

Our previous study showed that expression of stable Mx encapsulin protomer protein such as EncA tagged with a DYKDDDDK sequence and the fluorescent PAmCherry cargo encoding genes could be successfully achieved in mammalian 293T cells. We also demonstrated that encapsulated label did not affect cell proliferation and viability [26].

In this study we first verified the presence of necessary transgenic sequences, as well as proteins translated from them. For this purpose, PAmCherry was photoactivated in the transgenic 293T cells. PAmCherry encoding gene is coupled to a short protein (Figure 2A) unstable under physiological conditions [destabilization domain (DD)] [34]. The presence of DD leads to PAmCherry protein degradation by the proteasome if not encapsulated into the Mx shell. As can be seen from Figure 2B, after the activation with a laser with the wavelength of 405 nm and subsequent excitation with a 561 nm light, a bright red fluorescent signal from PAmCherry was detected in the cell cytoplasm. Therefore, we could conclude that the expression of encapsulated PAmCherry label was retained. The protein expression of EncA protomers was also confirmed by the Western blot analysis. A single band of protomer protein

**FIGURE 1**

Phenotypic characterization and multilineage differentiation of human MSCs. **(A)** Flow cytometry analysis of the MSCs surface markers expression: red graphs show experimental samples, while blue graphs—negative control. MSCs differentiation: **(B)** Osteogenic revealed by Alizarin Red, **(C)** chondrogenic revealed by Alcian Blue, and **(D)** adipogenic revealed by Oil Red staining. Scale bars are 50 μ m.

with a weight of ~ 35 kDa was clearly visible (Figure 2C). The encapsulins were further isolated from the cells, and the hydrodynamic size of the shell was measured using the DLS analysis. According to the DLS analysis, the hydrodynamic size of isolated Mx encapsulins (Figure 2D) was 37 ± 6 nm with 0.4 PDI (polydispersity index). This value corresponds well to the size of the Mx encapsulin shell described in literature [35].

Engineering of Tf-FAM double-labeled Mx encapsulins

We have developed a strategy for FAM-labeled Tf conjugation with Mx encapsulin shells using EMCS – a heterobifunctional cross-linking reagent with amine and sulfhydryl reactivity (Figure 3). Thus, the receptor-targeted Mx-Tf-FAM obtained in this study has two fluorescent labels: PAmCherry (spectral maximum of excitation at 564 nm and emission at 595 nm) inside the shell, and FAM (spectral maximum of excitation at 492 nm and emission at 517 nm) on the shell. These two fluorescent labels, on the one hand, enable verification of Tf-FAM localization on the shells of Mx encapsulins, and, on the other hand, visualize the conjugate internalization into cells.

Cellular uptake of vectorized Mx encapsulins by MSCs

First of all, the ability of Tf-FAM to bind to TfRs was analyzed by the laser scanning confocal microscopy using MSCs and human fibroblasts. The obtained microphotographs (Figure 4A) show that TfRs are visualized as characteristic placoids with cytoplasmic localization. The imaging flow cytometry measurements (Figures 4B, C) also confirmed MSCs to be TfR positive. It can be seen that the TfR expression in fibroblasts is dramatically lower compared to that of MSCs (Supplementary Figure S3).

Next, the laser scanning confocal microscopy was used for qualitative estimation of the uptake and intracellular distribution of Mx-Tf-FAM by MSCs. The obtained micrographs (Figure 5) clearly show the co-localization of two intense fluorescent signals in green and red spectral ranges. It can also be seen that the fluorescent signal is localized predominantly on membranes of the cells after 30 min of incubation (Figure 5, upper row), and after 1.5 h of incubation (Figure 5, lower row), the signal from the labels is also observed in the cytoplasm of the cells. The uptake of Mx-Tf-FAM by control fibroblasts is presented in Supplementary Figure S4. In contrast to the result obtained for MSCs, the fluorescent signals from Tf-FAM and PAmCherry in fibroblasts are barely distinguishable.

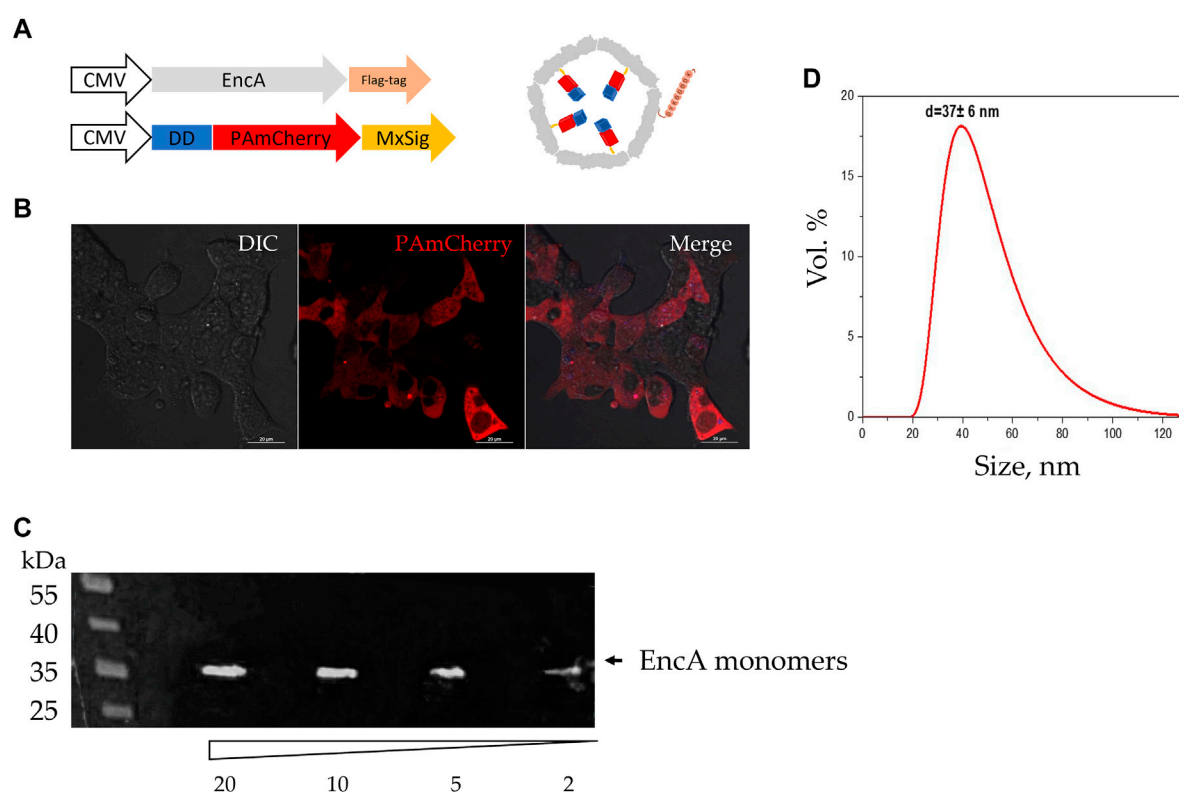


FIGURE 2

Assembly of Mx encapsulins and PAmCherry photoactivation in 293T cells. (A) Schematic representation of the genetic constructs (with minor omissions) and the assembled Mx encapsulin shell containing a photoactivatable protein. At the N-terminus, PAmCherry is fused to a destabilization domain (DD) to degrade such a protein that is not encapsulated within the envelope. MxSig is C-terminal Mx encapsulation signal, CMV—cytomegalovirus promoter; (B) 293T EncA_PAmCherry cells after irradiation with a 405 nm laser followed by excitation with light with 561 nm wavelength. Laser scanning confocal microscopy using Nikon A1 MP instrument, scale bars are 20 μ m; DIC—differential interference contrast; (C) Western blot analysis against FLAG-tag on EncA protomer proteins; the numbers indicate the volume of cell lysate (2, 5, 10, and 20 μ L) added to the gel; the triangle indicates a decrease in the volume of cell lysate added to the gel; black arrow indicates a band with a molecular weight of 35 kDa region; (D) Dynamic light scattering analysis of isolated Mx encapsulins ($d = 37 \pm 6$ nm; PDI 0.4).

At last, to verify that the interaction between Mx-Tf-FAM and MSCs was related to Tf-TfR interaction, we assessed by the imaging flow cytometry the ability of free Tf to compete for interaction with the vectorized encapsulins. It was shown (Figure 6A) that the median intensity in the “Mx-Tf-FAM” sample exceeded that of the “Mx-Tf-FAM + Tf” sample. It can also be seen (Figure 6B) that the FAM fluorescence intensity in the “Mx-Tf-FAM” sample is significantly higher compared to that observed in the “Mx-Tf-FAM + Tf” sample (Figure 6C). In addition, it can be noted that in spite of MCSs presence in bright field, the FAM signal is almost absent (Figure 6C).

The results obtained demonstrated that the unlabeled Tf effectively competed with the conjugated Mx-Tf-FAM formulations. That indicates conjugate internalization into cells by, supposedly, receptor-mediated endocytosis. Certainly, further research is required to recognize the exact Mx-Tf-FAM endocytosis pathway, for example, using endocytosis blockers.

Discussion

Over the past decades, many different nanocarrier delivery systems were developed, e.g., gold [16, 36] and iron oxide [37, 38] nanoparticles, including those with metal-organic framework storages for drug and *in vivo* gene delivery [39, 40]; micelles [41]; hybrid liposome-, polymer- [42], and protein-based nanoparticles [43, 44]. The shells of such carriers can be modified by adding to their surface various receptor molecules to provide fast binding kinetics to the related ligand [45] and achieve specific targeting [46]. An important part of these studies was investigation of toxicity of the obtained nanocarriers and the products of their *in vivo* biodegradation [47–49]. Among others, the protein-based nanocontainers (virus-like particles, ferritins, encapsulins) are of particular interest due to their stability, non-toxicity, and biodegradability.

As it is mentioned above, encapsulins are very similar in structure to viral capsids. Like viral capsids, they reliably keep the internal payload of the shell. In our recent work [26] on RAW

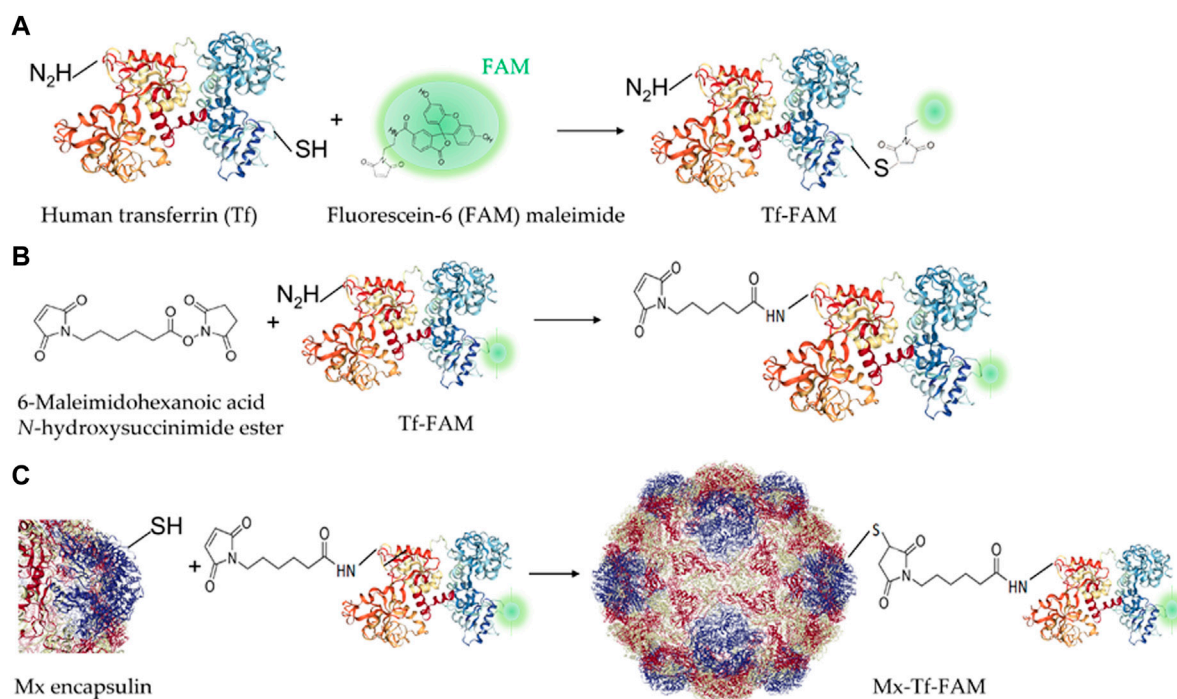


FIGURE 3

Schemes of Tf-FAM-conjugated Mx encapsulins preparation. **(A)** Labeling of human Tf with FAM; **(B)** Tf-FAM binding with the bifunctional EMCS linker; **(C)** Conjugation of Tf-FAM with Mx encapsulin using EMCS.

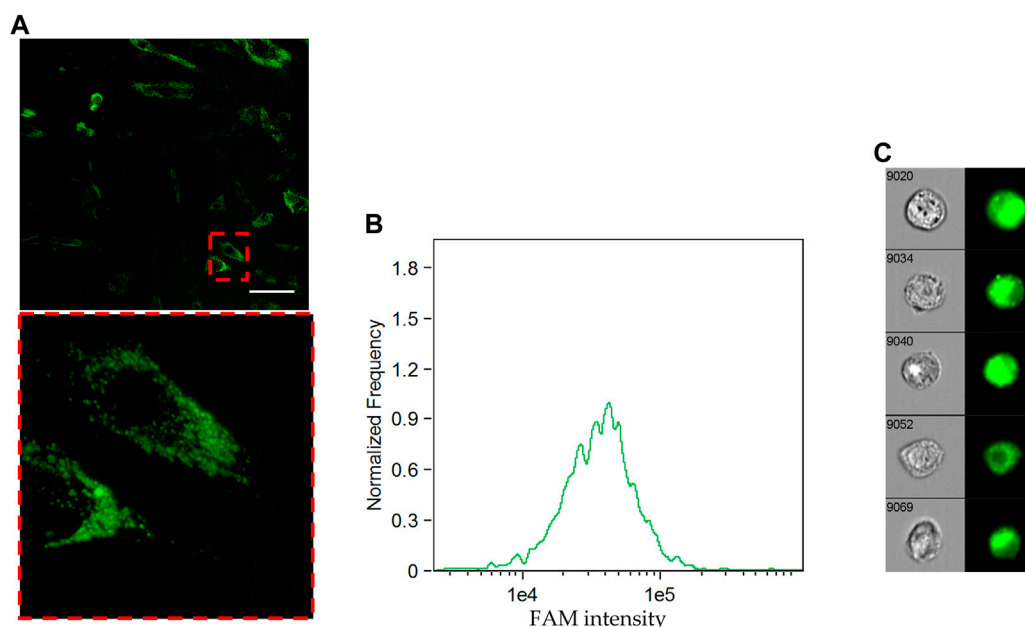
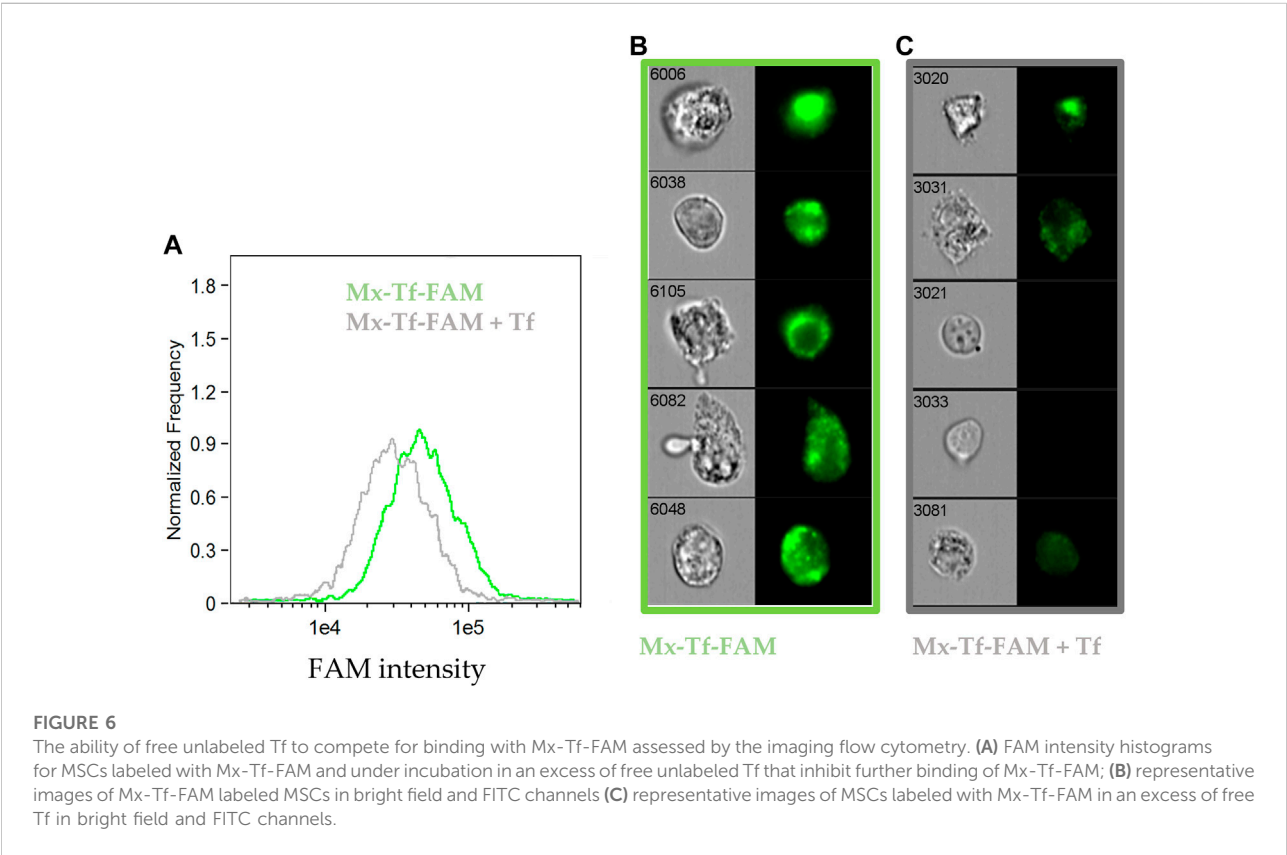
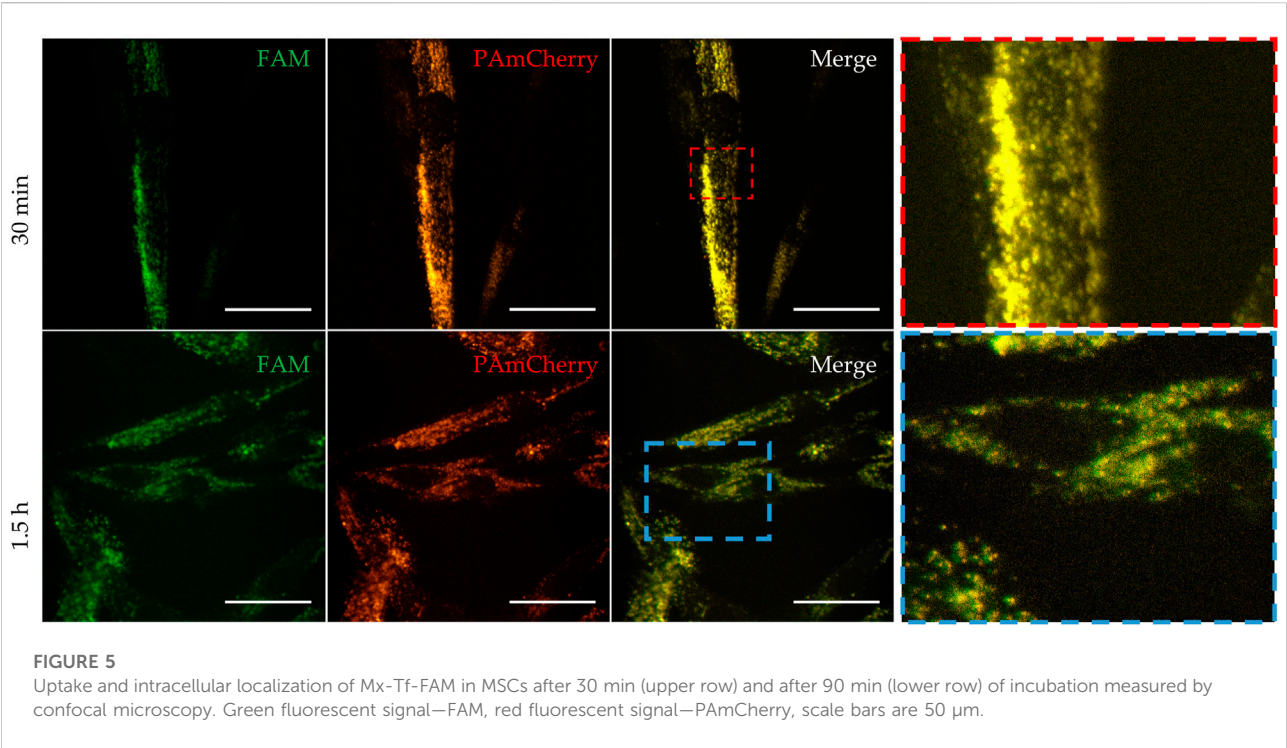


FIGURE 4

Cellular uptake of FAM-labeled transferrin by MSCs. **(A)** Uptake of Tf-FAM in MSCs after 90 min incubation. Green fluorescent signal shows FAM. Laser scanning confocal microscopy, scale bar 50 μ m. **(B)** FAM intensity histogram and **(C)** representative images of Tf-FAM labeled MSCs in bright field and FITC channels of an imaging flow cytometer.



264.7 cells, it was shown that Mx encapsulin shells protect the cargo protein from the action of intracellular proteases for at least 2 h. Interestingly, there is one more research, in which the authors investigated the uptake of fluorescently labeled encapsulins by macrophages (J774 macrophages cell line) [50] but they used a significantly longer internalization time.

In the present research, FAM-labeled human transferrin was obtained by binding of SH-groups with FAM-maleimide. Tf-FAM was then chemically conjugated using a linker bound with NH₂-groups of Tf-FAM and SH-groups on the encapsulin shells. According to the PDB data (entry 7S20), each EncA monomer has two cysteines in its structure. In total, the Mx encapsulin shell consists of 180 such monomers so the EMCS linker is potentially capable of binding FAM-labeled transferrin in 360 sites. That enables amplification of the fluorescent signal of FAM.

Prior to exploring the Tf-mediated targeting, we tested the uptake of non-vector Mx encapsulins by MSCs and human fibroblasts. No, even minimal, fluorescent signal of PAmCherry was detected in the cells after 2 h of incubation (Supplementary Figure S5). Unlike macrophages, neither MSCs nor fibroblasts are professional phagocytes. That is why they are not able to rapidly internalize protein structures of high molecular weight. The fact that Mx encapsulins are naturally inert to MSCs again confirms the need for further development of the targeted nanocarriers.

TfR-mediated endocytosis is a relatively fast process but the rate of Tf internalization varies in different cells [51]. In the case of MSCs, internalization of Mx-Tf-FAM conjugates could be registered after 30 min of incubation, while after 1.5 h incubation, fluorescent signals from FAM and PAmCherry were detected throughout the cell cytoplasm.

The targeted delivery system presented in this work is effective not only for MSCs but also for other cells of high TfR expression level. This is particularly true for malignant cells. It is well known that TfR plays an important role in the processes of proliferation, migration, and invasion of cancer cells [52–54]. As an example, one such neoplasm is known to be human glioblastoma multiforme—the primary grade IV brain tumor in adults with poor prognosis [55]. The model PAmCherry cargo protein used in this study can be further replaced/supplemented with different genetic material [56, 57], and the resulting nanoplatfrom can be an alternative to viral vectors for nucleic acids delivery to MSCs [58]. Moreover, this platform is suitable for intracellular delivery of recombinant proteins which is a potential strategy against a wide range of diseases.

Regarding the use of encapsulin-based nanocontainer systems for *in vivo* studies, it is important to address the issue of potential immunogenicity of the xenogeneic proteins. We have already discussed this problem partially: we presently know that, at least, *Quasibacillus thermotolerans* encapsulin-containing cells do not cause an immune response when implanted into mice [59] and rats [60]. In addition, an

article was recently published evaluating *in vivo* behavior of *Thermotoga maritima* encapsulins administered intravenously into mice [61]. The work demonstrated that IV-injected *Thermotoga maritima* encapsulins exhibited an excellent safety profile. The results obtained suggest that encapsulins from bacteria of other strains may also be safe for *in vivo* use.

It is noteworthy that all the described encapsulin-based delivery systems used encapsulins purified from bacteria of various strains. We have shown a possible alternative approach to encapsulin isolation using an eukaryotic cell line. We hope that our results will facilitate further developments of similar techniques.

Conclusion

Undoubtedly, encapsulins currently remain a relatively new object of research; their properties and their original functions in prokaryotes should be comprehensively studied. However, practical applications of encapsulins in the field of biotechnology is becoming increasingly promising. In this study, we describe a new vector tool for delivery of nucleic acids to mesenchymal stem cells. The entire process for obtaining of Mx-Tf-FAM conjugates was carried out under completely aseptic conditions, and that enabled development of a sterile and endotoxin-free delivery system targeted by transferrin receptors. The vectorized Mx encapsulins containing a PAmCherry label can bind transferrin receptors on the surface of mesenchymal stem cells followed by internalization into cells by, presumably, receptor-mediated endocytosis, while maintaining the PAmCherry and FAM fluorescent signals.

Summarizing, compared to nanoplatfroms based on inorganic and/or polymer nanoparticles encapsulin-based nanocontainer systems have a number of advantages. These structures are not only extremely robust. These are completely biodegradable, non-toxic, endotoxin-free protein nanoparticles. The synthesis of encapsulins is genetically based, which, on the one side, means its reproducibility is extremely high and, on the other side, there is a possibility for genetic manipulation. Thus, these features of encapsulins promise significant customization flexibility and broad usability. The obtained nanocarrier can be supplemented not only with nucleic acids, but also with peptides or therapeutic agents for specific delivery to MSCs.

Author contributions

PN provided formal analysis and funding acquisition, AG, NA, DG, ES, and EM carried out experiments and analyzed the data; EM, PM, and NA analyzed the results and provided

suggestions. AG and PN wrote the article. All authors contributed to the article and approved the submitted version.

Data availability statement

The original contributions presented in the study are included in the article/Supplementary Material, further inquiries can be directed to the corresponding author.

Ethics statement

The studies involving humans were approved by the Local Ethics Committee, Medical Research, and Education Center, Lomonosov Moscow State University (IRB00010587). The studies were conducted in accordance with the local legislation and institutional requirements. The participants provided their written informed consent to participate in this study.

References

- Weatherall EL, Avilkina V, Cortes-Araya Y, Dan-Jumbo S, Stenhouse C, Donadeu FX, et al. Differentiation potential of mesenchymal stem/stromal cells is altered by intrauterine growth restriction. *Front Vet Sci* (2020) 7:558905. doi:10.3389/fvets.2020.558905
- Heo JS, Choi Y, Kim HS, Kim HO. Comparison of molecular profiles of human mesenchymal stem cells derived from bone marrow, umbilical cord blood, placenta and adipose tissue. *Int J Mol Med* (2016) 37:115–25. doi:10.3892/ijmm.2015.2413
- Lee WS, Kim HJ, Kim KI, Kim GB, Jin W. Intra-articular injection of autologous adipose tissue-derived mesenchymal stem cells for the treatment of knee osteoarthritis: a phase IIb, randomized, placebo-controlled clinical trial. *Stem Cells Translational Med* (2019) 8:504–11. doi:10.1002/sctm.18-0122
- Zhao X, Ruan J, Tang H, Li J, Shi Y, Li M, et al. Multi-compositional MRI evaluation of repair cartilage in knee osteoarthritis with treatment of allogeneic human adipose-derived mesenchymal progenitor cells. *Stem Cell Res Ther* (2019) 10:308. doi:10.1186/s13287-019-1406-7
- Bolli R, Perin EC, Willerson JT, Yang PC, Traverse JH, Henry TD, et al. Allogeneic mesenchymal cell therapy in anthracycline-induced cardiomyopathy heart failure patients: the CCTRN SENECA trial. *JACC: CardioOncology* (2020) 2:581–95. doi:10.1016/j.jacc.2020.09.001
- He X, Wang Q, Zhao Y, Zhang H, Wang B, Pan J, et al. Effect of intramyocardial grafting collagen scaffold with mesenchymal stromal cells in patients with chronic ischemic heart disease: a randomized clinical trial. *JAMA Netw Open* (2020) 3:e2016236. doi:10.1001/jamanetworkopen.2020.16236
- Uccelli A, Laroni A, Brundin L, Clanet M, Fernandez O, Nabavi SM, et al. MESENCHYMAL Stem cells for Multiple Sclerosis (MESEMS): a randomized, double blind, cross-over phase I/II clinical trial with autologous mesenchymal stem cells for the therapy of multiple sclerosis. *Trials* (2019) 20:263. doi:10.1186/s13063-019-3346-z
- Petrou P, Kassisi I, Levin N, Paul F, Backner Y, Benoliel T, et al. Beneficial effects of autologous mesenchymal stem cell transplantation in active progressive multiple sclerosis. *Brain* (2020) 143:3574–88. doi:10.1093/brain/awaa333
- Namestnikova DD, Gubskiy IL, Revkova VA, Sukhinich KK, Melnikov PA, Gabashvili AN, et al. Intra-arterial stem cell transplantation in experimental stroke in rats: real-time MR visualization of transplanted cells starting with their first pass through the brain with regard to the therapeutic action. *Front Neurosci* (2021) 15:641970. doi:10.3389/fnins.2021.641970
- Powell SB, Silvestri JM. Safety of intratracheal administration of human umbilical cord blood derived mesenchymal stromal cells in extremely low birth weight preterm infants. *J Pediatr* (2019) 210:209–13.e2. doi:10.1016/j.jpeds.2019.02.029
- Yang YHK, Ogando CR, Wang See C, Chang TY, Barabino GA. Changes in phenotype and differentiation potential of human mesenchymal stem cells aging *in vitro*. *Stem Cell Res Ther* (2018) 9:131. doi:10.1186/s13287-018-0876-3
- Oggu GS, Sasikumar S, Reddy N, Ella KKR, Rao CM, Bokara KK. Gene delivery approaches for mesenchymal stem cell therapy: strategies to increase efficiency and specificity. *Stem Cell Rev Rep* (2017) 13:725–40. doi:10.1007/s12015-017-9760-2
- Kalidasan V, Ng WH, Ishola OA, Ravichantar N, Tan JJ, Das KT. A guide in lentiviral vector production for hard-to-transfect cells, using cardiac-derived c-kit expressing cells as a model system. *Sci Rep* (2021) 11:19265. doi:10.1038/s41598-021-98657-7
- Tsulaia TV, Prokopishyn NL, Yao A, Carsrud NV, Carou MC, Brown DB, et al. Glass needle-mediated microinjection of macromolecules and transgenes into primary human mesenchymal stem cells. *J Biomed Sci* (2003) 10:328–36. doi:10.1159/000070098
- Cervia LD, Chang CC, Wang L, Mao M, Yuan F. Enhancing electroporation efficiency through improvement in nuclear entry of plasmid DNA. *Mol Ther - Nucleic Acids* (2018) 11:263–71. doi:10.1016/j.omtn.2018.02.009
- Elizarova TN, Antopolsky ML, Novichikhin DO, Skirda AM, Orlov AV, Bragina VA, et al. A straightforward method for the development of positively charged gold nanoparticle-based vectors for effective siRNA delivery. *Molecules* (2023) 28:3318. doi:10.3390/molecules28083318
- Gonzalez-Fernandez T, Sathy BN, Hobbs C, Cunniffe GM, McCarthy HO, Dunne NJ, et al. Mesenchymal stem cell fate following non-viral gene transfection strongly depends on the choice of delivery vector. *Acta Biomater* (2017) 55:226–38. doi:10.1016/j.actbio.2017.03.044
- Sizikov AA, Nikitin PI, Nikitin MP. Magnetofection *in vivo* by nanomagnetic carriers systemically administered into the bloodstream. *Pharmaceutics* (2021) 13:1927. doi:10.3390/pharmaceutics13111927
- Stewart MP, Langer R, Jensen KF. Intracellular delivery by membrane disruption: mechanisms, strategies, and concepts. *Chem Rev* (2018) 118:7409–531. doi:10.1021/acs.chemrev.7b00678
- Gabashvili AN, Chmelyuk NS, Oda VV, Leonova MK, Sarkisova VA, Lazareva PA, et al. Magnetic and fluorescent dual-labeled genetically encoded targeted nanoparticles for malignant glioma cell tracking and drug delivery. *Pharmaceutics* (2023) 15:2422. doi:10.3390/pharmaceutics15102422
- Moon H, Lee J, Min J, Kang S. Developing genetically engineered encapsulin protein cage nanoparticles as a targeted delivery nanopatform. *Biomacromolecules* (2014) 15:3794–801. doi:10.1021/bm501066m

Funding

The author(s) declare that financial support was received for the research, authorship, and/or publication of this article. The study was supported by the Ministry of Science and Higher Education of the Russian Federation, contract No. 075-15-2022-315.

Conflict of interest

The authors declare that the research was conducted in the absence of any commercial or financial relationships that could be construed as a potential conflict of interest.

Supplementary material

The Supplementary Material for this article can be found online at: <https://www.ebm-journal.org/articles/10.3389/ebm.2024.10055/full#supplementary-material>

22. Van de Steen A, Khalife R, Colant N, Mustafa Khan H, Deveikis M, Charalambous S, et al. Bioengineering bacterial encapsulin nanocompartments as targeted drug delivery system. *Synth Syst Biotechnol* (2021) **6**:231–41. doi:10.1016/j.synbio.2021.09.001
23. Kwon S, Giessen TW. Engineered protein nanocages for concurrent RNA and protein packaging *in vivo*. *ACS Synth Biol* (2022) **11**:3504–15. doi:10.1021/acssynbio.2c00391
24. Almeida AV, Carvalho AJ, Calmeiro T, Jones NC, Hoffmann SV, Fortunato E, et al. Condensation and protection of DNA by the *Myxococcus xanthus* encapsulin: a novel function. *Int J Mol Sci* (2022) **23**:7829. doi:10.3390/ijms23147829
25. McHugh CA, Fontana J, Nemecek D, Cheng N, Aksyuk AA, Heymann JB, et al. A virus capsid-like nanocompartment that stores iron and protects bacteria from oxidative stress. *EMBO J* (2014) **33**:1896–911. doi:10.15252/embj.201488566
26. Gabashvili AN, Chmelyuk NS, Sarkisova VA, Melnikov PA, Semkina AS, Nikitin AA, et al. *Myxococcus xanthus* encapsulin as a promising platform for intracellular protein delivery. *Int J Mol Sci* (2022) **23**:15591. doi:10.3390/ijms232415591
27. Thermo Fisher StemPro® osteogenesis differentiation kit (2024). Available from: <https://www.thermofisher.com/document-connect/document-connect.html?url=https://assets.thermofisher.com/TFS-Assets%2FSLG%2Fmanuals%2FStemProOsteoDiff.pdf> (Accessed March 29, 2024).
28. Thermo Fisher StemPro® chondrogenesis differentiation kit (2024). Available from: https://www.thermofisher.com/document-connect/document-connect.html?url=https://assets.thermofisher.com/TFS-Assets%2FSLG%2Fmanuals%2Fstempro_chondro_diff_man.pdf (Accessed March 29, 2024).
29. Thermo Fisher StemPro® adipogenesis differentiation kit (2024). Available from: <https://www.thermofisher.com/document-connect/document-connect.html?url=https://assets.thermofisher.com/TFS-Assets%2FSLG%2Fmanuals%2FStemProAdipoDiffKit.pdf> (Accessed March 29, 2024).
30. Miltenyi Biotec MSC phenotyping Cocktail kit, anti-human, REAfinity™ (2022). Available from: <https://static.miltenyibiotec.com/asset/150655405641/document-1bt1iceg8ti5jgiq2gkfq6?content-disposition=inline> (Accessed March 29, 2024).
31. Mochalova EN, Kotov IA, Lifanov DA, Chakraborti S, Nikitin MP. Imaging flow cytometry data analysis using convolutional neural network for quantitative investigation of phagocytosis. *Biotechnol Bioeng* (2022) **119**:626–35. doi:10.1002/bit.27986
32. Bragina VA, Khomyakova E, Orlov AV, Znoyko SL, Mochalova EN, Paniushkina L, et al. Highly sensitive nanomagnetic quantification of extracellular vesicles by immunochromatographic strips: a tool for liquid biopsy. *Nanomaterials (Basel)* (2022) **12**:1579. doi:10.3390/nano12091579
33. CIF A basic guide to particle characterization (2015). Available from: https://www.cif.iastate.edu/sites/default/files/uploads/Other_Inst/Particle%20Size/Particle%20Characterization%20Guide.pdf (Accessed March 29, 2024).
34. Banaszynski LA, Chen LC, Maynard-Smith LA, Ooi AG, Wandless TJ. A rapid, reversible, and tunable method to regulate protein function in living cells using synthetic small molecules. *Cell* (2006) **126**:995–1004. doi:10.1016/j.cell.2006.07.025
35. Eren E, Wang B, Winkler DC, Watts NR, Steven AC, Wingfield PT. Structural characterization of the *Myxococcus xanthus* encapsulin and ferritin-like cargo system gives insight into its iron storage mechanism. *Structure* (2022) **30**:551–63.e4. doi:10.1016/j.str.2022.01.008
36. Singh P, Pandit S, Mokkapat V, Garg A, Ravikumar V, Mijakovic I. Gold nanoparticles in diagnostics and therapeutics for human cancer. *Int J Mol Sci* (2018) **19**:1979. doi:10.3390/ijms19071979
37. Nikitin MP, Zelepukin IV, Shipunova VO, Sokolov IL, Deyev SM, Nikitin PI. Enhancement of the blood-circulation time and performance of nanomedicines via the forced clearance of erythrocytes. *Nat Biomed Eng* (2020) **4**:717–31. doi:10.1038/s41551-020-0581-2
38. Ostroverkhov PV, Semkina AS, Naumenko VA, Plotnikova EA, Melnikov PA, Abakumova T, et al. Synthesis and characterization of bacteriochlorin loaded magnetic nanoparticles (MNP) for personalized MRI guided photosensitizers delivery to tumor. *J Colloid Interf Sci* (2019) **537**:132–41. doi:10.1016/j.jcis.2018.10.087
39. Tregubov A, Sokolov I, Babenyshev A, Nikitin P, Cherkasov V, Nikitin M. Magnetic hybrid magnetite/metal organic framework nanoparticles: facile preparation, post-synthetic biofunctionalization and tracking *in vivo* with magnetic methods. *J Magnetism Magn Mater* (2018) **449**:590–6. doi:10.1016/j.jmmm.2017.10.070
40. Ringaci A, Yaremenko A, Shevchenko K, Zvereva S, Nikitin M. Metal-organic frameworks for simultaneous gene and small molecule delivery *in vitro* and *in vivo*. *Chem Eng J* (2021) **418**:129386. doi:10.1016/j.cej.2021.129386
41. Lee SW, Kim YM, Cho CH, Kim YT, Kim SM, Hur SY, et al. An open-label, randomized, parallel, phase II trial to evaluate the efficacy and safety of a cremophor-free polymeric micelle formulation of paclitaxel as first-line treatment for ovarian cancer: a Korean gynecologic oncology group study (KGOG-3021). *Cancer Res Treat* (2018) **50**:195–203. doi:10.4143/crt.2016.376
42. Kovalenko VL, Komedchikova EN, Sogomonyan AS, Tereshina ED, Kolesnikova OA, Mirkasymov AB, et al. Lectin-modified magnetic nano-PLGA for photodynamic therapy *in vivo*. *Pharmaceutics* (2022) **15**:92. doi:10.3390/pharmaceutics15010092
43. Bae Y, Kim GJ, Kim H, Park SG, Jung HS, Kang S. Engineering tunable dual functional protein cage nanoparticles using bacterial superglue. *Biomacromolecules* (2018) **19**:2896–904. doi:10.1021/acs.biomac.8b00457
44. Palombarini F, Masciarelli S, Incocciati A, Liscardo F, Di Fabio E, Iazzetti A, et al. Self-assembling ferritin-dendrimer nanoparticles for targeted delivery of nucleic acids to myeloid leukemia cells. *J Nanobiotechnology* (2021) **19**:172. doi:10.1186/s12951-021-00921-5
45. Orlov AV, Nikitin MP, Bragina VA, Znoyko SL, Zaikina MN, Ksenevich TI, et al. A new real-time method for investigation of affinity properties and binding kinetics of magnetic nanoparticles. *J Magnetism Magn Mater* (2015) **380**:231–5. doi:10.1016/j.jmmm.2014.10.019
46. Sanna V, Sechi M. Therapeutic potential of targeted nanoparticles and perspective on nanotherapies. *ACS Med Chem Lett* (2020) **11**:1069–73. doi:10.1021/acsmchemlett.0c00075
47. Mohammadpour R, Ghandehari H. Mechanisms of immune response to inorganic nanoparticles and their degradation products. *Adv Drug Deliv Rev* (2022) **180**:114022. doi:10.1016/j.addr.2021.114022
48. Stepien G, Moros M, Perez-Hernandez M, Monge M, Gutierrez L, Fratila RM, et al. Effect of surface chemistry and associated protein corona on the long-term biodegradation of iron oxide nanoparticles *in vivo*. *ACS Appl Mater Inter* (2018) **10**:4548–60. doi:10.1021/acsami.7b18648
49. Liu Y, Li J. Self-assembling nanoarchitectonics of size-controllable celastrol nanoparticles for efficient cancer chemotherapy with reduced systemic toxicity. *J Colloid Interf Sci* (2023) **636**:216–22. doi:10.1016/j.jcis.2022.12.162
50. Putri RM, Allende-Ballester C, Luque D, Klem R, Rouso KA, Liu A, et al. Structural characterization of native and modified encapsulins as nanoplatforms for *in vitro* catalysis and cellular uptake. *ACS Nano* (2017) **11**:12796–804. doi:10.1021/acsnano.7b07669
51. Zhang D, Lee HF, Pettit SC, Zaro JL, Huang N, Shen WC. Characterization of transferrin receptor-mediated endocytosis and cellular iron delivery of recombinant human serum transferrin from rice (*Oryza sativa* L.). *BMC Biotechnol* (2012) **12**:92. doi:10.1186/1472-6750-12-92
52. Gu Z, Wang H, Xia J, Yang Y, Jin Z, Xu H, et al. Decreased ferroportin promotes myeloma cell growth and osteoclast differentiation. *Cancer Res* (2015) **75**:2211–21. doi:10.1158/0008-5472.can-14-3804
53. Ohkuma M, Haraguchi N, Ishii H, Mimori K, Tanaka F, Kim HM, et al. Absence of CD71 transferrin receptor characterizes human gastric adenocarcinoma stem cells. *Ann Surg Oncol* (2012) **19**:1357–64. doi:10.1245/s10434-011-1739-7
54. Singh M, Mugler K, Hailoo DW, Burke S, Nemesure B, Torkko K, et al. Differential expression of transferrin receptor (TfR) in a spectrum of normal to malignant breast tissues: implications for *in situ* and invasive carcinoma. *Appl Immunohistochem Mol Morphol* (2011) **19**:417–23. doi:10.1097/pai.0b013e318209716e
55. Czarnywojtek A, Borowska M, Dyrka K, Van Gool S, Sawicka-Gutaj N, Moskal J, et al. Glioblastoma multiforme: the latest diagnostics and treatment techniques. *Pharmacology* (2023) **108**:423–31. doi:10.1159/000531319
56. Nikitin MP. Non-complementary strand commutation as a fundamental alternative for information processing by DNA and gene regulation. *Nat Chem* (2023) **15**:70–82. doi:10.1038/s41557-022-01111-y
57. Vasileva AV, Gladkova MG, Ashniev GA, Osintseva ED, Orlov AV, Kravchuk EV, et al. Super-enhancers and their parts: from prediction efforts to pathogenomic status. *Int J Mol Sci* (2024) **25**:3103. doi:10.3390/ijms25063103
58. Moeinabadi-Bidgoli K, Mazloomnejad R, Beheshti Maal A, Asadzadeh Aghdaei H, Kazem Arki M, Hossein-Khannazer N, et al. Genetic modification and preconditioning strategies to enhance functionality of mesenchymal stromal cells: a clinical perspective. *Expert Opin Biol Ther* (2023) **23**:461–78. doi:10.1080/14712598.2023.2205017
59. Gabashvili AN, Efremova MV, Vodopyanov SS, Chmelyuk NS, Oda VV, Sarkisova VA, et al. New approach to non-invasive tumor model monitoring via self-assemble iron containing protein nanocompartments. *Nanomaterials* (2022) **12**:1657. doi:10.3390/nano12101657
60. Fedotov K, Efremova M, Gabashvili A, Semkina A, Sigmund F, Sarkisova V, et al. Towards multiscale tracking of stem cells with genetically encoded encapsulin nanocompartments. *FEBS OPEN BIO* (2021) **273**–3. WILEY 111 RIVER ST, HOBOKEN 07030-5774, NJ USA.
61. Rennie C, Sives C, Boyton I, Diaz D, Gorrie C, Vittorio O, et al. *In vivo* behavior of systemically administered encapsulin protein nanocages and implications for their use in targeted drug delivery. *Adv Ther* (2024) **7**:2300360. doi:10.1002/adtp.202300360



OPEN ACCESS

*CORRESPONDENCE

Dong Wang,
✉ wdong@mail.sysu.edu.cn

RECEIVED 05 June 2023

ACCEPTED 07 October 2023

PUBLISHED 09 April 2024

CITATION

Zhu X, Liu Y, Huang Y, Tan H, He M and Wang D (2024), Establishment and validation of a 5-factor diagnostic model for obstructive and non-obstructive azoospermia based on routine clinical parameters.
Exp. Biol. Med. 249:10137.
doi: 10.3389/ebm.2024.10137

COPYRIGHT

© 2024 Zhu, Liu, Huang, Tan, He and Wang. This is an open-access article distributed under the terms of the [Creative Commons Attribution License \(CC BY\)](#). The use, distribution or reproduction in other forums is permitted, provided the original author(s) and the copyright owner(s) are credited and that the original publication in this journal is cited, in accordance with accepted academic practice. No use, distribution or reproduction is permitted which does not comply with these terms.

Establishment and validation of a 5-factor diagnostic model for obstructive and non-obstructive azoospermia based on routine clinical parameters

Xiaoyu Zhu¹, Yin Liu¹, Ying Huang², Hongxia Tan¹, Meifang He³ and Dong Wang^{1,2*}

¹Department of Laboratory Medicine, The First Affiliated Hospital, Sun Yat-sen University, Guangzhou, China, ²Department of Laboratory Medicine, Guangxi Hospital Division of The First Affiliated Hospital, Sun Yat-sen University, Nanning, China, ³Laboratory of General Surgery, The First Affiliated Hospital, Sun Yat-sen University, Guangzhou, China

Abstract

Azoospermia is a serious leading male-factor cause of infertility in couples of childbearing age. The two main azoospermia types, obstructive (OA) and non-obstructive (NOA) azoospermia, differ in their treatment approaches. Therefore, their clinical diagnosis is extremely important, requiring an accurate, efficient, and easy-to-use diagnostic model. This retrospective observational study included 707 patients with azoospermia treated between 2017 and 2021, 498 with OA, and 209 with NOA. Hematological and seminal plasma parameters, hormone levels, and testicular volume were used in logistic regression analysis to evaluate and compare their diagnostic performance, results showed that the optimal diagnostic model is constructed by five variables including semen volume, semen pH, seminal plasma neutral α -glucosidase activity, follicle-stimulating hormone in the serum, and testicular volume, compared with follicle-stimulating hormone-based and testicular volume-based models. The 5-factor diagnostic model had an accuracy of 90.4%, sensitivity of 96.4%, positive predictive value of 90.6%, negative predictive value of 89.8%, and area under the curve of 0.931, all higher than in the other two models. However, its specificity (76.1%) was slightly lower than in the other models. Meantime, the internal 5-fold cross-validation results indicated that the 5-factor diagnostic model had a good clinical application value. This study established an accurate, efficient, and relatively accessible 5-factor diagnostic model for OA and NOA, providing a reference for clinical decision-making when selecting an appropriate treatment.

KEYWORDS

azoospermia, diagnostic model, follicle-stimulating hormone (FSH), seminal plasma, testicular volume

Impact statement

At present, the incidence of male infertility is gradually increasing, and many couples of childbearing age suffer from it. Among them, azoospermia is one of the most common and serious causes of male infertility, mainly divided into obstructive azoospermia and non-obstructive azoospermia. The optimal treatment options for the two types of azoospermia are different, so clinically accurate and efficient differentiation is required. In this study, a highly accurate diagnostic model was established using clinical routine parameters such as semen volume, semen pH, seminal plasma neutral α -glucosidase activity and follicle-stimulating hormone, as well as testicular volume. Compared with the traditional gold standard “testicular biopsy,” this model is simple, non-invasive, efficient and accurate, which can provide a good reference for clinical decision-making, and its practical application value needs to be tested in a larger population.

Introduction

The incidence of male infertility is increasing. It has been reported that about 10–15% of all couples of reproductive age face fertility-related problems, and about 50–60% of these can be attributed to males [1–3]. Azoospermia is a common and the most severe cause of male infertility, affecting approximately 10–15% of infertile males [4–6]. Azoospermia means that no spermatozoa are found in two or more ejaculated semen samples [6]. Azoospermia is divided into obstructive (OA) and non-obstructive (NOA) azoospermia types. In OA, spermatogenesis is normal, but the sperm cannot be excreted normally due to mechanical obstruction along the reproductive tract, including the vas deferens, epididymis, and ejaculatory ducts. The spermatogenic dysfunction of NOA is associated with inherent defects in the testes caused by various factors that severely affect the process, usually resulting in primary testicular failure or dysfunction of the hypothalamic-pituitary-gonadal axis [4, 6].

Advances in sperm retrieval and microsurgical techniques make it possible for more couples with infertility to have progeny. The two azoospermia types are clinically treated differently to achieve the best therapeutic effect. Patients with OA are often referred for surgical removal of obstruction, while those with NOA may require assisted reproductive technologies, including microdissection testicular sperm extraction [7]. Particularly, in some cases, in addition to conventional microsurgical reconstruction operations such as vasoepididymistomy, patients with epididymis obstruction or inguinal vessel obstruction can also be offered percutaneous epididymal sperm aspiration (PESA), microsurgical epididymal sperm aspiration (MESA), or testicular sperm aspiration (TESA), and patients with

intratesticular obstruction can take conventional testicular sperm extraction (TESE) [3, 8]. Therefore, an accurate diagnosis of the azoospermia type is very important for clinical treatment selection. A comprehensive clinical assessment is made to clarify the azoospermia type, comprising the results of medical history, physical examination, semen analysis, hormone evaluation, genetic testing, and various imaging examinations. These can lead to a definite diagnosis in over 90% of the patients with azoospermia; however, this comprehensive evaluation is time- and workforce-demanding, significantly increasing the diagnostic and treatment costs. Furthermore, a definite diagnosis cannot be reached for some patients, requiring testicular biopsy, the gold standard for OA and NOA diagnosis. However, a biopsy might cause testicular damage, so the relevant guidelines do not recommend using this method as a routine diagnostic tool to determine the azoospermia type [4]. An accurate and efficient clinical diagnostic model that can reduce the diagnosis and treatment costs for patients with azoospermia; however, such diagnostic models of azoospermia are scarce and limited. Studies have shown that males with elevated serum follicle-stimulating hormone (FSH) and reduced testosterone/FSH ratio are more likely to have abnormal semen analysis [9], reflecting lesions in the male genitourinary system [10]. The FSH-based model established by Tradewell et al. was good at predicting the probability of azoospermia but could not be used for differential diagnosis [11].

This study aimed to construct a clinical diagnostic model to differentiate between OA and NOA using conventional clinical parameters such as testicular volume, seminal plasma composition, and hormone levels. The receiver operating characteristic (ROC) curve was used to assess the diagnostic ability of the developed models and identify the optimal one. Such a model would be a valuable clinical tool for azoospermia diagnosis, ultimately providing a preliminary reference for selecting appropriate clinical treatment methods.

Materials and methods

Study population

This retrospective study included 707 patients with azoospermia treated at the First Affiliated Hospital of Sun Yat-Sen University between 2017 and 2021, 498 with OA, and 209 with NOA. All patients were diagnosed by ultrasonographic examination of the urogenital system and testicular biopsy. Among them, 493 patients underwent testicular biopsy in dedicated Fertility Center Laboratory of the hospital. According to histopathological results, it was diagnosed as OA if spermatogenic cells and mature spermatozoa at all levels can be seen in the seminiferous tubules, and the number is generally

normal or slightly reduced, and/or there is obstruction or absence of the epididymis, vas deferens, or ejaculatory ducts according to the ultrasound results; while the presence of markedly reduced testicular volume, cryptorchidism, or testicular parenchymal lesions was diagnosed as NOA. However, most patients were diagnosed as NOA when biopsy results showed that all levels of spermatogenic cells with a small amount of mature spermatozoa could be seen in the seminiferous tubules, significantly reduced mature spermatozoa or even azoospermia or Sertoli cell-only syndrome, or ultrasonography showed substantial changes in the testicles, and only a few patients were diagnosed as OA as the ultrasound results showed obstruction, semen stasis, or reproductive duct deficiency. The remaining 214 patients did not undergo testicular biopsy, and the diagnosis was mainly based on clinical manifestations and ultrasound results, including whether there was obstruction, absence of reproductive tract, and testicular volume, et al. During the testicular biopsy, the laboratory will immediately cryopreserve all the viable sperm if any of them are extracted. Patients with liver, kidney, hypothalamic-pituitary, and other reproductive system diseases were excluded.

Data collection

The following data were retrieved from the institute's database to construct the models: age; hematological parameters, including absolute values of leukocytes, neutrophils, monocytes, lymphocytes, eosinophils, basophils, red blood cells (RBC), and platelets, mean corpuscular volume, and hemoglobin; semen and seminal plasma analysis, including semen volume, pH, seminal fructose and elastase concentrations, seminal plasma neutral α -glucoside activity (SPNG); serum levels of FSH, luteinizing hormone (LH), testosterone, progesterone, estradiol, and prolactin; testicular volume.

Establishment and evaluation of the model

The OA and NOA groups were compared using nonparametric tests to screen for significantly different parameters. The parameters selected for inclusion in the initial logistic regression model were RBC, hemoglobin, platelets, semen volume, semen pH, seminal fructose, SPNG, FSH, LH, testosterone, prolactin, and testicular volume. Independent variables with a significant ($p < 0.05$) impact on the outcome were further screened to establish possible diagnostic models. Finally, we used the area under the ROC curve (AUC) to calculate the accuracy, sensitivity, specificity, positive predictive value (PPV), and negative predictive value (NPV) of the models. The diagnostic performance of the models was evaluated (see below), and the optimal one was selected.

Internal validation of the model

The internal validation of the model tested its generalization ability and evaluated its clinical application value. We used the machine learning tool in the DxAI intelligent scientific research platform (Deepwise, Beijing, China) with a 5-fold cross-validation method to validate the model. This validation method randomly divides all the research subjects into five average groups, using four groups as a training set and the fifth as a validation set. This process was repeated, using each time a different group as the validation set. The average value of the five evaluation results was used as the final evaluation indicator. The assessed metrics included the AUC, accuracy, sensitivity, specificity, PPV, and NPV.

Statistical analysis

This study used IBM SPSS Statistics for Windows, Version 20.0 (IBM Corp., Armonk, NY, United States) for data analysis. The Kolmogorov-Smirnov test assessed whether the variables were normally distributed. Continuous variables are described as medians (interquartile ranges), and categorical variables as frequencies (percentages). The Kolmogorov-Smirnov test compared continuous variables between two independent samples, and the Mann-Whitney U test compared categorical variables. Missing data values were completed using the expectation-maximization model. Binary logistic regression was used for multivariate analysis to obtain the corresponding diagnostic model. The stepwise regression method (forward-likelihood ratio) was used to screen independent variables, that is, the independent variables are introduced into the regression equation one by one, and the models with and without an independent variable are compared by the likelihood ratio statistic, and if there is statistical significance, the independent variable is included in the model, and *vice versa*, until no independent variable can be introduced. The models' ability to differentiate OA from NOA was evaluated using ROC analysis, and the MedCalc, Version 20.115 (MedCalc Software Ltd., Ostend, Belgium) was used for comparison of different ROC curves. The machine learning process was carried out on the DxAI intelligent scientific research platform. All tests were two-sided, and the significance level was set at $p < 0.05$.

Results

Demographic and clinical characteristics of the research subjects

During the study period, 707 patients (median age is 30, IQR is 6) with azoospermia were admitted to the First Affiliated

TABLE 1 Demographic and clinical characteristics of OA and NOA groups.

Variable	NOA (<i>n</i> = 209)	OA (<i>n</i> = 498)	<i>p</i> -value
Age (years)	30.00 (6.00)	30.00 (7.00)	0.72
Leukocytes (×10 ⁹ /L)	6.93 (2.39)	6.98 (2.02)	0.75
Neutrophils (×10 ⁹ /L)	3.99 (1.89)	4.00 (1.69)	0.55
Monocytes (×10 ⁹ /L)	0.49 (0.18)	0.49 (0.20)	0.98
Lymphocytes (×10 ⁹ /L)	2.16 (0.75)	2.19 (0.79)	0.99
Eosinophils (×10 ⁹ /L)	0.12 (0.14)	0.13 (0.17)	0.16
Basophils (×10 ⁹ /L)	0.03 (0.03)	0.03 (0.03)	0.85
RBC (×10 ¹² /L)	5.16 (0.64)	5.28 (0.54)	0.002 **
MCV (fL)	88.45 (5.27)	88.80 (5.80)	0.29
Hemoglobin (g/L)	152.00 (14.00)	157.00 (13.50)	0.000 **
Platelets (×10 ⁹ /L)	259.00 (79.50)	241.00 (71.00)	0.002 **
Semen volume (mL)	3.50 (2.00)	1.60 (1.70)	0.000 **
Semen pH	7.50 (0.00)	7.50 (1.00)	0.000 **
Seminal plasma fructose (μmol)	28.90 (43.85)	2.90 (16.25)	0.000 **
SPNG (mU)	24.80 (39.75)	2.90 (8.35)	0.000 **
Seminal plasma elastase (ng/mL)	169.20 (472.35)	205.80 (827.85)	0.14
FSH (IU/L)	14.69 (13.05)	3.67 (2.32)	0.000 **
LH (IU/L)	5.08 (3.58)	2.84 (1.69)	0.000 **
Testosterone (ng/mL)	3.97 (2.81)	4.89 (2.69)	0.000 **
Progesterone (ng/mL)	0.30 (0.20)	0.30 (0.10)	0.72
Estradiol (pg/mL)	21.00 (13.00)	21.00 (12.00)	0.96
Prolactin (ng/mL)	12.13 (10.55)	10.35 (6.04)	0.000 **
Testicular size			
Bilateral small testes or cryptorchidism	172 (82.3%)	142 (28.5%)	0.000 **
Unilateral small testis or absence/cryptorchidism	13 (6.2%)	90 (18.1%)	
Bilateral normal testicular volume	22 (10.5%)	222 (44.6%)	
Unilateral or bilateral large testicular volume	2 (1.0%)	44 (8.8%)	

*******p* < 0.01. OA, obstructive azoospermia; NOA, non-obstructive azoospermia; SPNG, seminal plasma neutral α-glucosidase activity; FSH, follicle-stimulating hormone; RBC, red blood cells; LH, luteinizing hormone; MCV, mean corpuscular volume.
The bold values mean significant different variable between OA and NOA.

Hospital of Sun Yat-sen University, 209 with NOA and 498 with OA. The clinical characteristics, hematological parameters, semen and seminal plasma parameters, serum hormone levels, and testicular volume of the two groups are summarized in Table 1. The analysis results showed that the RBC, hemoglobin, and testosterone in the OA group were significantly higher (*p* < 0.01) and FSH, LH, and prolactin significantly lower (*p* < 0.01) than in the NOA group. The groups also differed significantly in testicular volume (*p* < 0.01). Based on a normal testicular volume of 12–19 mL [13], 88.5% of the patients in the NOA group had unilateral or bilateral testicular volume reduction or cryptorchidism, while this was found in only 46.6% of the

patients in the OA group. Nearly half (44.6%) of the OA group had normal testicular volume compared with 10.5% of the NOA group. Other indicators, such as age, the total number of leukocytes and their components, mean corpuscular volume, seminal plasma elastase, progesterone, and estradiol levels, were similar in both groups.

Establishment and evaluation of the model

We included indicators significantly different between the OA and NOA groups as candidates for the logistic regression

TABLE 2 Three diagnostic model types to differentiate OA from NOA with their independent variables.

Model	Variable	B	p-value	OR (95% CI)
Model 1	Constant	15.131	0.000**	3726840.721
	Semen volume	−0.263	0.002**	0.769 (0.652–0.907)
	Semen pH	−1.090	0.003**	0.336 (0.164–0.690)
	SPNG	−0.015	0.002**	0.986 (0.977–0.994)
	FSH	−0.192	0.000**	0.826 (0.785–0.868)
	Testicular size		0.000**	
	Testicular size (1)	−4.362	0.017*	0.013 (0.000–0.457)
	Testicular size (2)	−2.918	0.116	0.054 (0.001–2.055)
	Testicular size (3)	−2.861	0.121	0.057 (0.002–2.138)
Model 2	Constant	3.091	0.000**	22.000
	Testicular size		0.000**	
	Testicular size (1)	−3.283	0.000**	0.038 (0.009–0.157)
	Testicular size (2)	−1.156	0.139	0.315 (0.068–1.456)
	Testicular size (3)	−0.779	0.303	0.459 (0.104–2.021)
Model 3	Constant	3.326	0.000**	27.814
	FSH	−0.308	0.000**	0.735 (0.699–0.773)

* $p < 0.05$, ** $p < 0.01$. Note: The testicular size was used as an ordered multi-categorical variable. It was assigned a value of 1 for bilateral small testes or cryptorchidism, 2 for unilateral small testis or absence/cryptorchidism, 3 for bilateral normal testicular volume, and 4 for unilateral or bilateral large testicular volume.
OA, obstructive azoospermia; NOA, non-obstructive azoospermia; SPNG, seminal plasma neutral α -glucosidase activity; FSH, follicle-stimulating hormone; OR, odds ratio; CI, confidence interval.
The bold values mean independent risk factors in each diagnostic model screened through the logistic regression analysis.

analysis and screened independent variables with the stepwise regression method (forward-LR) to avoid including too many independent variables and minimize the influence of irrelevant ones, improving the diagnostic model performance. Finally, a diagnostic model was established with five variables, including semen volume, semen pH, SPNG, FSH, and testicular volume (Model 1). Since the testicular volume had the greatest impact on the diagnostic results in the logistic regression model (odds ratio, 0.013; 95% confidence interval, 0.000–0.457, $p = 0.017$), it was used as an independent risk factor to establish a new diagnostic model (Model 2). Furthermore, FSH has been used alone to predict azoospermia [11] and as a diagnostic criterion for NOA [6, 12]. Therefore, we used FSH as an independent risk factor to establish another diagnostic model (Model 3). The logistic regression analysis results of the three models are shown in Table 2, and their ROC curves are shown in Figure 1. The three models were compared for accuracy, sensitivity, specificity, PPV, NPV, and AUC (in Table 3), showing that the diagnosis accuracy of Model 1 (90.4%) was higher than that of Models 2 (74.7%) and 3 (87.1%). The AUC of Model 1 (0.931) was significantly larger than that of Model 2 (0.778, $p < 0.01$) and Model 3 (0.908, $p < 0.01$).

Model verification

We conducted a 5-fold cross-validation of Model 1 to verify its generalization ability and evaluate the effectiveness of its diagnostic performance (Figure 2). The results showed that the training and validation sets had an accuracy of 88.0%. Moreover, its sensitivity, specificity, and PPV were all above 80%; however, the NPV was slightly lower than in the other two models. Notably, the AUCs of the training and validation sets were 0.938 and 0.928, respectively, indicating that Model 1 could accurately distinguish OA from NOA (Table 4; Figures 3A, B).

Discussion

This study screened clinical, hematological, and seminal plasma parameters, hormone levels, and testicular volume in patients with OA and NOA to construct diagnostic models. The selected diagnostic model to distinguish OA from NOA included semen volume, semen pH, SPNG, FSH, and testicular volume (AUC of 0.931). We used cross-validation to confirm the clinical diagnostic validity of this model.

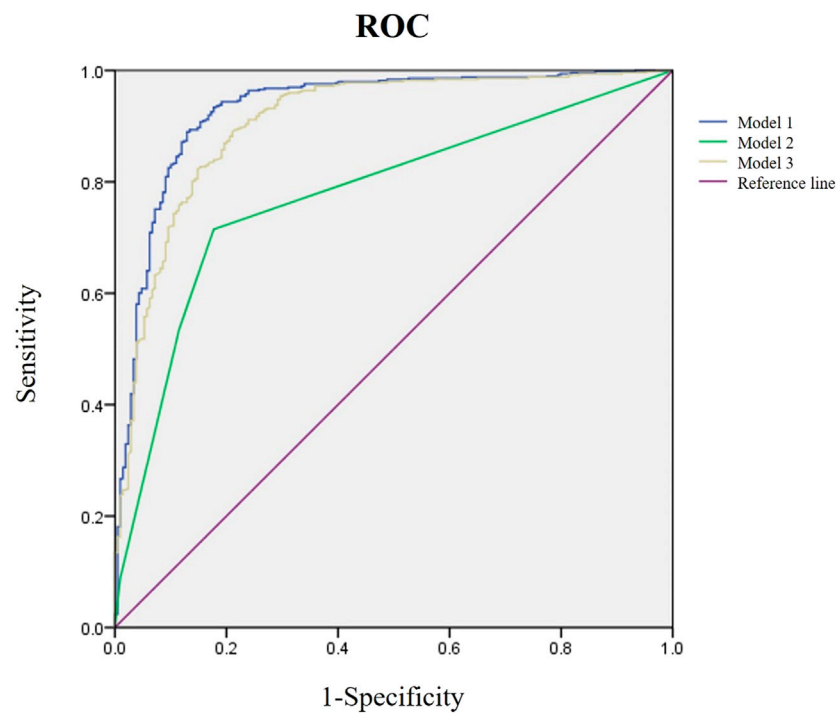


FIGURE 1 Receiver operating characteristic (ROC) analysis of three diagnostic models. The purple line is the reference, the blue is Model 1, the green is Model 2, and the yellow is Model 3.

TABLE 3 Efficacy evaluation of three diagnostic models for OA and NOA.

Models	Accuracy (%)	Sensitivity (%)	Specificity (%)	PPV (%)	NPV (%)	AUC
Model 1	90.4	96.4	76.1	90.6	89.8	0.931
Model 2	74.7	71.5	82.3	90.6	54.8	0.778
Model 3	87.1	96.8	64.1	86.5	89.3	0.908

OA, obstructive azoospermia; NOA, non-obstructive azoospermia; PPV, positive predictive value; NPV, negative predictive value; AUC, area under the receiver operating characteristic curve.

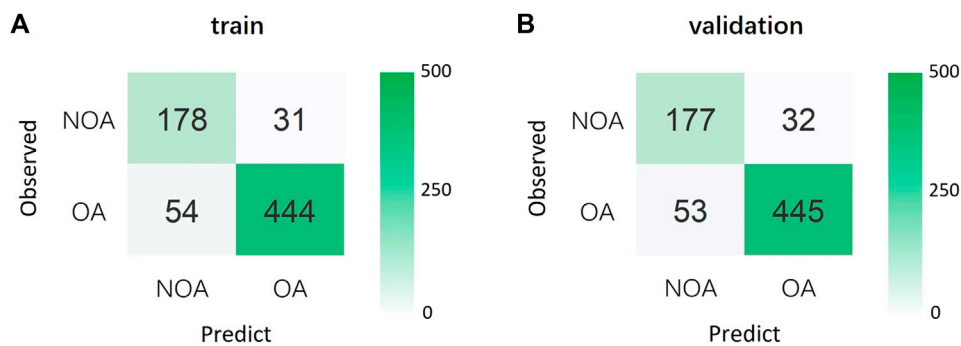
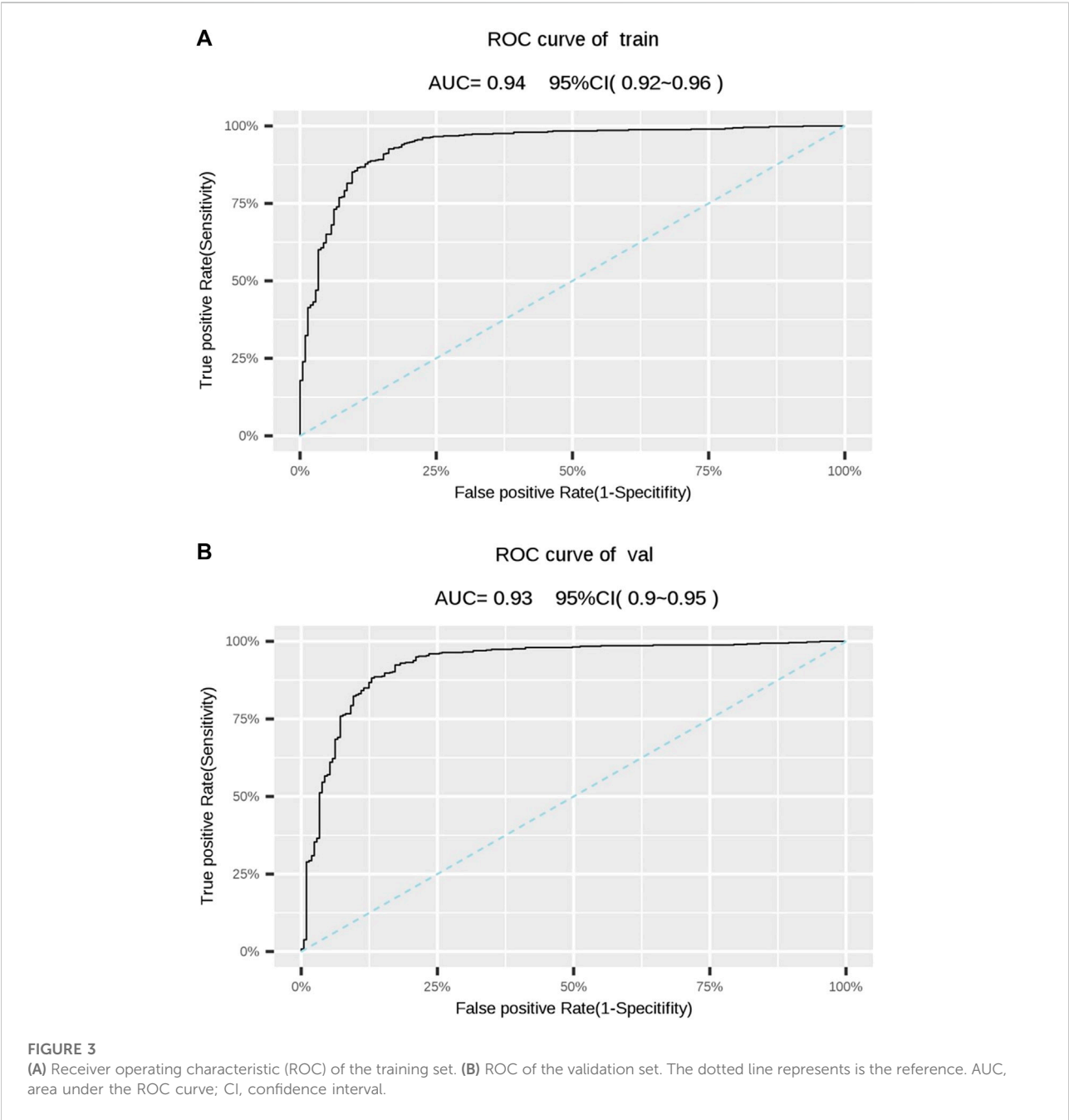


FIGURE 2 (A) Confusion matrix for the training set. (B) Confusion matrix for the validation set. OA, obstructive azoospermia; NOA, non-obstructive azoospermia.

TABLE 4 Internal 5-fold cross-validation results for Model 1.

Set	Accuracy (%)	Sensitivity (%)	Specificity (%)	PPV (%)	NPV (%)	AUC
Training	88.0	89.2	85.2	93.5	76.7	0.938
Validation	88.0	89.4	84.7	93.3	77.0	0.928

PPV, positive predictive value; NPV, negative predictive value; AUC, area under the receiver operating characteristic curve.



Routine hematological parameters are indispensable in clinical disease screening as they reflect the basic physiological and pathological conditions of the individual. In this study, only

the RBC, hemoglobin, and platelets differed significantly between the OA and NOA groups. However, these parameters had an insignificant effect on the diagnostic outcome in the logistic

regression analysis, indicating that differentiation between the two azoospermia types could not be performed accurately based on routine blood tests. However, the construction of a diagnostic model for OA and NOA was urgently needed to distinguish between various azoospermia types.

The parameters included in the model (seminal plasma parameters, hormone levels, and testicular volume) were assessed in studies on azoospermia. Studies demonstrated that the ejaculation volume of azoospermia patients with normal sperm motility was significantly smaller than that of patients with inactive spermatozoa [13]. Furthermore, serum levels of LH, testosterone, FSH, progesterone, estradiol, and other hormones affect spermatogenesis, especially FSH, which plays an important role in Sertoli cells and has an important regulatory effect on sperm formation [14]. A study by Muttukrishna et al. showed that FSH could distinguish OA from NOA, as it is usually normal or slightly elevated in patients with OA and significantly elevated in patients with NOA [15]. The testicular volume can be measured by non-invasive ultrasonographic methods and is closely related to testicular function [16, 17]. Our results were consistent with a previous study that found that patients with NOA had significantly smaller testicles than those in the OA and healthy control groups [18]. Another research showed that patients with severe testicular histopathology had higher serum FSH levels and smaller testicles in a NOA population [19]. The final diagnostic model that included 5 routine clinical parameters was more reliable for differential diagnosis of azoospermia than models based on a single factor (FSH or testicular volume).

Several studies reported diagnostic models to tell OA and NOA apart, using ultrasonography-derived testicular volume alone or in combination with abnormal vas deferens, FSH, or ultrasonography-related parameters. However, these studies assessed relatively few subjects and did not conduct model validation [7, 20–22]. Recent studies focused on omics methods for disease biomarker screening, including studies that screened potential biomarkers of NOA by transcriptome analysis of the testicular tissue [23, 24]; similarly, some researchers used testicular biopsy proteomic analysis to screen possible protein markers and pathways that could distinguish OA from NOA. Ritesh et al. screened seminal plasma mRNA to differentiate OA and NOA [25]. These studies identified potential biomarkers for diagnosing OA and NOA, but these biomarkers should be validated in an in-depth clinical study. Furthermore, although testicular biopsy is the gold standard for azoospermia diagnosis, it is not recommended as a routine clinical diagnostic procedure due to its invasiveness and the possibility of missing the spermatogenic regions [25, 26]. In addition, testicular biopsy may be damaging to the few remaining spermatogenesis sites in NOA patients and should be considered only in cases where no other diagnostic modalities can be used to obtain definitive results. At the same time, it should be carried out in a professional reproductive laboratory, so that all extracted active sperm can be cryopreserved in time. A multicenter study of

the developed diagnostic model is needed before applying it clinically.

In conclusion, this study established and validated a 5-parameter clinical diagnostic model to distinguish OA from NOA using logistic regression analysis. The model included semen volume, semen pH, SPNG, FSH, and testicular volume. This model provides a new method to tell OA and NOA apart and acts as a reference for instituting clinical treatment and other potential clinical applications.

Author contributions

DW and MH provided concept and designed the whole study; XZ and YL performed the experiments; YH and HT contributed to data acquisition and analysis; DW contributed to data interpretation and drafting of the manuscript. All authors contributed to the article and approved the submitted version.

Data availability statement

The original contributions presented in the study are included in the article/supplementary material, further inquiries can be directed to the corresponding authors.

Ethics statement

The studies involving humans were approved by the Ethics Committee of the First Affiliated Hospital of Sun Yat-Sen University. The studies were conducted in accordance with the local legislation and institutional requirements. The participants provided their written informed consent to participate in this study.

Funding

The author(s) declare that no financial support was received for the research, authorship, and/or publication of this article.

Conflict of interest

The authors declare that the research was conducted in the absence of any commercial or financial relationships that could be construed as a potential conflict of interest.

Publisher's note

Please note that the review of this paper was conducted at the previous publisher, SAGE.

References

1. Esteves SC, Miyaoka R, Agarwal A. An update on the clinical assessment of the infertile male. *Clinics (Sao Paulo)* (2011) **66**:691–700. doi:10.1590/s1807-59322011000400026
2. Olesen IA, Andersson AM, Akglaede L, Skakkebaek NE, Rajpert-de Meyts E, Joergensen N, et al. Clinical, genetic, biochemical, and testicular biopsy findings among 1,213 men evaluated for infertility. *Fertil Sterility* (2017) **107**:74–82. doi:10.1016/j.fertnstert.2016.09.015
3. Minhas S, Bettocchi C, Boeri L, Capogrosso P, Carvalho J, Cilesiz NC, et al. European association of urology guidelines on male sexual and reproductive Health: 2021 update on male infertility. *Eur Urol* (2021) **80**:603–20. doi:10.1016/j.eururo.2021.08.014
4. Andrade DL, Viana MC, Esteves SC. Differential diagnosis of azoospermia in men with infertility. *J Clin Med* (2021) **10**. doi:10.3390/jcm10143144
5. Esteves S. Clinical management of infertile men with nonobstructive azoospermia. *Asian J Androl* (2015) **0**. doi:10.4103/1008-682X.148719
6. Hwang K, Smith JF, Coward RM, Penzias A, Bendikson K, Butts S, et al. Evaluation of the azoospermic male: a committee opinion. *Fertil Sterility* (2018) **109**:777–82. doi:10.1016/j.fertnstert.2018.01.043
7. Cai W, Min X, Chen D, Fan C, Feng Z, Li B, et al. Noninvasive differentiation of obstructive azoospermia and nonobstructive azoospermia using multimodel diffusion weighted imaging. *Acad Radiol* (2021) **28**:1375–82. doi:10.1016/j.acra.2020.05.039
8. Esteves SC, Miyaoka R, Agarwal A. Sperm retrieval techniques for assisted reproduction. *Int Braz J Urol* (2011) **37**:570–83. doi:10.1590/s1677-55382011000500002
9. Gordetsky J, van Wijngaarden E, O'Brien J. Redefining abnormal follicle-stimulating hormone in the male infertility population. *BJU Int* (2012) **110**:568–72. doi:10.1111/j.1464-410x.2011.10783.x
10. Xie Y, Yao J, Zhang X, Chen J, Gao Y, Zhang C, et al. A panel of extracellular vesicle long noncoding RNAs in seminal plasma for predicting testicular spermatozoa in nonobstructive azoospermia patients. *Hum Reprod* (2020) **35**:2413–27. doi:10.1093/humrep/deaa184
11. Tradewell MB, Cazzaniga W, Pagani RL, Reddy R, Boeri L, Kresch E, et al. Algorithms for predicting the probability of azoospermia from follicle stimulating hormone: design and multi-institutional external validation. *World J Mens Health* (2022) **40**:600–7. doi:10.5534/wjmh.210138
12. Cissen M, Meijerink AM, D'Hauwers KW, Meissner A, van der Weide N, Mochtar MH, et al. Prediction model for obtaining spermatozoa with testicular sperm extraction in men with non-obstructive azoospermia. *Hum Reprod* (2016) **31**:1934–41. doi:10.1093/humrep/dew147
13. Fedder J. History of cryptorchidism and ejaculate volume as simple predictors for the presence of testicular sperm. *Syst Biol Reprod Med* (2011) **57**:154–61. doi:10.3109/19396368.2010.550796
14. Adamopoulos DA, Koukkou EG. 'Value of FSH and inhibin-B measurements in the diagnosis of azoospermia'—a clinician's overview. *Int J Androl* (2010) **33**:e109–13. doi:10.1111/j.1365-2605.2009.00980.x
15. Muttukrishna S, Yussuff H, Naidu M, Barua J, Arambage K, Suharjono H, et al. Serum anti-Müllerian hormone and inhibin B in disorders of spermatogenesis. *Fertil Sterility* (2007) **88**:516–8. doi:10.1016/j.fertnstert.2006.11.110
16. Sakamoto H, Ogawa Y, Yoshida H. Relationship between testicular volume and testicular function: comparison of the Prader orchidometric and ultrasonographic measurements in patients with infertility. *Asian J Androl* (2008) **10**:319–24. doi:10.1111/j.1745-7262.2008.00340.x
17. Schurich M, Aigner F, Frauscher F, Pallwein L. The role of ultrasound in assessment of male fertility. *Eur J Obstet Gynecol Reprod Biol* (2009) **144**(Suppl. 1):S192–8. doi:10.1016/j.ejogrb.2009.02.034
18. Liu J, Wang Z, Li M, Zhou M, Zhan W. Differential diagnostic value of obstructive and nonobstructive azoospermia by scrotal ultrasound. *Ultrasound Q* (2017) **33**:272–5. doi:10.1097/ruq.0000000000000299
19. Kavoussi PK, Hudson K, Machen GL, Barsky M, Lebovic DI, Kavoussi SK. FSH levels and testicular volumes are associated with the severity of testicular histopathology in men with non-obstructive azoospermia. *J Assist Reprod Genet* (2021) **38**:3015–8. doi:10.1007/s10815-021-02313-y
20. Han BH, Park SB, Seo JT, Chun YK. Usefulness of testicular volume, apparent diffusion coefficient, and normalized apparent diffusion coefficient in the MRI evaluation of infertile men with azoospermia. *Am J Roentgenology* (2018) **210**:543–8. doi:10.2214/ajr.17.18276
21. Huang IS, Huang WJ, Lin AT. Distinguishing non-obstructive azoospermia from obstructive azoospermia in Taiwanese patients by hormone profile and testis size. *J Chin Med Assoc* (2018) **81**:531–5. doi:10.1016/j.jcma.2017.09.009
22. Du J, Li F, Guo Y, Yang L, Zheng J, Chen B, et al. Differential diagnosis of azoospermia and etiologic classification of obstructive azoospermia: role of scrotal and transrectal US. *Radiology* (2010) **256**:493–503. doi:10.1148/radiol.10091578
23. Zhou R, Lv X, Chen T, Chen Q, Tian H, Yang C, et al. Construction and external validation of a 5-gene random forest model to diagnose non-obstructive azoospermia based on the single-cell RNA sequencing of testicular tissue. *Aging* (2021) **13**:24219–35. doi:10.18632/aging.203675
24. Zhou R, Liang J, Chen Q, Tian H, Yang C, Liu C. A 3-gene random forest model to diagnose non-obstructive azoospermia based on transcription factor-related genes. *Reprod Sci* (2022) **30**:233–46. doi:10.1007/s43032-022-01008-8
25. Goel R, Batra H, Kumar M, Dada R, Kumar R. Evaluation of cell-free seminal mRNA for the diagnosis of obstruction as the cause of azoospermia in infertile men: a prospective cohort study. *Andrologia* (2022) **54**:e14364. doi:10.1111/and.14364
26. Schoor R, Elhanbly S, Niederberger C, Ross L. The role of testicular biopsy in the modern management of male infertility. *J Urol* (2002) **167**:197–200. doi:10.1097/00005392-200201000-00044



OPEN ACCESS

*CORRESPONDENCE

Chantacha Sitticharoon,
✉ chantacha.sit@mahidol.ac.th

RECEIVED 27 March 2024

ACCEPTED 08 April 2024

PUBLISHED 25 April 2024


CITATION

Chatree S, Sitticharoon C, Maikaew P, Pongwattanapakin K, Keadkraichaiwat I, Churintaraphan M, Sripong C, Sriwichitchai R and Tapechum S (2024), Corrigendum: Epigallocatechin gallate decreases plasma triglyceride, blood pressure, and serum kisspeptin in obese human subjects. *Exp. Biol. Med.* 249:10179. doi: 10.3389/ebm.2024.10179

COPYRIGHT

© 2024 Chatree, Sitticharoon, Maikaew, Pongwattanapakin, Keadkraichaiwat, Churintaraphan, Sripong, Sriwichitchai and Tapechum. This is an open-access article distributed under the terms of the [Creative Commons Attribution License \(CC BY\)](https://creativecommons.org/licenses/by/4.0/). The use, distribution or reproduction in other forums is permitted, provided the original author(s) and the copyright owner(s) are credited and that the original publication in this journal is cited, in accordance with accepted academic practice. No use, distribution or reproduction is permitted which does not comply with these terms.

Corrigendum: Epigallocatechin gallate decreases plasma triglyceride, blood pressure, and serum kisspeptin in obese human subjects

Saimai Chatree, Chantacha Sitticharoon *, Pailin Maikaew, Kitchaya Pongwattanapakin, Issarawan Keadkraichaiwat, Malika Churintaraphan, Chanakarn Sripong, Rungnapa Sriwichitchai and Sompol Tapechum

Department of Physiology, Faculty of Medicine, Siriraj Hospital, Mahidol University, Bangkok, Thailand

KEYWORDS

obesity, blood pressure, epigallocatechin gallate, human adipocytes, kisspeptin, plasma triglyceride

A Corrigendum on

[Epigallocatechin gallate decreases plasma triglyceride, blood pressure, and serum kisspeptin in obese human subjects](#)

by Chatree S, Sitticharoon C, Maikaew P, Pongwattanapakin K, Keadkraichaiwat I, Churintaraphan M, Sripong C, Sriwichitchai R and Tapechum S (2021). *Exp. Biol. Med.* 246(2): 163–176. doi: [10.1177/1535370220962708](https://doi.org/10.1177/1535370220962708)

In the published article, there is an error in the Certificate of Ethical Approval Number in the **Ethics Statement**. The published certificate of approval number was mistakenly stated as “si344/2558(EC2).” The correct number for the Certificate of Ethical Approval Number is “Si 563/2015”.

The authors apologize for this error and state that this does not change the scientific conclusions of the article in any way.



OPEN ACCESS

*CORRESPONDENCE

Jian Liao,
✉ liaojian@gmc.edu.cn
Yue Xiong,
✉ 510429863@qq.com

†These authors have contributed equally to this work

RECEIVED 08 April 2024

ACCEPTED 19 April 2024

PUBLISHED 17 May 2024



CITATION

Xiong Y, Huang C-W, Shi C, Peng L, Cheng Y-T, Hong W and Liao J (2024), Corrigendum: Quercetin suppresses ovariectomy-induced osteoporosis in rat mandibles by regulating autophagy and the NLRP3 pathway. *Exp. Biol. Med.* 249:10149. doi: 10.3389/ebm.2024.10149

COPYRIGHT

© 2024 Xiong, Huang, Shi, Peng, Cheng, Hong and Liao. This is an open-access article distributed under the terms of the [Creative Commons Attribution License \(CC BY\)](https://creativecommons.org/licenses/by/4.0/). The use, distribution or reproduction in other forums is permitted, provided the original author(s) and the copyright owner(s) are credited and that the original publication in this journal is cited, in accordance with accepted academic practice. No use, distribution or reproduction is permitted which does not comply with these terms.

Corrigendum: Quercetin suppresses ovariectomy-induced osteoporosis in rat mandibles by regulating autophagy and the NLRP3 pathway

Yue Xiong ^{1*†}, Cheng-Wei Huang^{2†}, Chao Shi³, Liang Peng³, Yu-Ting Cheng¹, Wei Hong³ and Jian Liao ^{1*}

¹Department of Prosthodontics and Implantology, School/Hospital of Stomatology, Guizhou Medical University, Guiyang, China, ²AOSI CAR Dental, Shantou, China, ³Guizhou Medical University, Guiyang, China

KEYWORDS

NLRP3, Quercetin, alendronate, autophagy, osteoclasts, postmenopausal osteoporosis

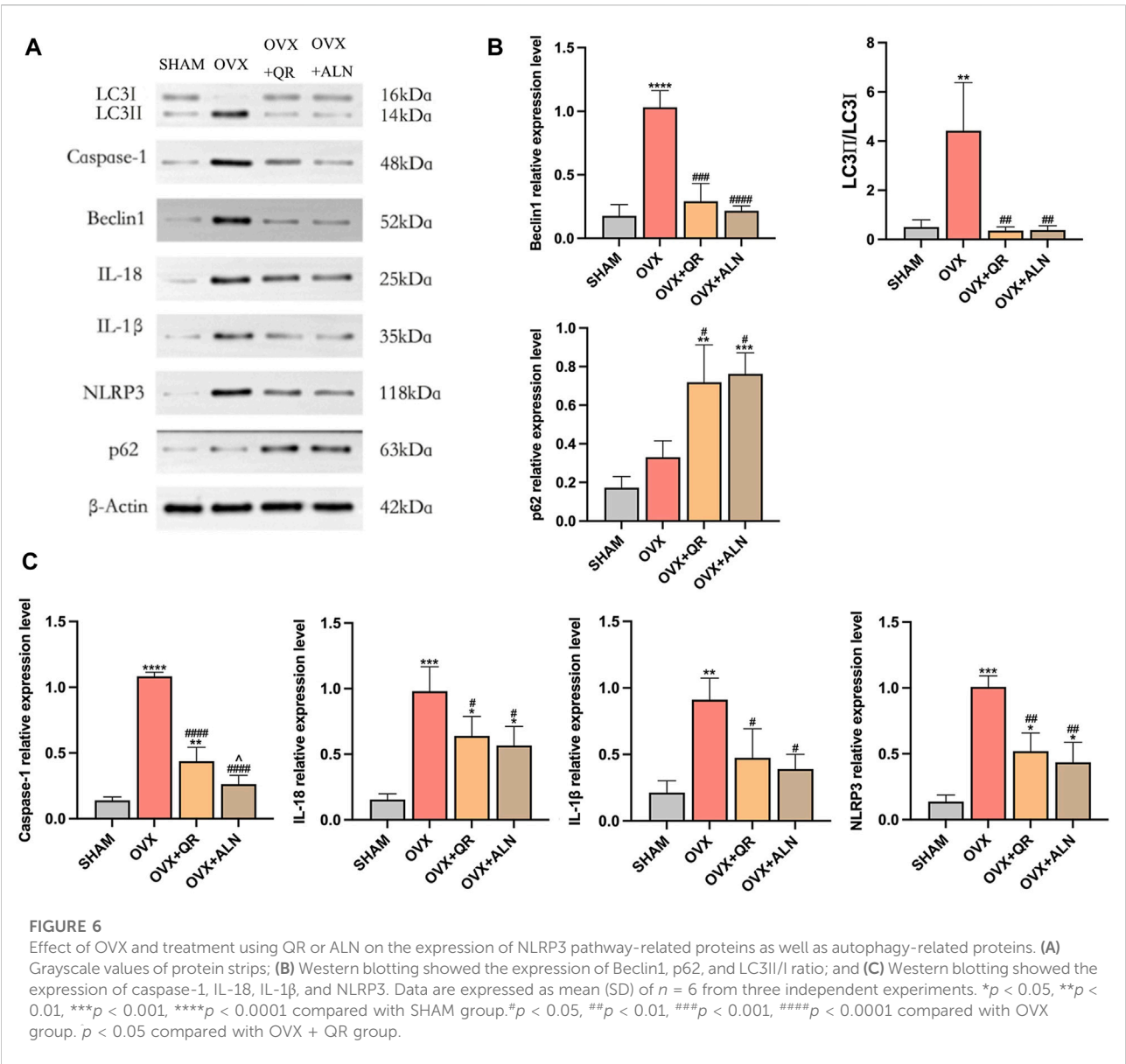
A Corrigendum on

[Quercetin suppresses ovariectomy-induced osteoporosis in rat mandibles by regulating autophagy and the NLRP3 pathway](#)

by Xiong Y, Huang C-W, Shi C, Peng L, Cheng Y-T, Hong W and Liao J (2023). *Exp. Biol. Med.* 248(23):2363–2380. doi: [10.1177/15353702231211977](https://doi.org/10.1177/15353702231211977)

In the published article, there was a mistake in [Figure 6](#) and [Figure 7](#) as published. In the original published version, the authors incorrectly reversed the labeling of the positions of LC3I and LC3II when labeling the names of the proteins. The corrected [Figure 6](#) and [Figure 7](#) appears below.

The authors apologize for this error and state that this does not change the scientific conclusions of the article in any way.



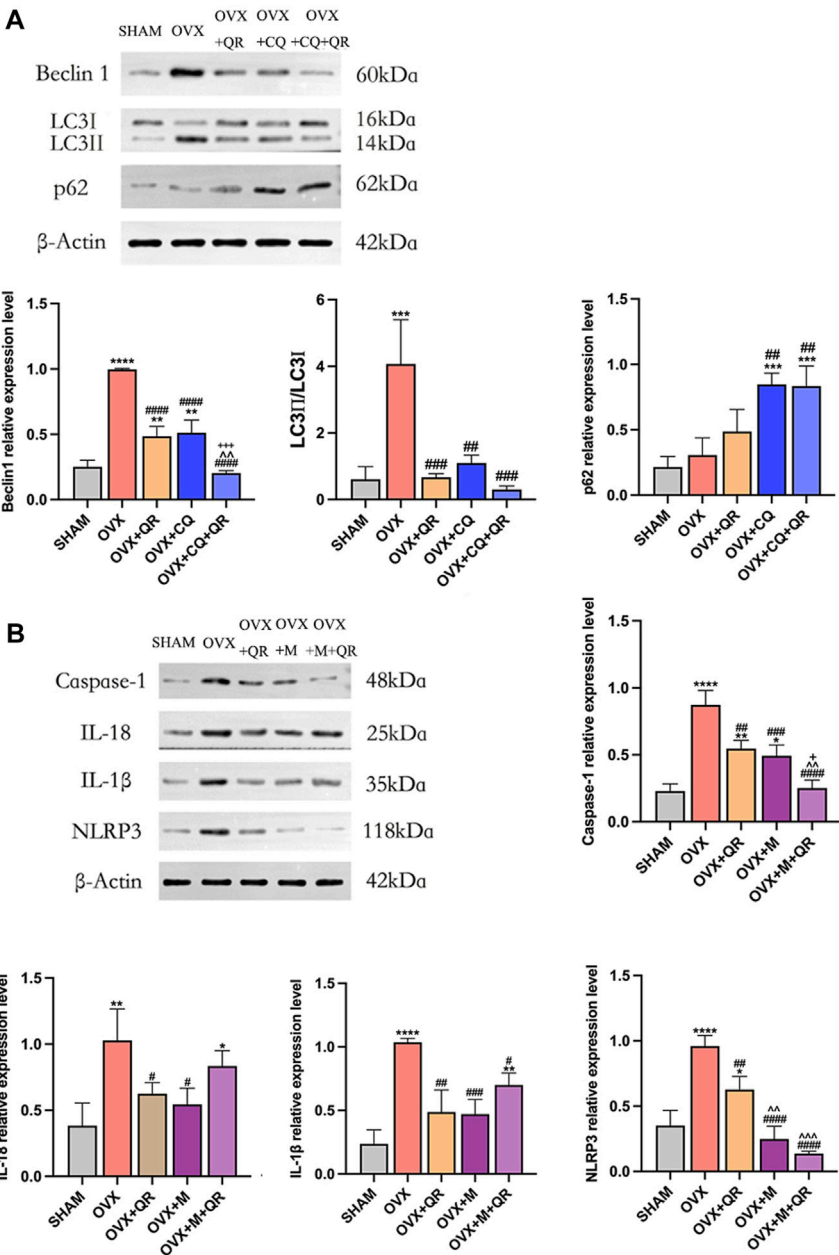


FIGURE 7
(A) Western blotting showed the effect of QR and CQ on the expression of autophagy-related proteins and (B) Western blotting showed the effect of QR and MCC950 on the expression of NLRP3 pathway-related proteins. Data are expressed as mean (SD) of $n = 6$ from three independent experiments. $*p < 0.05$, $**p < 0.01$, $***p < 0.001$, $****p < 0.0001$ compared with SHAM group. $^{\#}p < 0.05$, $^{\#\#}p < 0.01$, $^{\#\#\#}p < 0.001$, $^{\#\#\#\#}p < 0.0001$ compared with OVX group. $\bar{p} < 0.01$, $\bar{p} < 0.001$ compared with OVX + QR group. $*p < 0.05$, $^{++}p < 0.001$ compared with OVX + CQ group or OVX + M group.



OPEN ACCESS

*CORRESPONDENCE

Yuping Wang,
✉ 1500776978@qq.com

RECEIVED 20 July 2023

ACCEPTED 11 December 2023

PUBLISHED 22 April 2024

CITATION

Ma R, Xie N, Shu Y, Wu Y, He P, Xiang Y, Zhou Y and Wang Y (2024), Cannabidiol alleviates carbon tetrachloride-induced liver fibrosis in mice by regulating NF- κ B and PPAR- α pathways. *Exp. Biol. Med.* 249:10141. doi: 10.3389/ebm.2024.10141

COPYRIGHT

© 2024 Ma, Xie, Shu, Wu, He, Xiang, Zhou and Wang. This is an open-access article distributed under the terms of the [Creative Commons Attribution License \(CC BY\)](https://creativecommons.org/licenses/by/4.0/). The use, distribution or reproduction in other forums is permitted, provided the original author(s) and the copyright owner(s) are credited and that the original publication in this journal is cited, in accordance with accepted academic practice. No use, distribution or reproduction is permitted which does not comply with these terms.

Cannabidiol alleviates carbon tetrachloride-induced liver fibrosis in mice by regulating NF- κ B and PPAR- α pathways

Run Ma^{1,2,3}, Na Xie², Yuanhui Shu², Yafeng Wu⁴, Ping He^{1,2}, Yining Xiang⁵, Yan Zhou^{1,2} and Yuping Wang^{1,2*}

¹Center for Clinical Laboratories, The Affiliated Hospital of Guizhou Medical University, Guiyang, Guizhou, China, ²School of Clinical Laboratory Science, Guizhou Medical University, Guiyang, Guizhou, China, ³Sichuan Provincial Center for Disease Control and Prevention, Chengdu, Sichuan, China, ⁴Clinical Laboratory, The Fourth People's Hospital of Ya'an City, Ya'an, Sichuan, China, ⁵Pathology, The Affiliated Hospital of Guizhou Medical University, Guiyang, Guizhou, China

Abstract

Liver fibrosis has become a serious public health problem that can develop into liver cirrhosis and hepatocellular carcinoma and even lead to death. Cannabidiol (CBD), which is an abundant nonpsychoactive component in the cannabis plant, exerts cytoprotective effects in many diseases and under pathological conditions. In our previous studies, CBD significantly attenuated liver injury induced by chronic and binge alcohol in a mouse model and oxidative bursts in human neutrophils. However, the effects of CBD on liver fibrosis and the underlying mechanisms still need to be further explored. A mouse liver fibrosis model was induced by carbon tetrachloride (CCl₄) for 10 weeks and used to explore the protective properties of CBD and related molecular mechanisms. After the injection protocol, serum samples and livers were used for molecular biology, biochemical and pathological analyses. The results showed that CBD could effectively improve liver function and reduce liver damage and liver fibrosis progression in mice; the expression levels of transaminase and fibrotic markers were reduced, and histopathological characteristics were improved. Moreover, CBD inhibited the levels of inflammatory cytokines and reduced the protein expression levels of p-NF- κ B, NF- κ B, p-I κ B α , p-p38 MAPK, and COX-2 but increased the expression level of PPAR- α . We found that CBD-mediated protection involves inhibiting NF- κ B and activating PPAR- α . In conclusion, these results suggest that the hepatoprotective effects of CBD may be due to suppressing the inflammatory response in CCl₄-induced mice and that the NF- κ B and PPAR- α signaling pathways might be involved in this process.

KEYWORDS

cannabidiol, liver fibrosis, carbon tetrachloride, NF- κ B, PPAR- α

Impact statement

In this study, CBD had a hepatoprotective effect on CCl₄-induced liver fibrosis in mice by increasing antioxidant effects, and its mechanism of action may be related to the regulation of the NF- κ B and PPAR- α signaling pathways. Therefore, CBD and related compounds could represent novel pharmacological agents to treat fibrosis.

Introduction

Liver fibrosis is mainly caused by the progression of various chronic liver diseases. Worldwide, chronic liver diseases mainly include alcoholic hepatitis, nonalcoholic steatohepatitis (NASH), nonalcoholic fatty liver disease (NAFLD), viral hepatitis [hepatitis B (HBV) and hepatitis C (HCV)] and cholestatic liver disease [1–3]. In liver fibrosis, the most important pathological change in the liver is the formation and deposition of extracellular matrix (ECM) [4, 5]. The amount of type I collagen (COL-I) deposition positively correlates with the severity of fibrosis [6, 7]. The activation of hepatic stellate cells (HSCs), which express alpha-smooth muscle actin (α -SMA) and secrete and synthesize ECM and various autocrine or paracrine cytokines, such as tumor necrosis factor- α (TNF- α), interleukin 1 β (IL-1 β) and interleukin 6 (IL-6), is a crucial link in the occurrence of liver fibrosis. Many intracellular signaling pathways, including the transforming growth factor- β 1 (TGF- β 1) [8–10] and nuclear factor kappa B (NF- κ B) [11, 12] pathways, are involved in HSC activation.

Hepatic injury involves stress signaling [e.g., mitogen-activated protein kinase p38 (p38MAPK) and c-Jun N-terminal kinase (JNK)] [13] and proinflammatory pathways [e.g., NF- κ B [14, 15] and cyclooxygenase-2 (COX2)] [16] in various cell types, which in turn modulate important inflammatory and cell death processes. NF- κ B is a key regulator that stimulates the expression of inflammatory factors, chemokines and adhesion molecules and plays an important role in cell growth, differentiation and apoptosis. COX-2 is an important enzyme in the synthesis of prostaglandins from arachidonic acid and plays a key role in the inflammatory response [17]. The interaction of peroxidase proliferator-activated receptor- α (PPAR- α) with other signaling pathways can also regulate cellular redox status. For example, PPAR- α activation can inhibit the transcription of NF- κ B and oxidative stress and reduce the release of inflammatory cytokines [18].

Cannabidiol (CBD) is the main nonpsychoactive component of the cannabis plant and has many beneficial pharmacological effects, such as anti-inflammatory and antioxidant effects [19–21]. Studies have shown that CBD can be used for alcohol use disorder (AUD) and alcohol-related damage to the brain and liver [22]; CBD can be used to treat conditions such as

colitis, arthritis and type 1 diabetes, alcohol-induced lipodystrophy, or hypoxia-ischemia-induced brain damage [23, 24]; and CBD greatly alleviates liver inflammation, oxidative/nitrative stress, and cell death and inhibits bacterial endotoxin-induced NF- κ B activation and TNF- α production in Kupffer cells [25]. Currently, there are limited treatment options for liver fibrosis, and it is of great clinical importance to identify drugs that can prevent fibrosis progression or even reverse it. This study examined the protective effect of CBD in CCl₄-induced mice with liver fibrosis, which involved the NF- κ B and PPAR- α signaling pathways, and revealed its potential mechanism of action.

Materials and methods

Experimental reagents and equipments

The following reagents were used: CBD (Sigma, United States); colchicine (Beyotime, China); CCl₄ (Aladdin, China); peanut oil (Yuanye, China); ELISA kits (Novus, United States); hematoxylin and eosin (HE) and Masson assay kits (Beyotime, China); aspartate aminotransferase (AST) and hyaluronic acid (HA) kits (Nanjing Jiancheng Bioengineering Institute, China); RIPA lysis buffer and a BCA kit (Solaibao, China); COX-2, p-IkBa, and IkBa antibodies (Wanleibio, China); p-NF- κ B, NF- κ B, p-p38 MAPK, and p-38 MAPK antibodies (CST, United States); TGF- β 1, α -SMA, COL-I, PPAR- α and GAPDH antibodies (Abcam, United States); horseradish peroxidase-labeled secondary antibodies (Bioprimacy, China); chemiluminescence (ECL) color developing solution (Merck, United States); an RNeasy mini kit (Axygen, United States); a PrimeScript RT reagent kit with gDNA Eraser and SYBR Green Master Mix (Takara, Japan); an automatic chemical analyzer (Hitachi, Japan); and light microscopy (Nikon, Japan).

Experimental animals and treatments

Forty mice (C57BL/6J) were purchased from Guizhou Medical University. All animal experiments were approved by the Guizhou Medical University Animal Care Welfare Committee. Male (6–8 weeks old) mice weighing approximately 20 g were adapted to the animal environment, and food and water were available randomly. One week later, the mice were randomly divided into five groups with the following injection for 10 weeks: (I) In the control group, normal mice were treated with a peanut oil solution twice weekly ($n = 8$). (II) In the CCl₄ group, mice were intraperitoneally administered a 30% CCl₄ peanut solution (5 mL/kg) twice weekly ($n = 8$). (III) In the 4 mg/kg CBD group, mice were administered 4 mg/kg CBD intraperitoneally and the same CCl₄ as the CCl₄ group ($n = 8$). (IV) In the 8 mg/kg CBD group, mice were administered 8 mg/kg CBD intraperitoneally and the same CCl₄ as the CCl₄

group ($n = 8$). (V) In the colchicine group, mice were administered 0.2 mg/kg colchicine intraperitoneally and the same CCl_4 peanut solution as the CCl_4 group ($n = 8$). Two hours before each intraperitoneal injection of CCl_4 , the mice in the CBD and colchicine groups were intraperitoneally injected with the appropriate drug at the indicated dose (4, 8 mg/kg CBD, 0.2 mg/kg colchicine), and mice in the control group and model group were injected with normal saline. All mice were euthanized by anesthesia 24 h after the last administration, and blood and liver tissues were collected for further examination. The left lobe of the liver was quickly fixed in 4% paraformaldehyde, and the remaining liver samples were collected, frozen in liquid nitrogen and stored at -80°C .

Serum biochemical analysis

Serum was obtained by centrifuging ($3,000 \times g$, 4°C , for 10 min) whole blood. AST and HA levels were determined using a clinical chemical analyzer.

ELISA analysis of inflammatory cytokines

Liver tissues were promptly removed and washed in precooled normal saline. Liver tissues (0.1 g) were completely homogenized with cold saline (0.9 mL) by sonication on ice to obtain 10% tissue homogenate, and the supernatant was obtained by centrifugation. The Coomassie brilliant blue method was used to measure the total protein content, and the level of IL-1 β was measured using the corresponding assay kit. Serum levels of IL-6 and TNF- α were measured by Valukine ELISA kits according to the manufacturer's instructions.

Examination of pathological changes

Fresh liver samples were fixed in 4% paraformaldehyde for 24 h and paraffin-embedded tissue sections (4 μm). The extent of inflammation and cell necrosis in the liver was observed using HE staining. Liver fibrosis was effectively and widely evaluated at the histological level by staining collagen fibers with Masson's trichrome staining. The histological degree of liver fibrosis was observed using light microscopy by a pathologist who was blinded to this test.

Immunohistochemical staining

The sections were dewaxed, hydrated, boiled in citrate buffer for 5 minutes, cooled to room temperature, and washed three times in PBS buffer. Next, sections were incubated in 3% H_2O_2 for 10 min to block endogenous

peroxidase activity and were blocked with 10% bovine serum in a water bath at 37°C for 30 min to block nonspecific binding. Immunohistochemistry was performed by incubating the sections overnight at 4°C with primary antibodies (1/1000) (α -SMA and COL- I) and rinsing the sections three times with PBS. Biotinylated secondary antibodies were added according to the kit instructions. The sections were incubated with the DAB reagent for 3 min to develop the color, and the sections were counterstained with Mayer's hematoxylin. Finally, the sections were dehydrated in ethanol, cleared in xylene and sealed with neutral gum. Specific primary antibodies were substituted with PBS or nonimmune isotype-matched sera as the negative control. Images were captured by light microscopy, five fields were randomly selected, and the percentage of the area was assessed by ImageJ.

Western blotting

The liver tissue was washed with precooled saline and then dried with filter paper. Protein samples were obtained from liver tissues in RIPA lysis solution with sonication on ice, and then the protein concentration was determined by the BCA method. A total of 30 μg of protein was used for western blot analysis. Protein samples were separated by 10% SDS-PAGE and then transferred to PVDF membranes. The PVDF membranes were incubated with the appropriate primary antibodies (TGF- β 1 1/1000, α -SMA 1/10,000, COL-I 1/1000, p-NF- κ B 1/500, NF- κ B 1/1000, p-p38 MAPK 1/1000, p38 MAPK 1/1000, p-I κ B α 1/500, I κ B α 1/500, COX-2 1/1000, PPAR- α 1/500, and GAPDH 1/10,000) at 4°C overnight and then with the corresponding horseradish peroxidase-conjugated secondary antibodies. Next, the chromogenic solution was added dropwise, and the corresponding protein bands were detected after exposure. ImageJ software was used to measure the gray values of the bands.

Quantitative real-time polymerase chain reaction (PCR)

Liver tissues (0.1 g) were homogenized, and mRNA was isolated using the RNeasy mini kit following the manufacturer's instructions. Reverse transcription was performed using the PrimeScript RT reagent kit with gDNA Eraser and SYBR Green Master Mix. Real-time PCR was performed for each sample using a Roche Real-Time PCR System. Transcription specificity was confirmed by melting curve profiles generated at the end of the PCR program. The data are expressed as the expression of the target genes normalized to the expression of GAPDH and were quantified using the comparative cycle threshold Ct method ($2^{-\Delta\Delta\text{CT}}$) (Table 1).

TABLE 1 Primer sequences for quantitative real-time polymerase chain reaction.

Gene	Forward primer (5'-3')	Reverse primer (5'-3')
GAPDH	AAGAAGGTGGTGAAGCAGGCATC	CGGCATCGAAGGTGGAAGAGTG
COL-I	ACGCCATCAAGGTCTACTGC	ACTCGAACGGGAATCCATCG
α -SMA	GCCATCTTTCATTGGGATGGA	CCCCTGACAGGACGTTGTTA
TGF- β	GCTGAACCAAGGAGACGGAA	ATGTCATGGATGGTGCCAG
IL-1 β	CTTCAGGCAGGCAGTATC	CAGCAGGTTATCATCATCATC
IL-6	CCCCAATTTCCAATGCTCTCC	CGCACTAGGTTTGCCGAGTA
TNF- α	TCAGTTCCATGGCCCAGAC	GTTGTCTTTGAGATCCATGCCATT

Statistical analysis

Values are expressed as the mean \pm standard deviation. The statistical significance of differences was determined using Student's *t*-test (for two groups) or one-way ANOVA (for more than two groups) followed by the LSD multiple comparisons test. All analyses were performed with PASW statistics 26 (SPSS). *p* < 0.05 was considered significant.

Results

CBD treatment ameliorated liver damage

The levels of AST and HA are considered important markers for evaluating liver function. We found that CCl₄ significantly increased the levels of AST and HA compared to those in the control group; the administration of CCl₄ to mice treated with CBD and colchicine markedly reduced the levels of AST and HA. However, no significantly different expression levels of AST and HA were found after 4 mg/kg and 8 mg/kg CBD injection (Figures 1A, B). Liver injury was assessed by HE staining. In the liver tissue of the control group, liver cells were neatly arranged and showed no necrosis, indicating normal liver tissue structure. In the CCl₄ group, hepatocyte disorder, necrosis, swelling, and a large amount of inflammatory cell infiltration indicated serious liver damage. Compared with the CCl₄ group, the CBD and colchicine groups had significantly reduced liver damage, with only mild necrosis and a relatively stable cell structure (Figure 1C). Masson staining showed that the liver tissue of the control group exhibited a normal lobular structure, the radial hepatic cords were neatly arranged, and there was no collagen accumulation around the blood vessels; the structure of the liver lobules in the CCl₄ group was severely damaged, a large amount of collagen was deposited, and pseudo lobules had formed, indicating that the model of liver fibrosis was successfully established; and in the CBD and colchicine groups, the liver was not significantly damaged, the accumulation of

collagen was reduced, and the degree of fibrosis was significantly improved compared with that in the CCl₄ group. The histological changes observed in both fibrosis models were significantly attenuated by CBD (Figure 1D). The extent of the improvement did not increase with the CBD dose. Combined with the serological results, these data showed that CBD had hepatoprotective effects on CCl₄-induced mice.

CBD treatment attenuated CCl₄-induced liver fibrosis

In the liver tissue of the control group, α -SMA and COL-I were weakly expressed in the portal area and central vasculature wall; in the CCl₄ group, α -SMA, and COL-I were widely expressed, mainly distributed in the portal ducts of fibrous tissue proliferation and the interarea interval, and diffuse expression was also observed between the central vein and hepatocytes; and the sites of α -SMA and COL-I expression in the CBD group and colchicine groups were the same as those in the CCl₄ group, but the areas were markedly reduced (Figures 2A, B). Positive area expression analysis also showed similar decreases in α -SMA and COL-I after CBD administration. However, no significant differences in the expression of α -SMA and COL-I were found between 4 mg/kg and 8 mg/kg CBD (Figures 2C, D).

CBD treatment alleviated the production of inflammatory mediators

Inflammatory cytokines play a pivotal role in liver fibrosis. The levels of the inflammatory markers IL-6, IL-1 β , and TNF- α in the different treatment groups were measured by ELISA. CCl₄ treatment markedly elevated the levels of serum IL-6 and TNF- α and liver IL-1 β compared with those in the control group. Treatment with CBD significantly reversed the increases in the expression of IL-6, IL-1 β , and TNF- α , and the same results were obtained after colchicine treatment

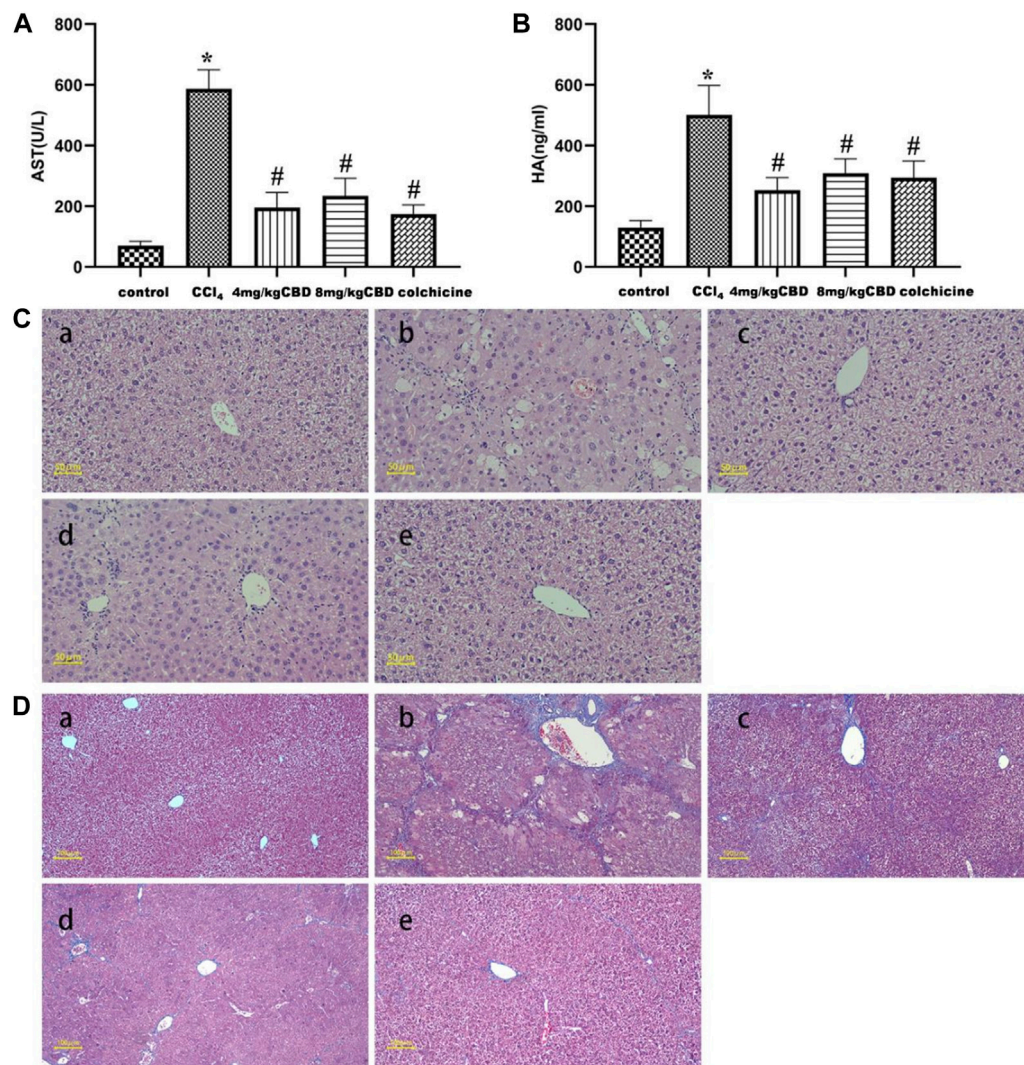


FIGURE 1

Effects of CBD treatment on liver function in mice with CCl₄-induced liver fibrosis. (A,B) Serum AST and HA levels in the indicated groups. (C) Representative HE staining of liver sections. (D) Fibrosis deposition was observed by Masson trichrome staining. The values represent the means \pm SEM ($n = 8$). * $p < 0.05$ vs. the control group, # $p < 0.05$ vs. the CCl₄ group, as determined by one-way ANOVA, followed by the LSD multiple comparisons test. (a) Control group; (b) CCl₄ group; (c) 4 mg/kg CBD group; (d) 8 mg/kg CBD group; (e) 0.2 mg/kg colchicine group.

(Figures 3A–C). Semiquantitative q-PCR analysis also showed similar decreases in IL-6, IL-1 β , and TNF- α mRNA expression after CBD administration. The levels of the inflammatory markers IL-6, IL-1 β , and TNF- α were not significantly different between 4 mg/kg and 8 mg/kg CBD (Figure 3D).

CBD treatment attenuated the expression levels of TGF- β 1, α -SMA, and COL-I

In response to CCl₄, the expression levels of TGF- β 1, α -SMA, and COL-I in the liver in the CCl₄ group increased significantly,

and these expression levels were effectively reduced by CBD and colchicine (Figures 4A–D). The semiquantitative q-PCR results showed increased expression of TGF- β 1, α -SMA and COL-I in liver tissues in the CCl₄ group compared with the control group; compared with that in the CCl₄ group, the expression of TGF- β 1, α -SMA and COL-I markedly decreased after treatment with CBD and colchicine (Figure 4E). The western blot and Semiquantitative q-PCR results showed that the expression levels of TGF- β 1, α -SMA, and COL-I were similar between 4 mg/kg and 8 mg/kg CBD. Importantly, the results showed that CBD treatment attenuated CCl₄-induced liver fibrosis.

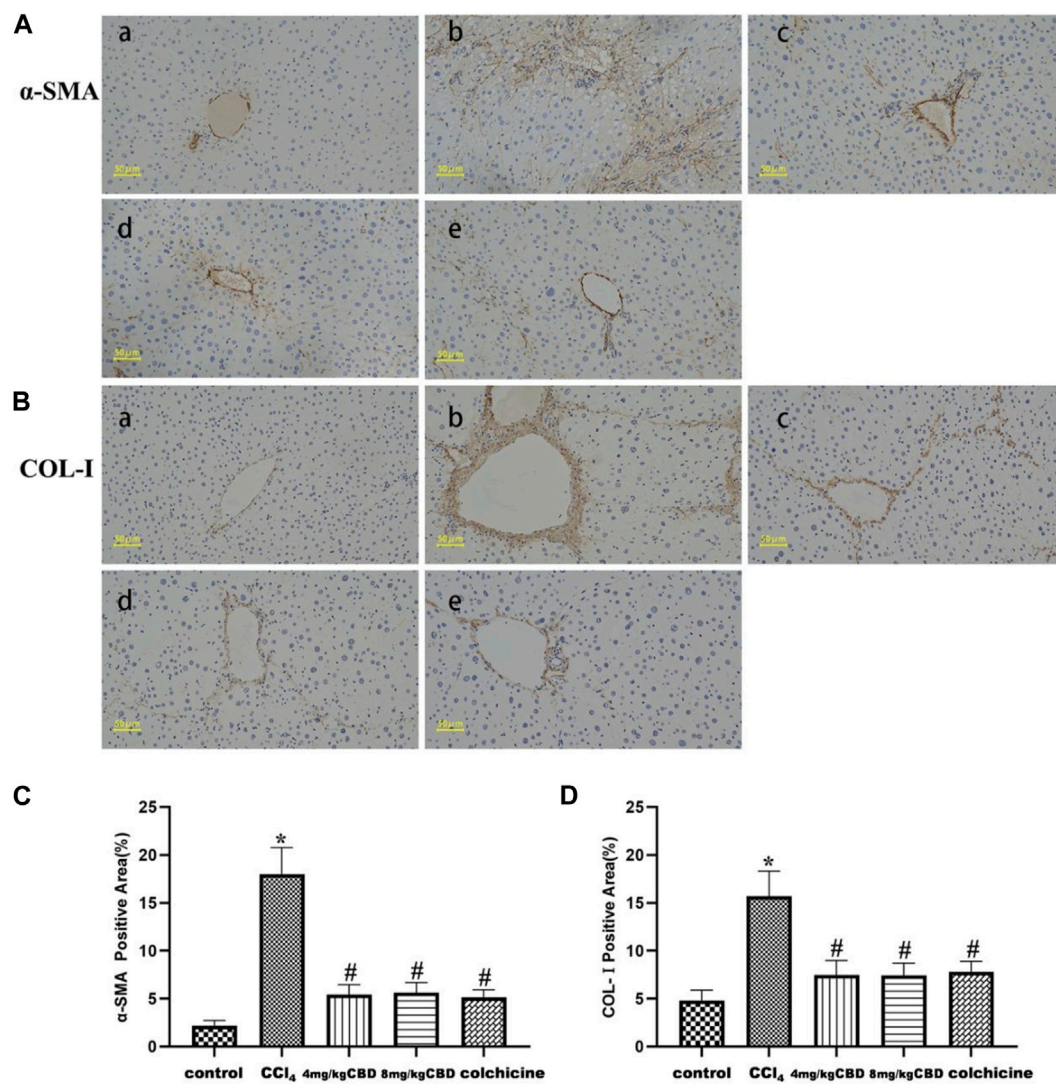


FIGURE 2

Effects of CBD on α -SMA and COL-I in mice with CCl₄-induced liver fibrosis. (A,B) Representative immunohistochemical staining of α -SMA and COL-I. (C,D) Quantification of positive staining areas was performed by ImageJ software. The values represent the means \pm SEM ($n = 8$). * $p < 0.05$ vs. the control group, # $p < 0.05$ vs. the CCl₄ group, as determined by one-way ANOVA, followed by the LSD multiple comparisons test. (a) Control group; (b) CCl₄ group; (c) 4 mg/kg CBD group; (d) 8 mg/kg CBD group; (e) 0.2 mg/kg colchicine group.

CBD treatment protected the liver by inhibiting the NF- κ B pathway and activating the PPAR- α pathway

To explore the potential mechanism of CBD mediated protection, we measured the expression of NF- κ B and PPAR- α related proteins in liver tissues by western blotting. Compared with those in the control group, the expression levels of p-NF- κ B, NF- κ B, and COX-2 and the p-I κ Ba/I κ Ba and p-p38/p38 ratios in the CCl₄ group were significantly increased. Interestingly, CBD and colchicine treatment reversed these alterations in liver fibrosis, suggesting that the effect of CBD on CCl₄-induced inflammation was associated with inhibiting the activation of

the NF- κ B pathway. In addition, PPAR- α was highly expressed in the control group, and the expression of PPAR- α in the liver was significantly decreased in the CCl₄ group compared with the control group. CBD and colchicine treatment significantly increased the expression of PPAR- α in the liver, indicating that CBD may modulate PPAR- α signaling in mice with CCl₄-induced liver fibrosis (Figures 5A–H).

Discussion

Liver fibrosis is the pathological result of abnormal ECM accumulation in the liver and is closely related to hepatic

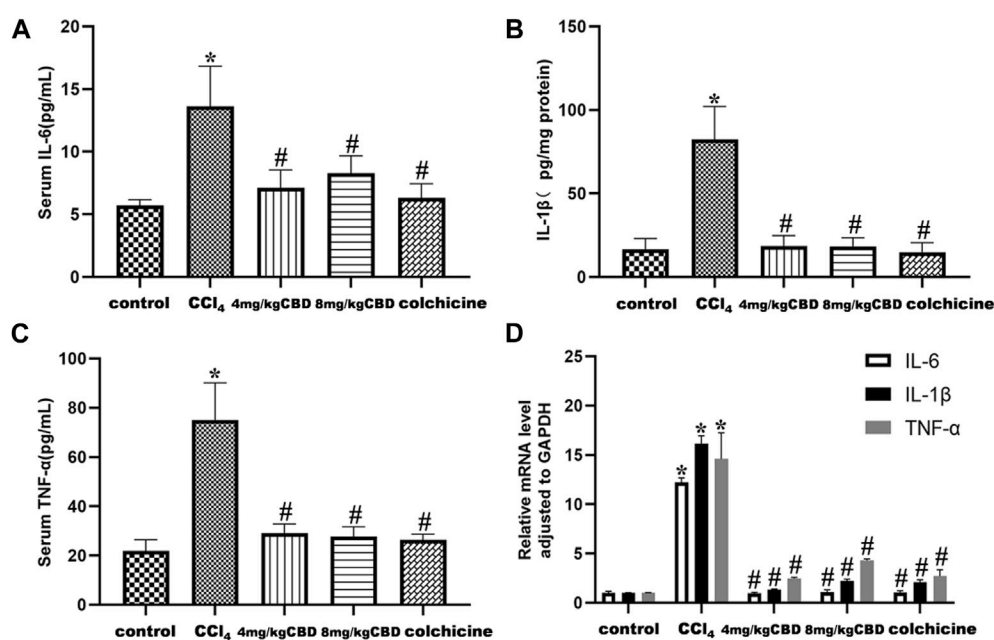


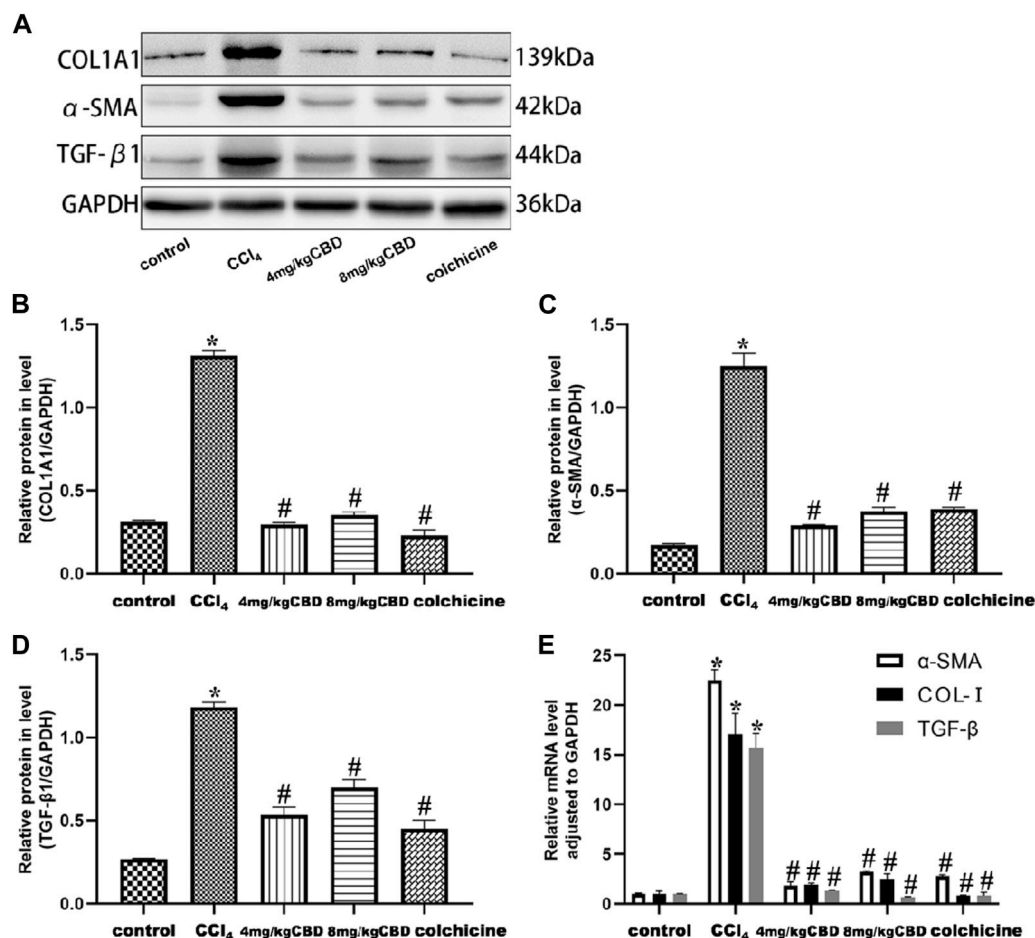
FIGURE 3

Effects of CBD on inflammatory cytokines in mice with CCl₄-induced liver fibrosis. (A–C) Serum levels of IL-6 and TNF-α and liver levels of IL-1β. (D) The mRNA levels of IL-6, IL-1β and TNF-α were measured by q-PCR. The values represent the means ± SEM (*n* = 8). **p* < 0.05 vs. the control group, #*p* < 0.05 vs. the CCl₄ group, as determined by one-way ANOVA, followed by the LSD multiple comparisons test.

morbidity and mortality [26]. Some studies have shown that the development of liver fibrosis can be prevented by experimental clinical treatments, but many patients do not have good reactions [27]. Therefore, there is an urgent need for new therapeutic approaches to reverse fibrosis. CBD is one of the main components extracted from cannabis, and its level is second only to that of tetrahydrocannabinol (THC) [19]. In recent years, the medicinal value of CBD has become increasingly apparent, and long-term use has shown good tolerance and no side effects in humans [28, 29]. CBD can regulate the immune system in different tissues and reduce oxidative/nitrative stress [30], cell death and inflammatory responses, such as IL-6, COX2, and NF-κB, neutrophil infiltration, and stress signaling [31–33]. Researchers have found that CBD has some important effects on the central nervous system, including antipsychotic, antianxiety, antiepileptic, and analgesic effects [34]. In addition, CBD also has complex immune regulation, anti-inflammatory and antioxidant effects [35]. Studies have reported that CBD can induce apoptosis of thymus cells and spleen cells, inhibit the proliferation of T cells and macrophages, and have certain therapeutic effects on autoimmune diseases [36, 37]. CBD can inhibit T-cell-mediated chronic autoimmune myocarditis and myocardial reconstruction/fibrosis and improve myocardial dysfunction [38]. CBD induces functional Treg cells to induce immunosuppression under low-level T-cell stimulation [39]. CBD is used to treat brain damage caused by colitis, diabetic complications, drug-induced nephrotoxicity, alcohol

fat deposition or hypoxic-ischemia [40–42]. Treatment of mice with cannabidiol markedly attenuated the cisplatin-induced oxidative/nitrosative stress, inflammation, and cell death in the kidney, and it improved renal function [43]. In the prevention and treatment of skin and liver fibrosis, CBD inhibited collagen gene transcription and synthesis and prevented TGF-β and IL-4 induced fibroblast migration [44]. CBD treatment decreases the inflammatory and remodelling processes in a murine model of ovalbumin induced allergic asthma [45]. Previous studies have examined whether CBD has a protective effect on alcoholic fatty liver disease [46], but its effect on fibrosis and the detailed mechanisms in the context of inflammation remain unclear. We analyzed the effects of CBD on CCl₄-induced liver inflammation and collagen deposition using a well-established model that is very similar to human liver fibrosis [47, 48]. Colchicine, which is an alkaloid agent that is generally used to treat acute gout in the clinic, was used as the positive control for its effects on improving liver fibrosis and ameliorating liver function [49]. In this study, the CCl₄-induced mouse model was used to study the intervention effect of CBD on liver fibrosis and to explore whether its potential mechanism is related to the inhibition of NF-κB and activation of the PPAR-α signaling pathway and anti-inflammatory and antioxidant stress damage.

Increasingly, we found that CCl₄-induced liver fibrosis resulted in significant weight loss, increased liver weight, and increased serum AST and HA levels. Pathological analysis of liver tissue in the CCl₄ group showed massive liver cell necrosis, diffuse

**FIGURE 4**

Effects of CBD on TGF- β 1, α -SMA, and COL-1 in mice with CCl₄-induced liver fibrosis. (A) The effects of CBD on the protein expression of TGF- β 1, α -SMA, and COL-1 were measured by western blotting. (B–D) ImageJ software was used to measure the grey values of the bands. (E) The effect of CBD on the mRNA expression of TGF- β 1, α -SMA, and COL-1 was determined by q-PCR. The values represent the means \pm SEM ($n = 8$). * $p < 0.05$ vs. the control group, # $p < 0.05$ vs. the CCl₄ group, as determined by one-way ANOVA, followed by the LSD multiple comparisons test.

inflammatory cells and high levels of collagen, indicating that CCl₄ caused severe liver damage. This study showed that CBD reduced the levels of AST and HA and reduced inflammatory infiltration and collagen deposition in liver tissues, indicating that CBD significantly alleviates CCl₄-induced liver fibrosis, but there were similar effects between 4 mg/kg and 8 mg/kg CBD.

TGF- β 1 is an essential cytokine that regulates the production, degradation and accumulation of ECM and plays a significant role in the activation of HSCs. In normal liver tissue, the expression of TGF- β 1 in the liver is reduced. However, when liver injury occurs, HSCs, Kupffer cells (KCs) and other related cells produce large amounts of TGF- β 1, which activates HSCs to form myofibroblasts, promotes the production of ECM and inhibits matrix degradation, resulting in the accumulation of scar matrix and liver fibrosis [50, 51]. Activated HSCs secrete large amounts of fibrillar collagens, mainly in the form of α -SMA and COL-I [52, 53], and the expression of the COL-I gene could indicate the synthesis of

collagen. CBD inhibited the gene and protein expression of COL-I, α -SMA and TGF- β 1. However, within the CBD concentration range set by the experiment, there was no statistically significant difference between the 4 mg/kg and 8 mg/kg CBD groups in various detection results. These results indicated that CBD inhibited collagen formation to prevent liver fibrosis, and further research is needed to determine the signaling pathways that mediate this protective effect on the liver.

Inflammation is closely related to the development of CCl₄-induced liver fibrosis. IL-1 β is one of the main factors inducing fibrosis, which promotes the aggregation of fibroblasts and inflammatory cells, as well as collagen and fibrin synthesis, which further leads to ECM deposition. We examined a series of inflammatory genes, including IL-6, IL-1 β , and TNF- α , and found that CCl₄ enhanced the expression of IL-6, IL-1 β , and TNF- α . CBD blocked the inflammatory response in mouse liver tissue, which supported the anti-inflammatory effect of CBD, and

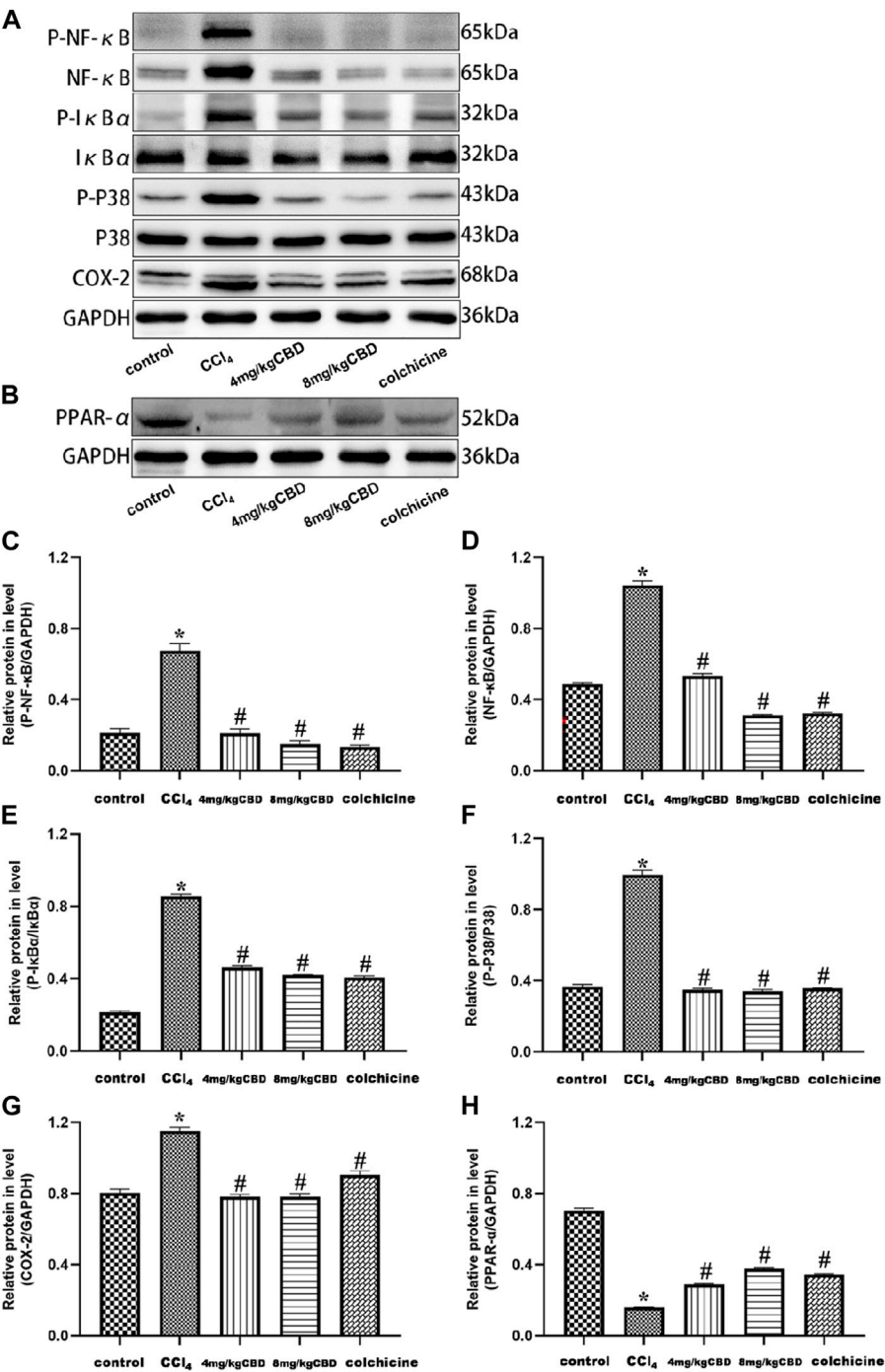


FIGURE 5 Effects of CBD on NF-κB- and PPAR-α-related proteins in mice with CCl₄-induced liver fibrosis. **(A,B)** The effects of CBD on the protein expression levels of NF-κB, p-NF-κB, p-IκBα, IκBα, p-p38 MAPK, p38 MAPK, COX-2, and PPAR-α were measured by western blotting. **(C–H)** ImageJ software was used to measure the grey values of the bands. The values represent the means ± SEM (*n* = 8). **p* < 0.05 vs. the control group, #*p* < 0.05 vs. the CCl₄ group, as determined by one-way ANOVA, followed by the LSD multiple comparisons test.

the underlying mechanism may be associated with the inhibition of inflammatory signaling pathways.

NF- κ B is an important nuclear transcription factor in the cell that participates in inflammatory and immune responses and can regulate cell apoptosis and the stress response [54, 55]. The phosphorylation of NF- κ B inhibitory protein (I κ B) enhanced the activity of NF- κ B, promoted the nuclear transport of the NF- κ B subunit, and triggered the transcription of downstream inflammatory genes, such as TNF- α , IL-6, and IL-1 β . According to reports, activation of the NF- κ B pathway can enhance the inflammatory response and EMT in liver cells. In the present study, we observed increased protein expression levels of total p-NF- κ B, NF- κ B, p-I κ B α /I κ B α , and downstream TNF- α , IL-6, and IL-1 β in CCL₄-induced mice. CBD treatment inhibited the activation of NF- κ B signaling and the increases in these inflammatory cytokines, suggesting that CBD may inhibit NF- κ B signaling and reduce the inflammatory response [56]. p38 MAPK mitogen-activated protein kinase belongs to the family of mitogen-activated protein kinases (MAPKs), which regulate the cell cycle, inflammation, growth, apoptosis, differentiation and other physiological processes. p38 MAPK can be phosphorylated by many extracellular agonists through the canonical MAPK pathway, and p-p38 MAPK can further regulate many substrates, such as transcription factors and PPARs [57]. PPAR belongs to the hormone nuclear receptor superfamily and consists of three subtypes (PPAR- α , PPAR- β/δ , and PPAR- γ) [58–60]. PPAR- α has important functions in regulating cells and is involved in cell proliferation, differentiation, oxidative/nitric stress, inflammation and immune response. PPAR- α has been reported to reverse fibrosis by reducing lipid peroxidation and inhibiting activation of HSCs and KCs [61, 62]. Furthermore, studies have shown that inhibiting p-p38 MAPK increased PPAR- α expression to protect the liver against concanavalin A-induced injury [57]. We examined the expression of COX-2, p-p38/p38 and PPAR- α and demonstrated that CBD treatment reduced COX-2 expression, inhibited p-p38 MAPK, activated the PPAR- α signaling pathway, and protected the liver from fibrosis. These findings suggest that CBD can protect against liver fibrosis by activating the PPAR- α signaling pathway, and this study may make great progress in the treatment of chronic liver fibrosis.

In summary, we have shown that intraperitoneal injection of CBD exerts potent anti-inflammatory and antifibrotic activities *in vivo*. Moreover, we found that the first time CBD efficacy in reducing CCL₄-induced hepatic fibrosis by multiple mechanisms. These mechanisms may involve inhibition of NF- κ B, activation of the PPAR- α pathway, and inhibition of oxidative stress. Based on these findings, CBD has the potential to be further developed as a treatment for hepatic fibrosis, especially as a combination therapy with the currently available therapies.

Author contributions

RM: Data curation, Investigation, Methodology, Validation, Writing–original draft, Writing–review and editing. NX: Methodology, Software, Writing–original draft. YS: Methodology, Writing–original draft. YaW: Methodology, Writing–original draft. PH: Software, Writing–original draft. YX: Supervision, Writing–review and editing. YZ: Supervision, Writing–review and editing. YuW: Methodology, Supervision, Writing–original draft, Writing–review and editing. All authors contributed to the article and approved the submitted version.

Data availability statement

The original contributions presented in the study are included in the article/supplementary material, further inquiries can be directed to the corresponding author.

Ethics statement

The animal study was approved by the Guizhou Medical University Animal Care Welfare Committee. The study was conducted in accordance with the local legislation and institutional requirements.

Funding

The author(s) declare that financial support was received for the research, authorship, and/or publication of this article. National Natural Science Foundation of China (81860118 and 81460125), Guizhou Provincial Health Commission Science and Technology Fund (gzwkj2021 -119).

Conflict of interest

The authors declare that the research was conducted in the absence of any commercial or financial relationships that could be construed as a potential conflict of interest.

Publisher's note

Please note that the review of this paper was conducted at the previous publisher, SAGE.

References

- Aydın MM, Akçalı KC. Liver fibrosis. *Turk J Gastroenterol* (2018) **29**:14–21. doi:10.5152/tjg.2018.17330
- Moon AM, Singal AG, Tapper EB. Contemporary epidemiology of chronic liver disease and cirrhosis. *Clin Gastroenterol Hepatol* (2020) **18**:2650–66. doi:10.1016/j.cgh.2019.07.060
- Asrani SK, Devarbhavi H, Eaton J, Kamath PS. Burden of liver diseases in the world. *J Hepatol* (2019) **70**:151–71. doi:10.1016/j.jhep.2018.09.014
- Guo Y, Liang X, Meng M, Chen H, Wei X, Li M, et al. Hepatoprotective effects of yulangsang flavone against carbon tetrachloride (CCl₄)-induced hepatic fibrosis in rats. *Phytomedicine* (2017) **33**:28–35. doi:10.1016/j.phymed.2017.07.005
- Parola M, Pinzani M. Liver fibrosis: pathophysiology, pathogenetic targets and clinical issues. *Mol Aspects Med* (2019) **65**:37–55. doi:10.1016/j.mam.2018.09.002
- Altamirano-Barrera A, Barranco-Fragoso B, Méndez-Sánchez N. Management strategies for liver fibrosis. *Ann Hepatol* (2017) **16**:48–56. doi:10.5604/16652681.1226814
- Tsuchida T, Friedman SL. Mechanisms of hepatic stellate cell activation. *Nat Rev Gastroenterol Hepatol* (2017) **14**:397–411. doi:10.1038/nrgastro.2017.38
- Xiang D, Zou J, Zhu X, Chen X, Luo J, Kong L, et al. Physalin D attenuates hepatic stellate cell activation and liver fibrosis by blocking TGF- β /Smad and YAP signaling. *Phytomedicine* (2020) **78**:153294. doi:10.1016/j.phymed.2020.153294
- Mu M, Zuo S, Wu RM, Deng KS, Lu S, Zhu JJ, et al. Ferulic acid attenuates liver fibrosis and hepatic stellate cell activation via inhibition of TGF- β /Smad signaling pathway. *Drug Des Develop Ther* (2018) **12**:4107–15. doi:10.2147/dddt.s186726
- Liu N, Feng J, Lu X, Yao Z, Liu Q, Lv Y, et al. Isorhamnetin inhibits liver fibrosis by reducing autophagy and inhibiting extracellular matrix formation via the TGF- β /smad3 and TGF- β /p38 MAPK pathways. *Mediators Inflamm* (2019) **2019**:6175091–14. doi:10.1155/2019/6175091
- Wang K, Fang S, Liu Q, Gao J, Wang X, Zhu H, et al. TGF- β 1/p65/MAT2A pathway regulates liver fibrogenesis via intracellular SAM. *EBioMedicine* (2019) **42**:458–69. doi:10.1016/j.ebiom.2019.03.058
- Espin-Palazón R, Traver D. The NF- κ B family: key players during embryonic development and HSC emergence. *Exp Hematol* (2016) **44**:519–27. doi:10.1016/j.exphem.2016.03.010
- Zeng S, Feirt N, Goldstein M, Guarrera J, Ippagunta N, Ekong U, et al. Blockade of receptor for advanced glycation end product (RAGE) attenuates ischemia and reperfusion injury to the liver in mice. *Hepatology* (2004) **39**:422–32. doi:10.1002/hep.20045
- Hines IN, Grisham MB. Divergent roles of superoxide and nitric oxide in liver ischemia and reperfusion injury. *J Clin Biochem Nutr* (2010) **48**:50–6. doi:10.3164/jcbs.11-016fr
- Abe Y, Hines IN, Zibari G, Pavlick K, Gray L, Kitagawa Y, et al. Mouse model of liver ischemia and reperfusion injury: method for studying reactive oxygen and nitrogen metabolites *in vivo*. *Free Radic Biol Med* (2009) **46**:1–7. doi:10.1016/j.freeradbiomed.2008.09.029
- Hamada T, Tsuchihashi S, Avanesyan A, Duarte S, Moore C, Busuttill RW, et al. Cyclooxygenase-2 deficiency enhances Th2 immune responses and impairs neutrophil recruitment in hepatic ischemia/reperfusion injury. *J Immunol* (2008) **180**:1843–53. doi:10.4049/jimmunol.180.3.1843
- Yang H, Xuefeng Y, Shandong W, Jianhua X. COX-2 in liver fibrosis. *Clinica Chim Acta* (2020) **506**:196–203. doi:10.1016/j.cca.2020.03.024
- González-Mañán D, D'Espessailles A, Dossi CG, San Martín M, Mancilla RA, Tapia GS. Rosa mosqueta oil prevents oxidative stress and inflammation through the upregulation of PPAR- α and NRF2 in C57BL/6J mice fed a high-fat diet. *J Nutr* (2017) **147**:579–88. doi:10.3945/jn.116.243261
- Rong C, Lee Y, Carmona N, Cha D, Ragguett R, Rosenblat J, et al. Cannabidiol in medical marijuana: research vistas and potential opportunities. *Pharmacol Res* (2017) **121**:213–8. doi:10.1016/j.phrs.2017.05.005
- Weiss L, Zeira M, Reich S, Har-Noy M, Mechoulam R, Slavin S, et al. Cannabidiol lowers incidence of diabetes in non-obese diabetic mice. *Autoimmunity* (2006) **39**:143–51. doi:10.1080/08916930500356674
- Atalay S, Jarocka-Karpowicz I, Skrzydlewska E. Antioxidant and anti-inflammatory properties of cannabidiol. *Antioxidants (Basel)* (2019) **9**:21. doi:10.3390/antiox9010021
- De Ternay J, Naassila M, Nourredine M, Louvet A, Bailly F, Sescousse G, et al. Therapeutic prospects of cannabidiol for alcohol use disorder and alcohol-related damages on the liver and the brain. *Front Pharmacol* (2019) **10**:627. doi:10.3389/fphar.2019.00627
- Yang L, Rozenfeld R, Wu D, Devi LA, Zhang Z, Cederbaum A. Cannabidiol protects liver from binge alcohol-induced steatosis by mechanisms including inhibition of oxidative stress and increase in autophagy. *Free Radic Biol Med* (2014) **68**:260–7. doi:10.1016/j.freeradbiomed.2013.12.026
- del Zoppo GJ, Frankowski H, Gu YH, Osada T, Kanazawa M, Milner R, et al. Microglial cell activation is a source of metalloproteinase generation during hemorrhagic transformation. *J Cereb Blood Flow Metab* (2012) **32**:919–32. doi:10.1038/jcbfm.2012.11
- Mukhopadhyay P, Rajesh M, Horváth B, Bátkai S, Park O, Tanchian G, et al. Cannabidiol protects against hepatic ischemia/reperfusion injury by attenuating inflammatory signaling and response, oxidative/nitrative stress, and cell death. *Free Radic Biol Med* (2011) **50**:1368–81. doi:10.1016/j.freeradbiomed.2011.02.021
- Huang W, Zheng Y, Feng H, Ni L, Ruan Y, Zou X, et al. Total phenolic extract of *Euscaphis konishii* hayata Pericarp attenuates carbon tetrachloride (CCl₄)-induced liver fibrosis in mice. *Biomed Pharmacother* (2020) **125**:109932. doi:10.1016/j.biopha.2020.109932
- Zhang CY, Yuan WG, He P, Lei JH, Wang CX. Liver fibrosis and hepatic stellate cells: etiology, pathological hallmarks and therapeutic targets. *World J Gastroenterol* (2016) **22**:10512–22. doi:10.3748/wjg.v22.i48.10512
- Ewing LE, Skinner CM, Quick CM, Kennon-McGill S, McGill MR, Walker LA, et al. Hepatotoxicity of a cannabidiol-rich cannabis extract in the mouse model. *Molecules* (2019) **24**:1694. doi:10.3390/molecules24091694
- Seltzer ES, Watters AK, MacKenzie D, Jr, Granat LM, Zhang D. Cannabidiol (CBD) as a promising anti-cancer drug. *Cancers (Basel)* (2020) **12**:3203. doi:10.3390/cancers12113203
- Nichols JM, Kaplan BLF. Immune responses regulated by Cannabidiol. *Cannabis Cannabinoid Res* (2020) **5**:12–31. doi:10.1089/can.2018.0073
- Majdi F, Taheri F, Salehi P, Motaghinejad M, Safari S. Cannabinoids Δ (9)-tetrahydrocannabinol and cannabidiol may be effective against methamphetamine induced mitochondrial dysfunction and inflammation by modulation of Toll-like type-4(Toll-like 4) receptors and NF- κ B signaling. *Med Hypotheses* (2019) **133**:109371. doi:10.1016/j.mehy.2019.109371
- Huang Y, Wan T, Pang N, Zhou Y, Jiang X, Li B, et al. Cannabidiol protects livers against nonalcoholic steatohepatitis induced by high-fat high cholesterol diet via regulating NF- κ B and NLRP3 inflammasome pathway. *J Cell Physiol* (2019) **234**:21224–34. doi:10.1002/jcp.28728
- Ma H, Xu F, Liu C, Seeram NP. A network pharmacology approach to identify potential molecular targets for Cannabidiol's anti-inflammatory activity. *Cannabis Cannabinoid Res* (2021) **6**:288–99. doi:10.1089/can.2020.0025
- Lim K, See Y, Lee J. A systematic review of the effectiveness of medical cannabis for psychiatric, movement and neurodegenerative disorders. *Clin Psychopharmacol Neurosci* (2017) **15**:301–12. doi:10.9758/cpn.2017.15.4.301
- Iffland K, Grotenhermen F. An update on safety and side effects of cannabidiol: a review of clinical data and relevant animal studies. *Cannabis Cannabinoid Res* (2017) **2**:139–54. doi:10.1089/can.2016.0034
- Rieder SA, Chauhan A, Singh U, Nagarkatti M, Nagarkatti P. Cannabinoid-induced apoptosis in immune cells as a pathway to immunosuppression. *Immunobiology* (2010) **215**:598–605. doi:10.1016/j.imbio.2009.04.001
- Tahamtan A, Tavakoli-Yaraki M, Rygiel TP, Mokhtari-Azad T, Salimi V. Effects of cannabinoids and their receptors on viral infections. *J Med Virol* (2016) **88**:1–12. doi:10.1002/jmv.24292
- Lee WS, Erdelyi K, Matyas C, Mukhopadhyay P, Varga ZV, Liaudet L, et al. Cannabidiol limits T cell-mediated chronic autoimmune myocarditis: implications to autoimmune disorders and organ transplantation. *Mol Med* (2016) **22**:136–46. doi:10.2119/molmed.2016.00007
- Dhital S, Stokes JV, Park N, Seo KS, Kaplan BL. Cannabidiol (CBD) induces functional tregs in response to low-level T cell activation. *Cell Immunol* (2017) **312**:25–34. doi:10.1016/j.cellimm.2016.11.006
- Rajesh M, Mukhopadhyay P, Bátkai S, Patel V, Saito K, Matsumoto S, et al. Cannabidiol attenuates cardiac dysfunction, oxidative stress, fibrosis, and inflammatory and cell death signaling pathways in diabetic cardiomyopathy. *J Am Coll Cardiol* (2010) **56**:2115–25. doi:10.1016/j.jacc.2010.07.033
- Charytoniuk T, Sztolsztener K, Bielawiec P, Chabowski A, Konstantynowicz-Nowicka K, Harasim-Symbor E. Cannabidiol downregulates myocardial *de novo* ceramide synthesis pathway in a rat model of high-fat diet-induced obesity. *Int J Mol Sci* (2022) **23**:2232. doi:10.3390/ijms23042232
- Burggren AC, Shirazi A, Ginder N, London ED. Cannabis effects on brain structure, function, and cognition: considerations for medical uses of cannabis and its derivatives. *The Am J Drug Alcohol Abuse* (2019) **45**:563–79. doi:10.1080/00952990.2019.1634086

43. Pan H, Mukhopadhyay P, Rajesh M, Patel V, Mukhopadhyay B, Gao B, et al. Cannabidiol attenuates cisplatin-induced nephrotoxicity by decreasing oxidative/nitrosative stress, inflammation, and cell death. *J Pharmacol Exp Ther* (2009) **328**: 708–14. doi:10.1124/jpet.108.147181
44. Del Río C, Ruiz-Pino F, Prados ME, Fiebich BL, Tena-Sempere M, Muñoz E. Cannabidiol markedly alleviates skin and liver fibrosis. *Front Pharmacol* (2022) **13**: 981817. doi:10.3389/fphar.2022.981817
45. Vuolo F, Abreu SC, Michels M, Xisto DG, Blanco NG, Hallak JE, et al. Cannabidiol reduces airway inflammation and fibrosis in experimental allergic asthma. *Eur J Pharmacol* (2019) **843**:251–9. doi:10.1016/j.ejphar.2018.11.029
46. Wang Y, Mukhopadhyay P, Cao Z, Wang H, Feng D, Hasko G, et al. Cannabidiol attenuates alcohol-induced liver steatosis, metabolic dysregulation, inflammation and neutrophil-mediated injury. *Sci Rep* (2017) **7**:12064. doi:10.1038/s41598-017-10924-8
47. Crespo Yanguas S, Cogliati B, Willebrords J, Maes M, Colle I, van den Bossche B, et al. Experimental models of liver fibrosis. *Arch Toxicol* (2016) **90**:1025–48. doi:10.1007/s00204-015-1543-4
48. Unsal V, Cicek M, Sabancilar İ. Toxicity of carbon tetrachloride, free radicals and role of antioxidants. *Rev Environ Health* (2021) **36**:279–95. doi:10.1515/reveh-2020-0048
49. Schlesinger N, Schumacher R, Catton M, Maxwell L. Colchicine for acute gout. *Cochrane database Syst Rev* (2006) **4**:CD006190. doi:10.1002/14651858.cd006190
50. Mahmoud AM, Hozayen WG, Hasan IH, Shaban E, Bin-Jumah M. Umbelliferone ameliorates CCl₄-induced liver fibrosis in rats by upregulating PPARgamma and attenuating oxidative stress, inflammation, and TGF-beta1/Smad3 signaling. *Inflammation* (2019) **42**:1103–16. doi:10.1007/s10753-019-00973-8
51. Dooley S, ten Dijke P. TGF-β in progression of liver disease. *Cell Tissue Res* (2012) **347**:245–56. doi:10.1007/s00441-011-1246-y
52. Wang M, Zhang M, Fu L, Lin J, Zhou X, Zhou P, et al. Liver-targeted delivery of TSG-6 by calcium phosphate nanoparticles for the management of liver fibrosis. *Theranostics* (2020) **10**:36–49. doi:10.7150/thno.37301
53. Lakner AM, Steuerwald NM, Walling TL, Ghosh S, Li T, McKillop IH, et al. Inhibitory effects of microRNA 19b in hepatic stellate cell-mediated fibrogenesis. *Hepatology* (2012) **56**:300–10. doi:10.1002/hep.25613
54. Chen Y, Zhao C, Liu X, Wu G, Zhong J, Zhao T, et al. Plumbagin ameliorates liver fibrosis via a ROS-mediated NF-κB signaling pathway *in vitro* and *in vivo*. *Biomed Pharmacother* (2019) **116**:108923. doi:10.1016/j.biopha.2019.108923
55. Yoo W, Lee J, Noh KH, Lee S, Jung D, Kabir MH, et al. Progranulin attenuates liver fibrosis by downregulating the inflammatory response. *Cell Death Dis.* (2019) **10**:758. doi:10.1038/s41419-019-1994-2
56. Coulthard LR, White DE, Jones DL, McDermott MF, Burchill SA. p38(MAPK): stress responses from molecular mechanisms to therapeutics. *Trends Mol Med* (2009) **15**:369–79. doi:10.1016/j.molmed.2009.06.005
57. Lu X, Liu T, Chen K, Xia Y, Dai W, Xu S, et al. Isorhamnetin: a hepatoprotective flavonoid inhibits apoptosis and autophagy via P38/PPAR-α pathway in mice. *Biomed Pharmacother* (2018) **103**:800–11. doi:10.1016/j.biopha.2018.04.016
58. Du X, Wu M, Tian D, Zhou J, Wang L, Zhan L. MicroRNA-21 contributes to acute liver injury in LPS-induced sepsis mice by inhibiting PPARα expression. *PPAR Res* (2020) **2020**:1–7. doi:10.1155/2020/6633022
59. Morinishi T, Tokuhara Y, Ohsaki H, Ibuki E, Kadota K, Hirakawa E. Activation and expression of peroxisome proliferator-activated receptor alpha are associated with tumorigenesis in colorectal carcinoma. *PPAR Res* (2019) **2019**:1–9. doi:10.1155/2019/7486727
60. Mello T, Materozzi M, Galli A. PPARs and mitochondrial metabolism: from NAFLD to HCC. *PPAR Res* (2016) **2016**:1–18. doi:10.1155/2016/7403230
61. Ip E, Farrell G, Hall P, Robertson G, Leclercq I. Administration of the potent PPARα agonist, Wy-14,643, reverses nutritional fibrosis and steatohepatitis in mice. *Hepatology* (2004) **39**:1286–96. doi:10.1002/hep.20170
62. Pawlak M, Lefebvre P, Staels B. Molecular mechanism of PPARα action and its impact on lipid metabolism, inflammation and fibrosis in non-alcoholic fatty liver disease. *J Hepatol* (2015) **62**:720–33. doi:10.1016/j.jhep.2014.10.039



OPEN ACCESS

*CORRESPONDENCE

Jonathan Shannahan,
✉ jshannah@purdue.edu

RECEIVED 02 February 2024

ACCEPTED 05 April 2024

PUBLISHED 22 April 2024

CITATION

Shinde A and Shannahan J (2024),
Inhalation exposure-induced toxicity
and disease mediated via
mTOR dysregulation.
Exp. Biol. Med. 249:10135.
doi: 10.3389/ebm.2024.10135

COPYRIGHT

© 2024 Shinde and Shannahan. This is
an open-access article distributed
under the terms of the [Creative
Commons Attribution License \(CC BY\)](#).
The use, distribution or reproduction in
other forums is permitted, provided the
original author(s) and the copyright
owner(s) are credited and that the
original publication in this journal is
cited, in accordance with accepted
academic practice. No use, distribution
or reproduction is permitted which does
not comply with these terms.

Inhalation exposure-induced toxicity and disease mediated via mTOR dysregulation

Akshada Shinde and Jonathan Shannahan*

School of Health Sciences, College of Health and Human Sciences, Purdue University, West Lafayette, IN, United States

Abstract

Environmental air pollution is a global health concern, associated with multiple respiratory and systemic diseases. Epidemiological supports continued urbanization and industrialization increasing the prevalence of inhalation exposures. Exposure to these inhaled pollutants induces toxicity via activation of numerous cellular mechanisms including oxidative stress, autophagy, disrupted cellular metabolism, inflammation, tumorigenesis, and others contributing to disease development. The mechanistic target of rapamycin (mTOR) is a key regulator involved in various cellular processes related to the modulation of metabolism and maintenance of homeostasis. Dysregulation of mTOR occurs following inhalation exposures and has also been implicated in many diseases such as cancer, obesity, cardiovascular disease, diabetes, asthma, and neurodegeneration. Moreover, mTOR plays a fundamental role in protein transcription and translation involved in many inflammatory and autoimmune diseases. It is necessary to understand inhalation exposure-induced dysregulation of mTOR since it is key regulator which may contribute to numerous disease processes. This mini review evaluates the available literature regarding several types of inhalation exposure and their impacts on mTOR signaling. Particularly we focus on the mTOR signaling pathway related outcomes of autophagy, lipid metabolism, and inflammation. Furthermore, we will examine the implications of dysregulated mTOR pathway in exposure-induced diseases. Throughout this mini review, current gaps will be identified related to exposure-induced mTOR dysregulation which may enable the targeting of mTOR signaling for the development of therapeutics.

KEYWORDS

mTOR, inhalation toxicology, lung disease, autophagy, lipid homeostasis, metabolism, inflammation

Impact statement

mTOR is a key regulator of numerous cellular processes often disrupted in numerous disease scenarios. Inhalation exposures are prevalent in environmental and occupational settings and contribute to both pulmonary and systemic diseases. Inhalation exposure-induced toxicity and diseases are associated with outcomes of

mTOR dysregulation including autophagy, lipid metabolism, and inflammation. This minireview uniquely summarizes and integrates our current knowledge associated with inhalation exposure-induced dysregulation of mTOR contributing to toxicity and disease. This perspective is impactful as it highlights a complex and primary mediator to numerous disease processes contributing to human health risks associated with inhalation exposures. Further, a thorough understanding of mTOR-mediated mechanisms of toxicity and disease are necessary for the development of therapeutic strategies. Due to mTOR's numerous cellular regulatory functions these strategies could be applied broadly to multiple exposures and disease scenarios.

Introduction

Inhalation exposures are a significant global health concern associated with a variety of pulmonary and systemic diseases. Diseases associated with inhalation exposures include asthma, chronic obstructive pulmonary disease (COPD), pulmonary fibrosis, cancer, cardiovascular disease, and others [1]. Inhalation of environmental air pollution is associated with the induction of cellular responses including, oxidative stress, altered metabolism, autophagy, cell death and others. These cellular toxicity mechanisms contribute to disease development and progression [2]. For example, tobacco smoke exposure can result in development of COPD which is a complex lung disease involving destruction of the lung epithelium, bronchial inflammation, and fibrinogenesis. Individuals with COPD have demonstrated increased expression of microtubule-associated protein 1A/1B-light chain 3 (LC3) protein, a marker of autophagosome formation in lungs of COPD patients, suggesting of induction of autophagy [3]. Elucidation of molecular signaling mediating toxicity following inhalation exposures is necessary to develop interventional strategies to address health outcomes [4]. Mechanistic target of rapamycin (mTOR) represents a key regulator of multiple cellular processes, many of which are dysregulated following inhalation exposures which may contribute to the progression of disease. Specifically, mTOR regulates cell proliferation and survival, metabolism, autophagy, inflammation, oxidative stress, and DNA damage repair. Dysregulation of mTOR has been associated with numerous diseases including cancer, fibrosis, COPD, cardiovascular disease, autoimmune diseases, and metabolic disease [5, 6]. In this mini review we will assess the current literature regarding mTOR dysregulation associated with inhalation exposures and its contribution to toxicity and disease development. Additionally, we will highlight current knowledge gaps as

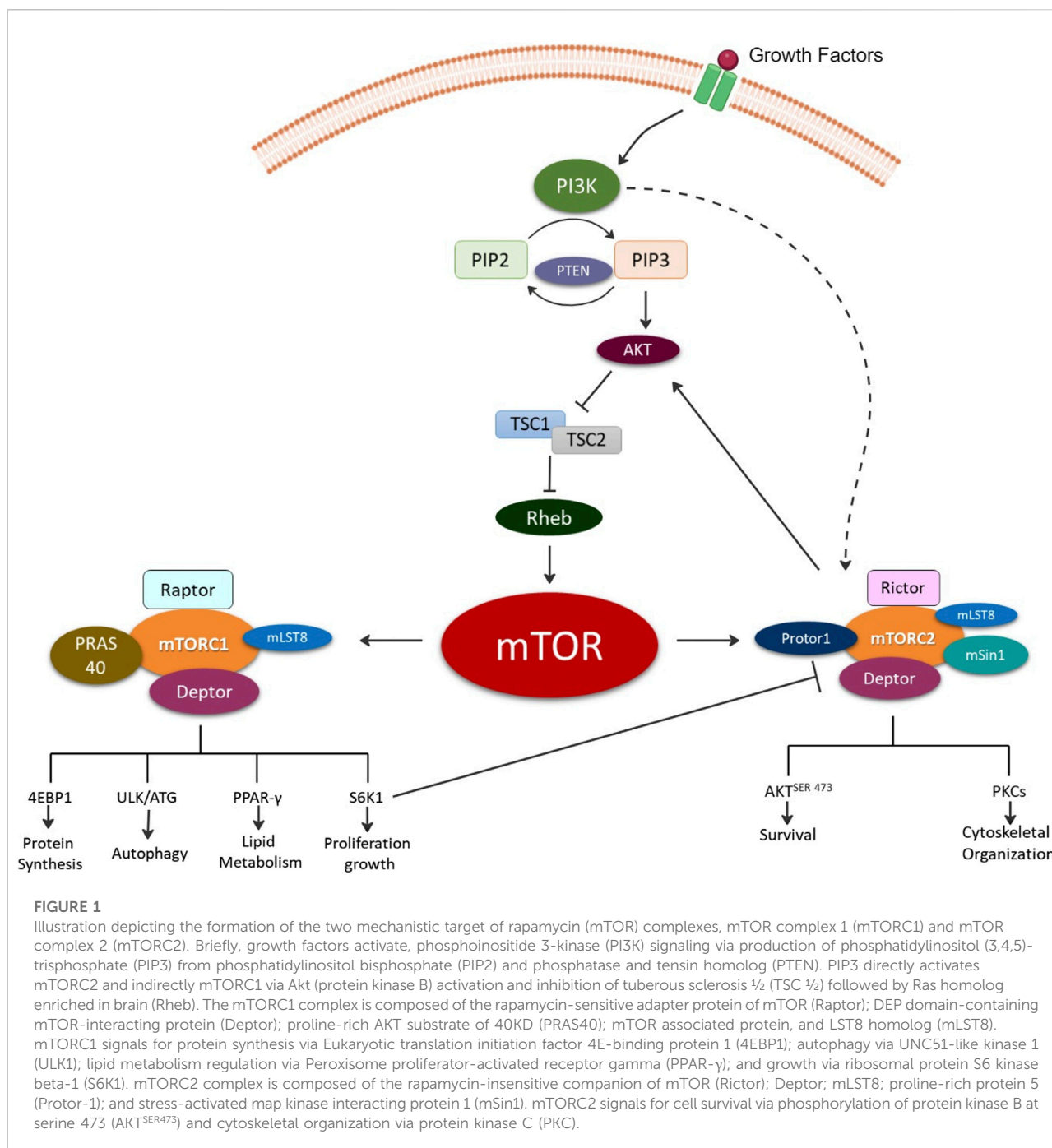
well as the potential to target mTOR-mediated mechanisms for therapeutic strategies.

mTOR complexes

The discovery of rapamycin, a secondary metabolite originally observed to be produced by bacterium, led to a search for its cellular target, known as target of rapamycin (TOR) [7]. Several independent studies in 1994 led to the discovery the mammalian homologue of TOR or the mTOR [8]. mTOR is a 289-kDa serine/threonine kinase belonging to the phosphoinositide 3-kinases (PI3K)-related kinase family which is highly conserved across species. mTOR mediates cellular growth and proliferation via governing of intracellular adenosine triphosphate (ATP) levels based on extracellular nutrients. Further, it is involved in various cellular processes such as cell growth, survival, autophagy, and metabolism. These functions are mediated by two complexes mTOR complex 1 (mTORC1) and mTOR complex 2 (mTORC2) [5]. The upstream signaling resulting in formation of mTORC1 and mTORC2 as well as their distinct downstream signaling regulating cellular processes have previously been thoroughly reviewed elsewhere and are summarized in Figure 1 [8–14].

mTORC1 consists of the core subunits of 1) mTOR, 2) regulatory-associated protein of mTOR (Raptor), and 3) mammalian lethal with SEC13 protein 8 (mLST8) [15] (Figure 1). mTORC1 regulates biosynthesis of protein, lipids, and nucleic acids via transcriptional, translational, and post-translational mechanisms with the involvement of its substrate ribosomal protein S6 kinase (rpS6K) and eukaryotic translation initiation factor (eIF) 4E-binding protein (4E-BP) [15]. It is also involved in ATP production via reducing NADPH and certain macromolecule precursors involved in biosynthesis [15]. Rapamycin and its related compounds, called rapalogs, are recognized as allosteric inhibitors of mTORC1. These include two endogenous inhibitors, DEP domain-containing mTOR-interacting protein (DEPTOR) and 40kDa Proline-rich Akt substrate (PRAS40). Rapamycin and other rapalogs primarily target mTORC1 making them useful in specifically regulating mTORC1 and its associated signaling enabling mechanistic investigations of mTORC1 signaling in laboratory settings.

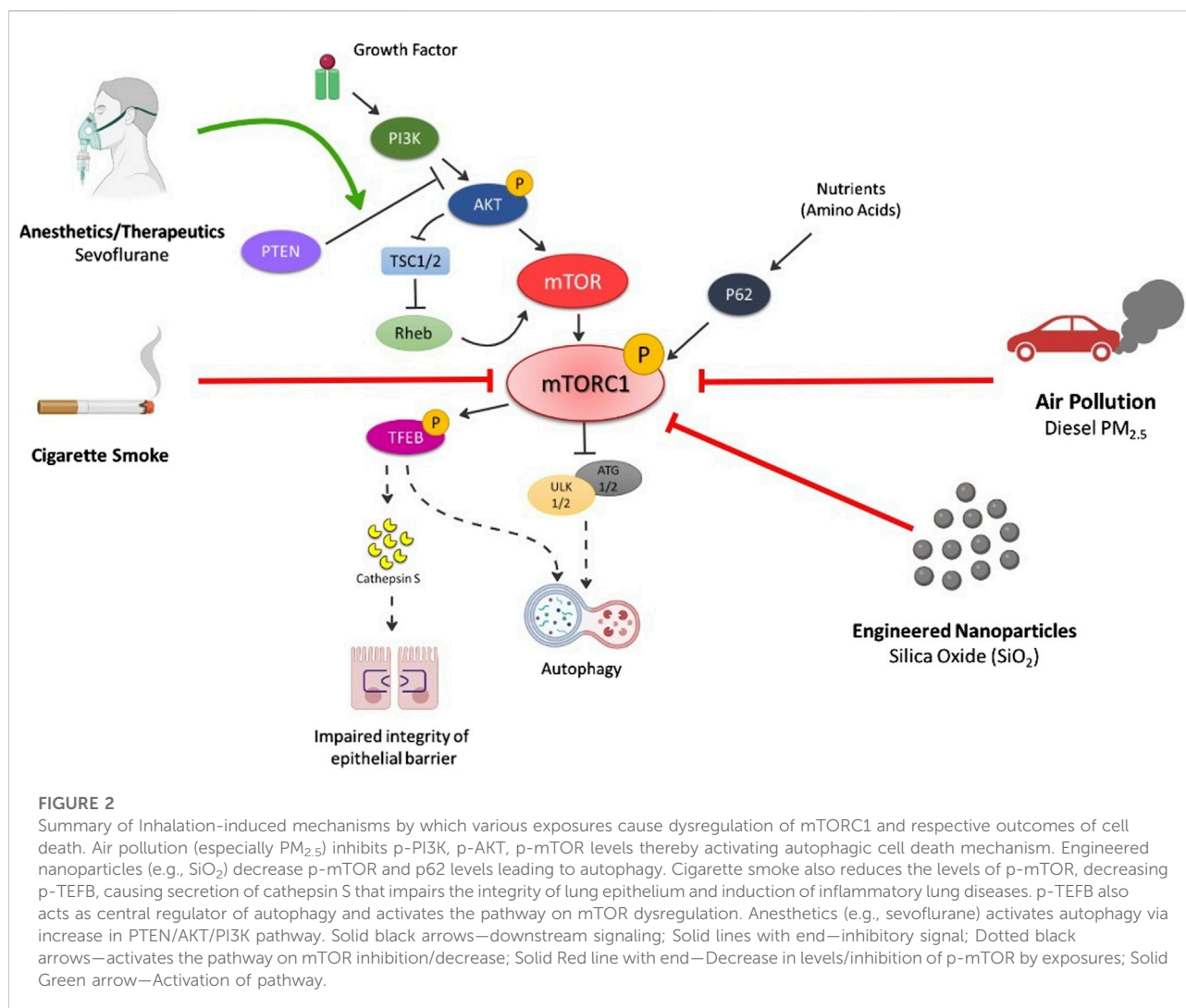
mTORC2 consists of mTOR, DEPTOR, and mLST8, along with unique components Rapamycin-insensitive companion of mTOR (Rictor), protein-binding Rictor (Protor) and stress-activated protein kinase-interacting protein 1 (Sin1). Rictor's primary function is the recruitment of substrates. mTORC2 does not bind Rapamycin nor impact S6K1. Thus, Raptor (mTORC1 subunit) and Rictor (mTORC2 subunit) independently associate with mTOR resulting in differential signaling outcomes and are utilized to define the complexes.



Inhalation exposure modified mTOR signaling contributing to disease via autophagy

Several inhalation exposures target the mTOR pathway, disrupting normal cellular and molecular pathways [6] (Figure 2). These exposures include commonly inhaled

exposures including ambient particulate matter, engineered nanoparticles (NPs), anesthetics and therapeutics, and cigarette smoke. Autophagy, a cellular degradation pathway directs cells to maintain their homeostatic function such as protein turnover. Autophagy is a cellular adaptive defense mechanism and occurs in stressful environments such as during low nutrient situations, high energy demands,



infection, following organelle damage, etc. In general, the autophagic process involves formation of autophagosome that fuses with lysosome resulting in formation of autolysosome that is responsible for breakdown and recycling of sequestered cytosolic material. In mammalian cells, the conversion of LC3B protein from its free form, LC3B-I to the phosphatidylethanolamine-conjugated form, LC3B-II, is an important hallmark in monitoring the autophagic flux [16,17]. mTOR is one of the primary regulators of autophagy, which activates in nutrient rich environments, thereby inhibiting autophagy but inhibited mTOR activates the autophagic process. Different forms of illness such as cancer, neurodegenerative disorders, cardiovascular diseases, diabetes are associated with dysregulated mTOR signaling due to imbalance of nutrient and energy demands, therefore, suggesting malfunctioned autophagy [18–23]. Further, many inhalation exposures result in the dysregulation of mTOR signaling and may contribute to disease via autophagy.

Respiratory implications

Exhaust fumes from automobiles, emissions from industries and refineries including power generating stations are major sources of outdoor pollution. In contrast, cooking, burning fuel, dry cleaning, and domestic heating activities contribute as indoor sources of pollution. The mixture of particulate matter (PM) and gases are inhaled and penetrated into lungs, leading to pulmonary and systemic health effects [24]. In healthy lung tissue, mTORC1 is basally activated and the autophagy-related protein LC3 II is suppressed, maintaining cell homeostasis, and protecting cell damage from stress. However, lung injury following exposures can result in the inhibition of mTORC1 causing the upregulation of LC3 II, leading to development of pulmonary disease. Intratracheal instillation of PM with a diameter of less than 2.5 microns (PM_{2.5}) in mice lungs induces pulmonary damage with vascular hyperpermeability and inflammatory responses.

Mechanistically, PM_{2.5} upregulates Toll-like receptor (TLR) expression, releasing inflammatory cytokines. Additionally, PM_{2.5} inhibits mTOR signaling pathway, decreasing the levels of phosphorylated mTOR, Protein kinase B (Akt), and PI3K [25], worsening the lung injury. Consequently, the study reported a strong connection of complex signaling network between TLR, one of the sensors for autophagy and mTOR, also involved in lung inflammation [25, 26]. These findings suggest disruption of mTOR signaling contributes to PM-induced lung damage.

The fundamental insights of risk factors such as lack of physical activity, high calorie intake and high glycemic index have been well known for decades. However, a strong link between environmental factors in air and predisposition of diabetes mellitus has been growing recently. Moreover, extensive data from high fat diet induced murine model and humans suggests ambient air pollution with PM_{2.5} exposure is critically associated with pathophysiological disturbances in metabolic disease conditions [27]. Autophagy serves as a protective mechanism in pancreatic B cell survival. Chronic activation of mTORC1 inhibits the autophagy and facilitates the progression of type 2 diabetes mellitus and insulin resistance [28–30]. Activated mTOR stimulates S6K1 to inhibit insulin receptor substrate-1 (IRS1), affecting the insulin pathway, causing insulin resistance [31–33]. mTOR also mediates lipogenesis and formation of adipose tissue. Role of S6K1 has been investigated in diet-induced obesity mice model, which suggested mice lacking S6K1 are protected against obesity [34]. In addition, the study suggests exposure to PM_{2.5} exacerbates a key defect in insulin signaling via alterations in PI3K/AKT pathway increasing inflammation at adipose tissue macrophages [27]. Prospectively, abnormalities in PI3K/AKT pathway can be suggestive of cascade activation of mTOR implicating its potential in exaggerating inflammatory response in metabolic disease.

Metal nanoparticles have a wide range of applications from medicine to consumer products and incorporation into industrial processes. With potential manufacturing and widespread use of nanotechnology, exposure to engineered nanoparticles has also increased among consumers and manufacturers. Exposure to nanoparticles composed of metals and metal oxides have potential for adverse environmental and health effects [35]. Inhalation is the primary route of nanoparticle exposure in environmental and occupational settings, resulting in pulmonary damage leading to lung injury and development of respiratory diseases [36]. Several studies have reported autophagy is a consequence of metal nanoparticle exposure contributing to toxicity [37–41]. In particular, mesoporous silica nanoparticles induce autophagy in human bronchial epithelial cells (BEAS-2B) via mTOR inhibition, in a dose-dependent manner [42]. Specifically, mesoporous silica nanoparticle exposure resulted in decreased phosphorylation of mTOR and p62 levels, suggesting induction of autophagy, which was further confirmed in mouse lungs exposed to

mesoporous silica nanoparticles via intratracheal instillation [42]. This silica-induced autophagy leads to macrophage activation, stimulating lung fibroblasts activity and progression of silicosis (pulmonary fibrosis) [43]. Overall, nanoparticle inhalation exposure may cause dysregulation of mTOR signaling inducing autophagy, potentially contributing to pulmonary damage and other respiratory health concerns.

Neurological implications

Air pollution and nanoparticle exposures have the potential to induce neurotoxicity via direct interactions following transport from the lung to the brain or indirectly via secondary mechanisms. In particular, nanomaterials have applications in medicine as drug delivery systems due to their ability to increase drug bioavailability. However, some nanomaterials have the ability to produce reactive oxygen species (ROS), inducing oxidative stress leading to detrimental effects on the brain. ROS are produced in response to xenobiotics and environmental stressors and as a by-product of oxygen metabolism. An imbalance in production and removal of these ROS by biological system is termed as oxidative stress. This highly reactive oxygen containing species induces mitochondrial dysfunction and stimulates various signaling proteins kinases. These oxidative damage conditions can initiate autophagosome formation inducing autophagy [44, 45]. In biological system, NPs tends to form protein-NP corona depending on protein affinity and NPs characteristics. Additionally, NPs functions as molecular chaperon to carry out protein folding, stabilization and protein aggregates. However, alterations in formation of stable corona and high protein concentration can result in accumulation of protein aggregates [46]. Autophagy is crucial in clearing toxic intracellular proteins and aggregates [amyloid- β (A β), mutant huntingtin, α -synuclein, and, phosphor-tau] which contribute to neurodegenerative diseases [47, 48]. Glycogen synthase kinase-3 beta (GSK3 β), the main kinase that phosphorylates tau protein, is a component of the PI3K/AKT/mTOR signaling pathway. Increased expression of GSK3 β can lead to hyperphosphorylation of tau protein via activation of mTOR, resulting in its aggregation and the formation of neurofibrillary tangles, which are a major neuropathological feature of Alzheimer's disease [49–52]. Furthermore, it has been evidently reported that air pollution with PM_{0.1} triggers the development of central nervous system disorders such as Alzheimer's, Parkinson's and stroke. An investigation on exposure of PM_{0.1} composed of aluminum emphasized the generation of ROS with association of autophagosome and oxidative DNA damage in neuronal cells. Interestingly, nanoparticles are proposed to cause autophagy by oxidative stress mechanism resulting in mitochondrial damage and accumulation of proteins. Hence, the likelihood of PM_{0.1}

exposure generating ROS that can induce autophagy contributing to neuronal damage and development of neurodegenerative diseases should not be disregarded [46].

Modern general anesthesia methods ensure the safety of numerous surgeries each year [53]. In clinical settings, the most utilized inhalational anesthetics are isoflurane, sevoflurane, and desflurane. Research on the safety of these anesthetics has indicated they can have both beneficial and harmful impacts on various organs, including the lungs, trachea, diaphragm muscle, liver, and kidneys [54]. Further, the use of anesthetic agents could potentially cause harm to the development of neurocognition, particularly during early childhood. Sevoflurane is a widely and popularly used inhalation anesthetic in children. It has been proposed that infant exposure to sevoflurane and isoflurane are associated with long-term loss of cognitive functions and neurobehavioral changes [55–57]. Autophagy is crucial for normal brain development since it is involved in nutritional supplementation during the prenatal period [58, 59]. Interfering with autophagy can disturb the proper coordination of cell growth, specialization, and programmed cell death that are required for developing the intricate structure of the nervous system [59]. This dysregulated autophagy was substantially studied in pregnant rats exposed to sevoflurane. It was determined inhalation of sevoflurane upregulated autophagy via the PTEN/Akt/mTOR pathway in fetus brains [58]. Further, phosphatase and tensin homolog on chromosome 10 (PTEN), is abundantly expressed in embryonic central nervous system and affects brain development. In mammalian cells, PTEN can modulate autophagy by counteracting PI3K via its lipid phosphatase function. Specifically, compared to the control group, the administration of sevoflurane resulted in a noteworthy increase of PTEN expression and a decrease in the levels of p-Akt/Akt and mTOR in fetal brains. This suggests the combined involvement of PTEN/Akt/mTOR signaling in activating autophagy in sevoflurane-induced neurotoxicity [58]. Broadly, these results suggest systemic effects following inhalation exposures could be mediated by variations in mTOR signaling.

Inhalation exposure modified mTOR signaling contributing to disease via lipid Metabolism and inflammation

mTOR, a primary regulator of cellular growth and development, also has key translational and/or transcriptional roles in inflammation with implications in atherosclerosis and other inflammatory diseases [60]. Pulmonary epithelial cells are primary target for exogenous irritants and act as a first line defense to protect against the inhaled particulates of air including pollutants, pathogens, allergens, etc. When exposed to foreign substances these epithelial cells not only restrict the systemic entry but also can activate the immune response [61]. mTOR

activity is an important intracellular regulator of leptin-induced macrophage lipid metabolism. Leptin, a hormone/cytokine secreted by adipocytes, modulates appetite control, and regulates energy metabolism via interactions with the hypothalamus. Interestingly leptin is directly involved in the formation of lipid droplets via activation of epithelial cells. Leptin directly exaggerates the production of inflammatory mediators such as leukotriene B₄ via activation of the mTOR pathway. Specifically, in macrophages, leptin activates PI3K/mTOR pathway, resulting in formation of lipid droplets, which are otherwise inhibited by rapamycin treatment (mTORC1 inhibitor). Lipid droplets are sites where lipid metabolism enzymes such prostaglandin-endoperoxide synthase 2 (PTGS2, also known as cyclooxygenase 2 or COX-2) involved in production of prostaglandins are located. Hence the formation of lipid droplets demonstrated increased expression of COX-2 and phospholipase A₂ protein expression suggesting of pro-inflammatory response [62]. Moreover, exposure to PM_{2.5} increases the adipose tissue macrophages which parallelly increases the visceral adipose tissue content and size, secreting more proinflammatory substances, causing inflammation [63]. Mechanistically, the findings confirm that increases in visceral fat causes dysregulation in PI3K/Akt/endothelial NO synthase signaling, causing inflammation and insulin resistance [27]. Overall, one could conclude, mTOR mediates metabolic syndrome and obesity-induced inflammation that is exaggerated by inhalation exposure.

Pulmonary outcomes

It is widely acknowledged that cigarette smoking is the primary contributor to the development of lung cancer due to the strong correlation between the quantity of cigarettes consumed and the likelihood of developing the disease. The main cause of COPD is the inhalation of chemicals and oxidants present in cigarette smoke (CS), in addition to being exposed to dust, industrial, or household particles [64, 65]. COPD is marked by a cumulative and complete blockage of the airways (known as chronic bronchitis), damage to the alveolar walls (emphysema), and excess mucus production [66]. Cysteine cathepsins are important in lung homeostasis and their dysregulation plays a key role in lung injury and inflammation via degrading antimicrobial peptides and extracellular matrix components. Murine experimental emphysema reported to have increased levels of cathepsin S, which is a potent elastase involved in alveolar remodeling [67–69]. Specifically, nicotine-containing cigarette smoke extract (CSE) upregulates cathepsin expression in human macrophages via mTOR pathway, modulating epithelial integrity and enhancing its permeability in COPD. This was confirmed when macrophages exposed to nicotine-containing CSE and nicotine alone demonstrated similar fold increase in cathepsin upregulation suggesting

nicotine to be driving factor of responses [64]. Furthermore, the signaling pathway was confirmed with treatment of rapamycin, a known mTOR inhibitor, which demonstrated increase in immunoreactive and mature cathepsin and decrease in phosphorylated transcription factor EB (TFEB), a central regulator of autophagy/lysosomal biogenesis [70]. Consequently, dysregulation of mTOR signaling contributes to CS-associated induction of pulmonary inflammation and disease.

Cancer

Prevalently, 90% of lungs cancer diagnosis is associated with the use of tobacco. Tobacco smoke contains numerous components including aromatic amines and polychromatic hydrocarbons that promote carcinogenesis. Additionally, these components, especially nicotine and nitrosamine 4-(methylnitrosamino)-1-(3-pyridyl)-1-butanone (NNK) produce active metabolites that promote DNA adduct formation. The carcinogenic effects of tobacco components involve activation of multiple signaling pathways that regulate cell cycle and proliferation. Of them, Akt/mTOR pathway is critically involved cell growth, metabolism, and survival. Abnormal and excessive mTOR activation promotes tumor growth, metastasis, and angiogenesis, a process that supplies carcinoma cells with oxygen and nutrients. Particularly, tobacco components damages DNA by activating Akt pathway and modulates PI3K, upstream regulator of Akt [71]. Experimentally, immunohistochemistry and immunoblotting on lung tissues of NNK-treated A/J mice reveals presence of phosphorylated Akt in airway epithelial cells and 5.5-fold increase in ratio of phosphorylated Akt to total Akt compared to phosphate buffered saline (PBS) control mice, respectively [72]. Similarly, *in vitro* studies on nicotine or NNK treated non-small cell lung cancer cells reports to increase phosphorylation of S6K1 and 4E-BP1, activate mTOR and induce cell proliferation [72, 73]. In short, tobacco smoke components foster cell proliferation and tumorigenesis via mTOR activation.

Conclusion

Inhalation exposure induces pulmonary and systemic effects contributing to the pathogenesis of various diseases. Inhaled

pollutants such as metal nanoparticles, exhaust fumes, cigarette smoke, and some anesthetics induce several detrimental cellular processes causing pathological outcomes. mTOR is involved in numerous cellular processes including cellular growth and metabolism. Given its importance in homeostasis, the dysregulation in mTOR signaling contributes to a variety of disease outcomes. mTOR is primarily regulated by PI3K/AKT signaling which can directly and/or indirectly be modified by many inhalation exposures resulting in autophagy, altered lipid metabolism, and inflammation. These cellular processes are known to contribute to multiple pulmonary and systemic diseases. Treatments focusing on reestablishing regulation of mTOR signaling could potentially be helpful in addressing inhalation exposure-induced diseases.

Author contributions

JS: Conceptualization, Funding acquisition, Project administration, Resources, Supervision, Writing-review and editing. AS: Formal analysis, Investigation, Methodology, Project administration, Visualization, Writing-original draft, Writing-review and editing, Conceptualization. All authors contributed to the article and approved the submitted version.

Funding

The authors declare that financial support was received for the research, authorship, and/or publication of this article. This work was funded by the National Institute of Environmental Health Sciences (NIEHS) Grant R01ES033173.

Acknowledgments

Figures created with [Biorender.com](https://biorender.com).

Conflict of interest

The authors declare that the research was conducted in the absence of any commercial or financial relationships that could be construed as a potential conflict of interest.

References

- Chen B, Kan H. Air pollution and population health: a global challenge. *Environ Health Prev Med* (2008) 13:94–101. doi:10.1007/s12199-007-0018-5
- Andreau K, Leroux M, Bouharrou A. Health and cellular impacts of air pollutants: from cytoprotection to cytotoxicity. *Biochem Res Int* (2012) 2012:1–18. doi:10.1155/2012/493894
- Levra S, Rosani U, Gnemmi I, Brun P, Leonardi A, Carriero V, et al. Impaired autophagy in the lower airways and lung parenchyma in stable COPD. *ERJ Open Res* (2023) 9(6):00423–2023. doi:10.1183/23120541.00423-2023
- Kobos L, Shannahan J. Particulate matter inhalation and the exacerbation of cardiopulmonary toxicity due to metabolic disease. *Exp Biol Med (Maywood)* (2021) 246(7):822–34. doi:10.1177/1535370220983275

5. Wang Y, Fung NSK, Lam WC, Lo ACY. mTOR signalling pathway: a potential therapeutic target for ocular neurodegenerative diseases. *Antioxidants (Basel)* (2022) **11**(7):1304. doi:10.3390/antiox11071304
6. Moore MN. Do airborne biogenic chemicals interact with the PI3K/Akt/mTOR cell signalling pathway to benefit human health and wellbeing in rural and coastal environments? *Environ Res* (2015) **140**:65–75. doi:10.1016/j.envres.2015.03.015
7. Battaglini S, Benjamin D, Wälchli M, Maier T, Hall MN. mTOR substrate phosphorylation in growth control. *Cell* (2022) **185**(11):1814–36. doi:10.1016/j.cell.2022.04.013
8. Yang M, Lu Y, Piao W, Jin H. The translational regulation in mTOR pathway. *Biomolecules* (2022) **12**(6):802. doi:10.3390/biom12060802
9. Tewari D, Patni P, Bishayee A, Sah AN, Bishayee A. Natural products targeting the PI3K-Akt-mTOR signaling pathway in cancer: a novel therapeutic strategy. *Semin Cancer Biol* (2022) **80**:1–17. doi:10.1016/j.semcancer.2019.12.008
10. Li T, Wang G. Computer-aided targeting of the PI3K/Akt/mTOR pathway: toxicity reduction and therapeutic opportunities. *Int J Mol Sci* (2014) **15**(10):18856–91. doi:10.3390/ijms151018856
11. Kim LC, Cook RS, Chen J. mTORC1 and mTORC2 in cancer and the tumor microenvironment. *Oncogene* (2017) **36**(16):2191–201. doi:10.1038/onc.2016.363
12. Saxton RA, Sabatini DM. mTOR signaling in growth, metabolism, and disease. *Cell* (2017) **169**(2):361–71. doi:10.1016/j.cell.2017.03.035
13. Dibble CC, Manning BD. Signal integration by mTORC1 coordinates nutrient input with biosynthetic output. *Nat Cell Biol* (2013) **15**(6):555–64. doi:10.1038/ncb2763
14. Szwed A, Kim E, Jacinto E. Regulation and metabolic functions of mTORC1 and mTORC2. *Physiol Rev* (2021) **101**(3):1371–426. doi:10.1152/physrev.00026.2020
15. Dibble CC, Cantley LC. Regulation of mTORC1 by PI3K signaling. *Trends Cell Biol* (2015) **25**(9):545–55. doi:10.1016/j.tcb.2015.06.002
16. Chen Z-H, Wu Y-F, Wang P-L, Wu Y-P, Li Z-Y, Zhao Y, et al. Autophagy is essential for ultrafine particle-induced inflammation and mucus hyperproduction in airway epithelium. *Autophagy* (2016) **12**(2):297–311. doi:10.1080/15548627.2015.1124224
17. Cadwell K. Crosstalk between autophagy and inflammatory signalling pathways: balancing defence and homeostasis. *Nat Rev Immunol* (2016) **16**(11):661–75. doi:10.1038/nri.2016.100
18. Zou Z, Tao T, Li H, Zhu X. mTOR signaling pathway and mTOR inhibitors in cancer: progress and challenges. *Cel Biosci* (2020) **10**(1):31–11. doi:10.1186/s13578-020-00396-1
19. Hua H, Kong Q, Zhang H, Wang J, Luo T, Jiang Y. Targeting mTOR for cancer therapy. *J Hematol Oncol* (2019) **12**(1):71–19. doi:10.1186/s13045-019-0754-1
20. Gremke N, Polo P, Dort A, Schneikert J, Elmshäuser S, Brehm C, et al. mTOR-mediated cancer drug resistance suppresses autophagy and generates a druggable metabolic vulnerability. *Nat Commun* (2020) **11**(1):4684. doi:10.1038/s41467-020-18504-7
21. Ballesteros-Álvarez J, Andersen JK. mTORC2: the other mTOR in autophagy regulation. *Aging Cell* (2021) **20**(8):e13431. doi:10.1111/ace1.13431
22. Rabanal-Ruiz Y, Otten EG, Korolchuk VI. mTORC1 as the main gateway to autophagy. *Essays Biochem* (2017) **61**(6):565–84. doi:10.1042/ebc20170027
23. Levine B, Kroemer G. Autophagy in the pathogenesis of disease. *Cell* (2008) **132**(1):27–42. doi:10.1016/j.cell.2007.12.018
24. Lakhdar R, Mumby S, Abubakar-Waziri H, Porter A, Adcock IM, Chung KF. Lung toxicity of particulate and gaseous pollutants using *ex-vivo* airway epithelial cell culture systems. *Environ Pollut* (2022) **183**:119323. doi:10.1016/j.envpol.2022.119323
25. Jeong SY, Kim J, Park EK, Baek M-C, Bae J-S. Inhibitory functions of maslinic acid on particulate matter-induced lung injury through TLR4-mTOR-autophagy pathways. *Environ Res* (2020) **183**:109230. doi:10.1016/j.envres.2020.109230
26. Woodward NC, Levine MC, Haghani A, Shirmohammadi F, Saffari A, Sioutas C, et al. Toll-like receptor 4 in glial inflammatory responses to air pollution *in vitro* and *in vivo*. *J neuroinflammation* (2017) **14**:84–15. doi:10.1186/s12974-017-0858-x
27. Sun Q, Yue P, Deilulis JA, Lumeng CN, Kampfrath T, Mikolaj MB, et al. Ambient air pollution exaggerates adipose inflammation and insulin resistance in a mouse model of diet-induced obesity. *Circulation* (2009) **119**(4):538–46. doi:10.1161/circulationaha.108.799015
28. Jung HS, Chung KW, Won Kim J, Kim J, Komatsu M, Tanaka K, et al. Loss of autophagy diminishes pancreatic β cell mass and function with resultant hyperglycemia. *Cel Metab* (2008) **8**(4):318–24. doi:10.1016/j.cmet.2008.08.013
29. Ebato C, Uchida T, Arakawa M, Komatsu M, Ueno T, Komiya K, et al. Autophagy is important in islet homeostasis and compensatory increase of beta cell mass in response to high-fat diet. *Cel Metab* (2008) **8**(4):325–32. doi:10.1016/j.cmet.2008.08.009
30. Guillén C, Benito M. mTORC1 overactivation as a key aging factor in the progression to type 2 diabetes mellitus. *Front Endocrinol* (2018) **9**:621. doi:10.3389/fendo.2018.00621
31. Ong PS, Wang LZ, Dai X, Tseng SH, Loo SJ, Sethi G. Judicious toggling of mTOR activity to combat insulin resistance and cancer: current evidence and perspectives. *Front Pharmacol* (2016) **7**:395. doi:10.3389/fphar.2016.00395
32. Gual P, Le Marchand-Brustel Y, Tanti J. Positive and negative regulation of glucose uptake by hyperosmotic stress. *Diabetes Metab* (2003) **29**(6):566–75. doi:10.1016/s1262-3636(07)70071-x
33. Tanti J-F, Jager J. Cellular mechanisms of insulin resistance: role of stress-regulated serine kinases and insulin receptor substrates (IRS) serine phosphorylation. *Curr Opin Pharmacol* (2009) **9**(6):753–62. doi:10.1016/j.coph.2009.07.004
34. Um SH, Frigerio F, Watanabe M, Picard F, Joaquin M, Sticker M, et al. Absence of S6K1 protects against age- and diet-induced obesity while enhancing insulin sensitivity. *Nature* (2004) **431**(7005):200–5. doi:10.1038/nature02866
35. Stebounova LV, Adamcakova-Dodd A, Kim JS, Park H, O'Shaughnessy PT, Grassian VH, et al. Nanosilver induces minimal lung toxicity or inflammation in a subacute murine inhalation model. *Part Fibre Toxicol* (2011) **8**(1):5. doi:10.1186/1743-8977-8-5
36. Card JW, Zeldin DC, Bonner JC, Nestmann ER. Pulmonary applications and toxicity of engineered nanoparticles. *Am J Physiology-Lung Cell Mol Physiol* (2008) **295**(3):L400–11. doi:10.1152/ajplung.00041.2008
37. Yuan J, Mo Y, Zhang Y, Zhang Q. Nickel nanoparticles induce autophagy and apoptosis via HIF-1 α /mTOR signaling in human bronchial epithelial cells. *Environ Pollut* (2023) **329**:121670. doi:10.1016/j.envpol.2023.121670
38. Liu Z, Lv X, Xu L, Liu X, Zhu X, Song E, et al. Zinc oxide nanoparticles effectively regulate autophagic cell death by activating autophagosome formation and interfering with their maturation. *Part fibre Toxicol* (2020) **17**(1):46–17. doi:10.1186/s12989-020-00379-7
39. Stern ST, Adiseshaiah PP, Crist RM. Autophagy and lysosomal dysfunction as emerging mechanisms of nanomaterial toxicity. *Part fibre Toxicol* (2012) **9**:20–17. doi:10.1186/1743-8977-9-20
40. Xiao J, Tu B, Zhou X, Jiang X, Xu G, Zhang J, et al. Autophagy deficiency exacerbates acute lung injury induced by copper oxide nanoparticles. *J Nanobiotechnology* (2021) **19**(1):162–18. doi:10.1186/s12951-021-00909-1
41. Yu Y, Duan J, Yu Y, Li Y, Liu X, Zhou X, et al. Silica nanoparticles induce autophagy and autophagic cell death in HepG2 cells triggered by reactive oxygen species. *J Hazard Mater* (2014) **270**:176–86. doi:10.1016/j.jhazmat.2014.01.028
42. Chou C-C, Chen W, Hung Y, Mou C-Y. Molecular elucidation of biological response to mesoporous silica nanoparticles *in vitro* and *in vivo*. *ACS Appl Mater Inter* (2017) **9**(27):22235–51. doi:10.1021/acsami.7b05359
43. Liu H, Cheng Y, Yang J, Wang W, Fang S, Zhang W, et al. BBC3 in macrophages promoted pulmonary fibrosis development through inducing autophagy during silicosis. *Cel Death Dis* (2017) **8**(3):e2657–e. doi:10.1038/cddis.2017.78
44. Pizzino G, Irrera N, Cucinotta M, Pallio G, Mannino F, Arcoraci V, et al. Oxidative stress: harms and benefits for human health. *Oxidative Med Cell Longevity* (2017) **2017**:1–13. doi:10.1155/2017/8416763
45. Wang X, Sun J, Xu T, Lei Y, Gao M, Lin H. Resveratrol alleviates imidacloprid-induced mitochondrial apoptosis, necroptosis, and immune dysfunction in chicken lymphocyte lines by inhibiting the ROS/MAPK signaling pathway. *Environ Toxicol* (2024) **39**:2052–63. doi:10.1002/tox.24097
46. Calderón-Garcidueñas L, Reynoso-Robles R, González-Macié A. Combustion and friction-derived nanoparticles and industrial-sourced nanoparticles: the culprit of Alzheimer and Parkinson's diseases. *Environ Res* (2019) **176**:108574. doi:10.1016/j.envres.2019.108574
47. Hodges SL, Reynolds CD, Smith GD, Jefferson TS, Nolan SO, Lugo JN. Molecular interplay between hyperactive mammalian target of rapamycin signaling and Alzheimer's disease neuropathology in the NS-Pten knockout mouse model. *Neuroreport* (2018) **29**(13):1109–13. doi:10.1097/wnr.0000000000001081
48. Norwitz NG, Querfurth H. mTOR mysteries: nuances and questions about the mechanistic target of rapamycin in neurodegeneration. *Front Neurosci* (2020) **14**:775. doi:10.3389/fnins.2020.00775
49. Toral-Rios D, Pichardo-Rojas PS, Alonso-Vanegas M, Campos-Peña V. GSK3 β and tau protein in alzheimer's disease and epilepsy. *Front Cell Neurosci* (2020) **14**:19. doi:10.3389/fncel.2020.00019

50. Mueed Z, Tandon P, Maurya SK, Deval R, Kamal MA, Poddar NK. Tau and mTOR: the hotspots for multifarious diseases in Alzheimer's development. *Front Neurosci* (2018) **12**:1017. doi:10.3389/fnins.2018.01017
51. Chen J, Long Z, Li Y, Luo M, Luo S, He G. Alteration of the Wnt/GSK3 β / β -catenin signalling pathway by rapamycin ameliorates pathology in an Alzheimer's disease model. *Int J Mol Med* (2019) **44**(1):313–23. doi:10.3892/ijmm.2019.4198
52. Caccamo A, Magri A, Medina DX, Wisely EV, López-Aranda MF, Silva AJ, et al. mTOR regulates tau phosphorylation and degradation: implications for Alzheimer's disease and other tauopathies. *Aging cell* (2013) **12**(3):370–80. doi:10.1111/acer.12057
53. Pollard RJ, Hopkins T, Smith CT, May BV, Doyle J, Chambers CL, et al. Perianesthetic and anesthesia-related mortality in a southeastern United States population: a longitudinal review of a prospectively collected quality assurance data base. *Anesth Analgesia* (2018) **127**(3):730–5. doi:10.1213/ane.0000000000003483
54. Machado-Junior PA, de Souza ABF, Castro Td F, Perucci LO, Talvani A, Cangussú SD, et al. The deleterious impact of exposure to different inhaled anesthetics is time dependent. *Life Sci* (2022) **309**:121004. doi:10.1016/j.lfs.2022.121004
55. Liang L, Fan Z, He D, Zhao Y, Zeng T, Liu B, et al. Sevoflurane-induced neurotoxicity in the developing Hippocampus via HIPK2/AKT/mTOR signaling. *Neurotox Res* (2022) **40**(3):803–13. doi:10.1007/s12640-021-00445-8
56. Glatz P, Sandin RH, Pedersen NL, Bonamy A-K, Eriksson LI, Granath F. Association of anesthesia and surgery during childhood with long-term academic performance. *JAMA Pediatr* (2017) **171**(1):e163470–e. doi:10.1001/jamapediatrics.2016.3470
57. Sun L. Early childhood general anaesthesia exposure and neurocognitive development. *Br J Anaesth* (2010) **105**:i61–i68. doi:10.1093/bja/aeq302
58. Li X, Wu Z, Zhang Y, Xu Y, Han G, Zhao P. Activation of autophagy contributes to sevoflurane-induced neurotoxicity in fetal rats. *Front Mol Neurosci* (2017) **10**:432. doi:10.3389/fnmol.2017.00432
59. Boya P, Mellén MA, de la Rosa E. How autophagy is related to programmed cell death during the development of the nervous system. *Biochem Soc Trans* (2008) **36**(Pt 5):813–7. doi:10.1042/bst0360813
60. Maya-Monteiro CM, Bozza PT. Leptin and mTOR: partners in metabolism and inflammation. *Cell Cycle* (2008) **7**(12):1713–7. doi:10.4161/cc.7.12.6157
61. Li ZY, Wu YF, Xu XC, Zhou JS, Wang Y, Shen HH, et al. Autophagy as a double-edged sword in pulmonary epithelial injury: a review and perspective. *Am J Physiology-Lung Cell Mol Physiol* (2017) **313**(2):L207–L217. doi:10.1152/ajplung.00562.2016
62. Fazolini NP, Cruz AL, Werneck MB, Viola JP, Maya-Monteiro CM, Bozza PT. Leptin activation of mTOR pathway in intestinal epithelial cell triggers lipid droplet formation, cytokine production and increased cell proliferation. *Cell Cycle* (2015) **14**(16):2667–76. doi:10.1080/15384101.2015.1041684
63. Xu X, Yavar Z, Verdin M, Ying Z, Mihai G, Kampfrath T, et al. Effect of early particulate air pollution exposure on obesity in mice: role of p47phox. *Arteriosclerosis, Thromb Vasc Biol* (2010) **30**(12):2518–27. doi:10.1161/atvbaha.110.215350
64. Bigot P, Chesserion S, Saidi A, Sizaret D, Parent C, Petit-Courty A, et al. Cleavage of occludin by cigarette smoke-elicited cathepsin S increases permeability of lung epithelial cells. *Antioxidants (Basel)* (2022) **12**(1):5. doi:10.3390/antiox12010005
65. Murray CJ, Lopez AD. Evidence-based health policy—lessons from the global burden of disease study. *Science* (1996) **274**(5288):740–3. doi:10.1126/science.274.5288.740
66. Barnes PJ. Targeting cytokines to treat asthma and chronic obstructive pulmonary disease. *Nat Rev Immunol* (2018) **18**(7):454–66. doi:10.1038/s41577-018-0006-6
67. Wilkinson RD, Williams R, Scott CJ, Burden RE. Cathepsin S: therapeutic, diagnostic, and prognostic potential. *Biol Chem* (2015) **396**(8):867–82. doi:10.1515/hsz-2015-0114
68. Wang Z, Zheng T, Zhu Z, Homer RJ, Riese RJ, Chapman HA, et al. Interferon γ induction of pulmonary emphysema in the adult murine lung. *J Exp Med* (2000) **192**(11):1587–600. doi:10.1084/jem.192.11.1587
69. Zheng T, Zhu Z, Wang Z, Homer RJ, Ma B, Riese RJ, et al. Inducible targeting of IL-13 to the adult lung causes matrix metalloproteinase- and cathepsin-dependent emphysema. *J Clin Invest* (2000) **106**(9):1081–93. doi:10.1172/jci10458
70. Tan A, Prasad R, Lee C, Jho E-H. Past, present, and future perspectives of transcription factor EB (TFEB): mechanisms of regulation and association with disease. *Cel Death Differ* (2022) **29**(8):1433–49. doi:10.1038/s41418-022-01028-6
71. Memmott RM, Dennis PA. The role of the akt/mTOR pathway in tobacco carcinogen-induced lung tumorigenesis. *Clin Cancer Res* (2010) **16**(1):4–10. doi:10.1158/1078-0432.ccr-09-0234
72. West KA, Brognard J, Clark AS, Linnoila IR, Yang X, Swain SM, et al. Rapid Akt activation by nicotine and a tobacco carcinogen modulates the phenotype of normal human airway epithelial cells. *J Clin Invest* (2003) **111**(1):81–90. doi:10.1172/jci200316147
73. Tsurutani J, Castillo SS, Brognard J, Granville CA, Zhang C, Gills JJ, et al. Tobacco components stimulate Akt-dependent proliferation and NF κ B-dependent survival in lung cancer cells. *Carcinogenesis* (2005) **26**(7):1182–95. doi:10.1093/carcin/bgi072



OPEN ACCESS

*CORRESPONDENCE

Liang-An Chen,
✉ chenliangan301@163.com
Chun-Sun Li,
✉ sun082000@163.com

[†]These authors have contributed equally to this work

RECEIVED 15 January 2024

ACCEPTED 05 April 2024

PUBLISHED 19 April 2024

CITATION

Su C-C, Zhang Z-R, Liu J-X, Meng J-G, Ma X-Q, Mo Z-F, Ren J-B, Liang Z-X, Yang Z, Li C-S and Chen L-A (2024), Vaporization of perfluorocarbon attenuates sea-water-drowning-induced acute lung injury by deactivating the NLRP3 inflammasomes in canines.

Exp. Biol. Med. 249:10104.

doi: 10.3389/ebm.2024.10104

COPYRIGHT

© 2024 Su, Zhang, Liu, Meng, Ma, Mo, Ren, Liang, Yang, Li and Chen. This is an open-access article distributed under the terms of the [Creative Commons Attribution License \(CC BY\)](https://creativecommons.org/licenses/by/4.0/). The use, distribution or reproduction in other forums is permitted, provided the original author(s) and the copyright owner(s) are credited and that the original publication in this journal is cited, in accordance with accepted academic practice. No use, distribution or reproduction is permitted which does not comply with these terms.

Vaporization of perfluorocarbon attenuates sea-water-drowning-induced acute lung injury by deactivating the NLRP3 inflammasomes in canines

Cheng-Cheng Su^{1,2,3†}, Zhao-Rui Zhang^{2†}, Jin-Xia Liu^{1,2}, Ji-Guang Meng², Xiu-Qing Ma², Zhen-Fei Mo^{1,2}, Jia-Bo Ren^{1,2}, Zhi-Xin Liang², Zhen Yang², Chun-Sun Li^{2*} and Liang-An Chen^{2*}

¹Medical School of Chinese PLA, Beijing, China, ²Department of Respiration, The Eight Medical Center of Chinese PLA General Hospital, Beijing, China, ³Department of Critical Care and Respiration, Characteristic Medical Center of Chinese People's Armed Police Force, Tianjin, China

Abstract

Seawater-drowning-induced acute lung injury (SD-ALI) is a life-threatening disorder characterized by increased alveolar–capillary permeability, an excessive inflammatory response, and refractory hypoxemia. Perfluorocarbons (PFCs) are biocompatible compounds that are chemically and biologically inert and lack toxicity as oxygen carriers, which could reduce lung injury *in vitro* and *in vivo*. The aim of our study was to explore whether the vaporization of PFCs could reduce the severity of SD-ALI in canines and investigate the underlying mechanisms. Eighteen beagle dogs were randomly divided into three groups: the seawater drowning (SW), perfluorocarbon (PFC), and control groups. The dogs in the SW group were intratracheally administered seawater to establish the animal model. The dogs in the PFC group were treated with vaporized PFCs. Probe-based confocal laser endomicroscopy (pCLE) was performed at 3 h. The blood gas, volume air index (VAI), pathological changes, and wet-to-dry (W/D) lung tissue ratios were assessed. The expression of heme oxygenase-1 (HO-1), nuclear respiratory factor-1 (NRF1), and NOD-like receptor family pyrin domain containing-3 (NLRP3) inflammasomes was determined by means of quantitative real-time polymerase chain reaction (qRT-PCR) and immunological histological chemistry. The SW group showed higher lung injury scores and W/D ratios, and lower VAI compared to the control group, and treatment with PFCs could reverse the change of lung injury score, W/D ratio and VAI. PFCs deactivated NLRP3 inflammasomes and reduced the release of caspase-1, interleukin-1β

(IL-1 β), and interleukin-18 (IL-18) by enhancing the expression of HO-1 and NRF1. Our results suggest that the vaporization of PFCs could attenuate SD-ALI by deactivating NLRP3 inflammasomes via the HO-1/NRF1 pathway.

KEYWORDS

perfluorocarbons, acute lung injury, probe-based confocal laser endomicroscopy, heme oxygenase-1, nuclear respiratory factor-1

Impact statement

The study offered the first pCLE image description and quantitative analysis of acute lung injury induced by seawater drowning, and demonstrated that inhalation of vaporized PFCs suppressed seawater-drowning-induced acute lung injuries. The mechanisms of PFCs' therapeutic effects may be attributed to the regulation of NLRP3 inflammasomes' activation via the HO-1/NRF1 pathway. This study offers a meaningful exploration of PFCs' therapeutic mechanisms *in vivo*.

Highlights

- We observed that PFCs can attenuate seawater-drowning-induced acute lung injury.
- In this study, we proved that probe-based confocal laser endomicroscopy is a noninvasive examination to evaluate acute lung injury realtimely.
- Regulation of NLRP3 inflammasomes is a new promising target for seawater-drowning-induced acute lung injury.
- HO-1/NRF1 pathway connects with NLRP3 activation.

Introduction

Seawater drowning is a major cause of morbidity and mortality worldwide. According to the World Health Organization, drowning accounted for an estimated 372,000 deaths in 2012 [1]. Seawater-drowning-induced lung injury (SD-ALI)/acute respiratory distress syndrome (SD-ARDS) is one of the most important complications in drowning patients, with a high fatality rate but few therapies [2, 3]. The main treatment for drowning is supportive care, including pulmonary support to avoid complications. Previous studies have suggested that treatments including dexamethasone, tanshinone II A and 1 α , and 25-dihydroxyvitamin D3 might be effective at alleviating SD-ALI [4–7]. However, we still lack an effective therapy for this life-threatening disorder. ALI/ARDS are often regarded as one entity with similar pathobiology of lung injuries, clinical manifestations, and specific targets of drug intervention, despite induced by different injuries and conditions. The category “acute lung injury”, the previous definition expressed the milder form of ARDS, was omitted from the Berlin definition. It is generally considered that this

term is the description of the situation where the clinical definition criteria cannot be fulfilled as well as experimental study [8]. According to current research, SD-ALI is generally recognized as a complex injury process involving an insufficiency of oxygen and pulmonary surfactant, blood–air barrier disruption, the formation of pulmonary oedema, inflammation, oxidative stress, autophagy, apoptosis, and so on, but its exact mechanisms and potential treatments require further exploration [9].

Perfluorocarbons (PFCs) are colorless and odorless molecular liquids composed of carbon and fluorine with features such as a high level of gas dissolvability in water, rapid release, low surface pressure, high volume, average volatility, favorable histo-compatibility, and no absorption or metabolism *in vivo* [7, 10–12]. Partial liquid ventilation with perfluorocarbons improves the gas exchange, breathing mechanism, and lung structure in many acute lung injury models [13–16]. Our previous studies showed that blast lung injuries could be attenuated by the vaporization of PFCs via the nuclear factor (NF)- κ B pathway *in vivo* and *in vitro* [17, 18]. However, the influence of PFCs on SD-ALI in canines has not been reported.

Probe-based confocal laser endomicroscopy (pCLE) is a minimally invasive technique that allows for the *in vivo* microscopic imaging of living tissue through a 1 mm flexible fiber optic mini probe [19]. Recent studies showed that pCLE has the potential to serve as an *in vivo* bronchoscopic imaging technique in the assessment of lung injury [20]. Our study aimed to explore whether PFCs could reduce the severity of SD-ALI and investigate the underlying molecular mechanisms.

Materials and methods

Chemicals and reagents

The experimental seawater was prepared according to the formula provided by the Third Institute of Oceanography, Ministry of Natural Resources, Fujian, China. The main components of the seawater were close to those of the southeast coastal seawater of China: pH, 8.2; specific gravity, 1.05; and osmotic pressure, 1,300 mmol/L; NaCl 26.518 g/L, MgCl₂ 2.447 g/L, MgSO₄ 3.305 g/L, CaCl₂ 1.141 g/L, KCl 0.725 g/L, NaHCO₃ 0.202 g/L, NaBr 0.725 g/L [21].

Animal experiment and modeling

Eighteen male specified pathogen-free beagle dogs (12–18 months old, weighing 13.02 ± 0.66 kg) were obtained from the Laboratory Animal Center of the PLA General hospital. Dogs were housed under a 12 h light/dark cycle in a room with a controlled temperature (23°C) and humidity (50%). All experiments were performed in compliance with the Experimental Animal Care Committee of the PLA General hospital (SQ2022447) and the ARRIVE 2.0 guidelines [22].

We randomly divided the 18 beagle dogs into 3 groups: the control, seawater-induced acute lung injury (SW), and PFC groups. Anesthesia was induced via intraperitoneal (I.P.) injection of pentobarbital (25–30 mg/kg), which was deemed adequate according to the blink test throughout the experiment. Following 15 min of stabilization, the dogs in the control group were subjected to tracheal intubation without seawater instillation and treated with a ventilator (DRAGER, Savina 300) according to the following parameters: 30% inspired oxygen (FiO_2), 8 mL/kg tidal volume (VT), 4 cmH₂O positive end-expiratory pressure (PEEP), and 16 counts/min. The dogs in the SW groups were subjected to tracheal intubation and instilled with pre-cooled seawater (8 mL/kg) through a tracheal cannula within 1 min. The dogs were maintained in a supine position with heads elevated at 30° for monitoring. The appearance of dyspnea and frothy sputum, as well as a sharp drop in the oxygen saturation to 45–65%, demonstrated the successful modeling of SD-ALI. After resuscitation, the dogs were treated with a ventilator according to the same parameters as the control group. The dogs in the PFC groups were subjected to tracheal intubation and instilled with pre-cooled seawater (8 mL/kg), as described above in the SW group; then, they were ventilated with the same parameters, and vaporized PFCs (10 mL/kg) (C8F18; Huajieshi Medical Company, Shanghai, China) were administered continuously for 1.5 h at 0 h and 3 h after modeling via mechanical ventilation.

Blood gas analysis

Arterial blood was collected from the femoral artery of the dogs using a blood gas needle after 0 h, 3 h, and 6 h of modeling. Then, blood gas was analyzed immediately using an automated blood gas analyzer (ABL 800, Radiometer, Copenhagen, Denmark).

Probe-based confocal laser endomicroscopy

PCLE was performed with a 1.4 mm semi-flexible confocal probe (Cellvizio, Mauna Kea Technologies, Paris, France), which can pass through a portable bronchoscope. A 1 mL volume of 1%

sodium fluorescein was intravenously administered to obtain clear images 1 min before pCLE. We inserted the probe via the endotracheal route under bronchoscope control into a proximal segmental bronchiole of the left lobe, as described previously, and recorded the video sequences at least for at least 30 s using imaging software (Image cell 3.6.2; Mauna Kea Technologies, Paris, France). The volume air index (VAI) was calculated as described previously [23]. Briefly, images at end-expiration were selected for analysis and exported as single frames. Then, we developed a batch image processing method for NI Vision Assistant 8.2.1 (National Instruments, Austin, TX, United States) and obtained a histogram including the grey value distribution that could be analyzed and transferred to an Excel sheet (Microsoft Excel, 2003). Then, we calculated the mean grey value (M) and standard deviation (SD) to define the integration limits, defining $M-SD$ as the lower limit and M as the upper limit. The pixels between the lower and upper integration limits represented air-filled structures in the predefined slice. The VAI equaled the number of counted pixels divided by their total number, which represented the air content of several binary layers.

Sample collection

Blood and tissue samples from the lower right lung were harvested for subsequent measurements. We cut the left lung of the dogs and injected it with 20 mL pre-cooled normal saline. Then, we collected the bronchoalveolar lavage fluid (BALF) by gently washing the right lung. The lavage was repeated 3 times, and the retrieval rate was over 70%. The supernatants of the BALF were collected by centrifugation at 1,000 rpm for 5 min. The cells were resuspended in saline and smeared on glass slide for hematoxylin and eosin (H&E) staining and cell counting as described previously [24]. The three different sites in the anterior lobe, middle lobe, and posterior lobe of the right lung were fixed in 4% paraformaldehyde at room temperature, embedded in paraffin, sectioned serially at 5 μm , and stained with H&E for immunofluorescence and immunohistochemistry analyses. The peripheral venous blood was collected with a blood collection tube containing ethylene diamine tetraacetic acid (EDTA).

Measurement of lung wet-to-dry weight (W/D) ratio

To determine the severity of lung edema and water accumulation, we measured the W/D ratios. The middle lobe of the right lung was weighed immediately after sampling, and then the tissues were dried at 65°C until the weight was stabilized. The lung tissue W/D ratios were calculated as wet weight divided by dry weight.

H&E staining

Lung tissue sections were stained for histological analysis with a H&E staining kit. Finally, the slides were scanned using a Nano-Zoomer S60 system (Hamamatsu Photonics, Hamamatsu City, Japan). All sections were reviewed and analyzed by two pathologists independently in a blinded manner. The scoring strategy followed a previously described method [25]. Briefly, two pathologists who were blind to the treatment of the animals examined all tissue sections (3 sections from each animal) and evaluated the hyaline membrane, interstitial edema, intra-alveolar hemorrhage, intra-alveolar edema, and neutrophil accumulation levels. These characteristics were subjectively scored from 0 to 3: 0 = normal, 1 = slight effect, 2 = moderate presence of the feature, and 3 = severe effect.

Transmission electron microscopy (TEM)

Lung tissue samples with the size of millets were fixed in 4% glutaraldehyde at 4°C for 24 h and post-fixed in 1% osmic acid for 2 h. After dehydration with a gradient of ethanol and acetone, the samples were embedded in an epoxy resin. Finally, ultrathin sections were stained with 2% uranylacetate and lead citrate and observed using transmission electron microscopy (HT7800, Hitachi, Tokyo, Japan).

Immunological histological chemistry

Lung tissue sections were incubated in 3% H₂O₂ to block endogenous peroxidase and placed in blocking buffer (C220702, Yangguangbio, Beijing, China) for 15 min, followed by staining using rabbit polyclonal primary antibodies for NOD-like receptor family pyrin domain containing 3 (NLRP3) (1:500; bs-10021R, Bioss, Beijing, China), nuclear respiratory factor-1 (NRF1) polyclonal antibodies (1:1000; MBS3204137, Mybiosource, San Diego, CA, United States) and heme oxygenase-1 (HO-1) antibodies (1:500; GTX13248, Genetex, San Antonio, TX, United States) overnight at 4°C. Then, the sections were washed three times in PBS and incubated with horseradish peroxidase (HRP)-conjugated goat anti-rabbit IgG (H+L) (GB23303, Solarbio, Wuhan, Hubei, China) and HRP-conjugated goat anti-mouse IgG (H+L) (GB23301, Solarbio, Wuhan, Hubei, China). The slides were incubated in DAB (AR1022, Bosterbio, Wuhan, Hubei, China), counterstained in Mayer's hematoxylin solution, dehydrated, cleared in xylene, and placed in Depex mounting medium. Finally, the slides were scanned using a Nano-Zoomer S60 system.

Immunofluorescence

Lung tissue sections were placed in blocking buffer for 15 min followed by staining using rabbit polyclonal antibodies for E-cadherin polyclonal antibodies (1:300; 20874-1-AP, protein-tech, Wuhan, Hubei, China) overnight at 4°C. Then, the sections were washed 3 times in PBS and incubated in goat anti-rabbit IgG/RBITC (SR134, Solarbio, Wuhan, Hubei, China), followed by washing 3 times in PBS and incubation in anti-fade medium containing 4',6-diamidino-2'-phenylindole (DAPI). Finally, the slides were scanned using a Nano-Zoomer S60 system.

Enzyme-linked immunosorbent assay (ELISA)

The BALF supernatant obtained using the method described in *Sample collection* section was centrifuged at 8,000 g for 20 min, and we detected the levels of pulmonary surfactant A (SP-A) and pulmonary surfactant B (SP-B) with ELISA kits (Shanghai Enzyme-linked Biotechnology company, Shanghai, China) according to the manufacturer's protocol.

Quantitative real-time PCR (qRT-PCR) analysis

Using TRIzol™ reagent (15596026, Invitrogen, Carlsbad, CA, United States), total RNA was extracted from lung tissues. Then, we obtained the cDNA using a reagent kit (9767, TaKaRaBio, Dalian, Liaoning, China). QRT-PCR was carried out using a KAPA SYBR® FAST qPCR Master Mix kit (KK4601, R&D, Cape Town, South Africa) with the amplification conditions set as follows: 94°C for 30 s, followed by 40 cycles at 94°C for 5 s and 60°C for 34 s. Three technical replicates were performed for each cDNA sample. The β-actin gene was employed as the internal control. The primer sequences for the target genes are listed in [Table 1](#).

Statistical analysis

Statistical analysis was performed using GraphPad Prism 6 software (GraphPad Software Inc., La Jolla, CA, United States). Data are presented as mean ± standard error of mean (SEM), and one-way analysis of variance followed by Tukey's test was used for comparisons. *p* < 0.05 was considered to indicate a statistically significant difference.

TABLE 1 Primer sequences used in this study.

Primers	Sequences (5'-3')	PCR products (bp)
NRF1	CACCAATGGGAGCAATTTT	141
	ACACCCAGGTCCCTTTCTCT	
HO-1	CTTCTTCACCTTCCCAACA	138
	ATGTTTACAGCAGGAAGGCAGT	
NLRP3	GTGTTATGTGGCCTGGACT	119
	TGGTGCTTCTGGGTCTCTCT	
caspase-1	GCCTCAACCTCAAGGACAAA	101
	TGTCGAGGCTTTTGGAGAGT	
IL-1 β	CAAGAAACCTCCTTTGTGC	142
	ACAAGTGGGCTTTTTCATGG	
IL-18	ACGAGGGAAATCAACCTGTATT	113
	CAGACCTCTAGTGAGGCTATCT D	
β -actin	TGCGTGACATCAAGGAGAAG	175
	AGGAAGGAAGGCTGGAAGAG	

Abbreviations used are follows: NRF1, nuclear respiratory factor-1; HO-1, heme oxygenase-1; NLRP3, NOD-like-receptor family pyrin domain-containing-3; IL-1 β , interleukin-1 β ; IL-18, interleukin-18.

Results

Blood gas analysis

Compared with the control group, the pH value and oxygen index were significantly decreased and the PaCO₂ significantly increased in the SW group ($p < 0.05$). The blood gas analysis for the PFC group showed a significantly increased PaO₂ and pH value and decreased oxygen index ($p < 0.05$) (Figures 1A–C).

PCLE helped to assess lung injury in a noninvasive and real-time manner

Images in the control group showed the fiber-like structures represented normal alveolar tissue, while the dark background represented the gas in the lung. However, the pictures from the SW group showed much thicker fiber-like structures and more fiber-like structures representing the thickening and disorder of alveolar structures, while the background became much thicker, representing the gas-trapping, liquid leakage and inflammatory infiltration. However, images from the PFC group showed alleviation of the above-mentioned manifestations (Figure 1D).

Then, image sequences of at least six differing alveolar clusters of each group were selected for the calculation of the VAI. As depicted in Figure 1E significant difference

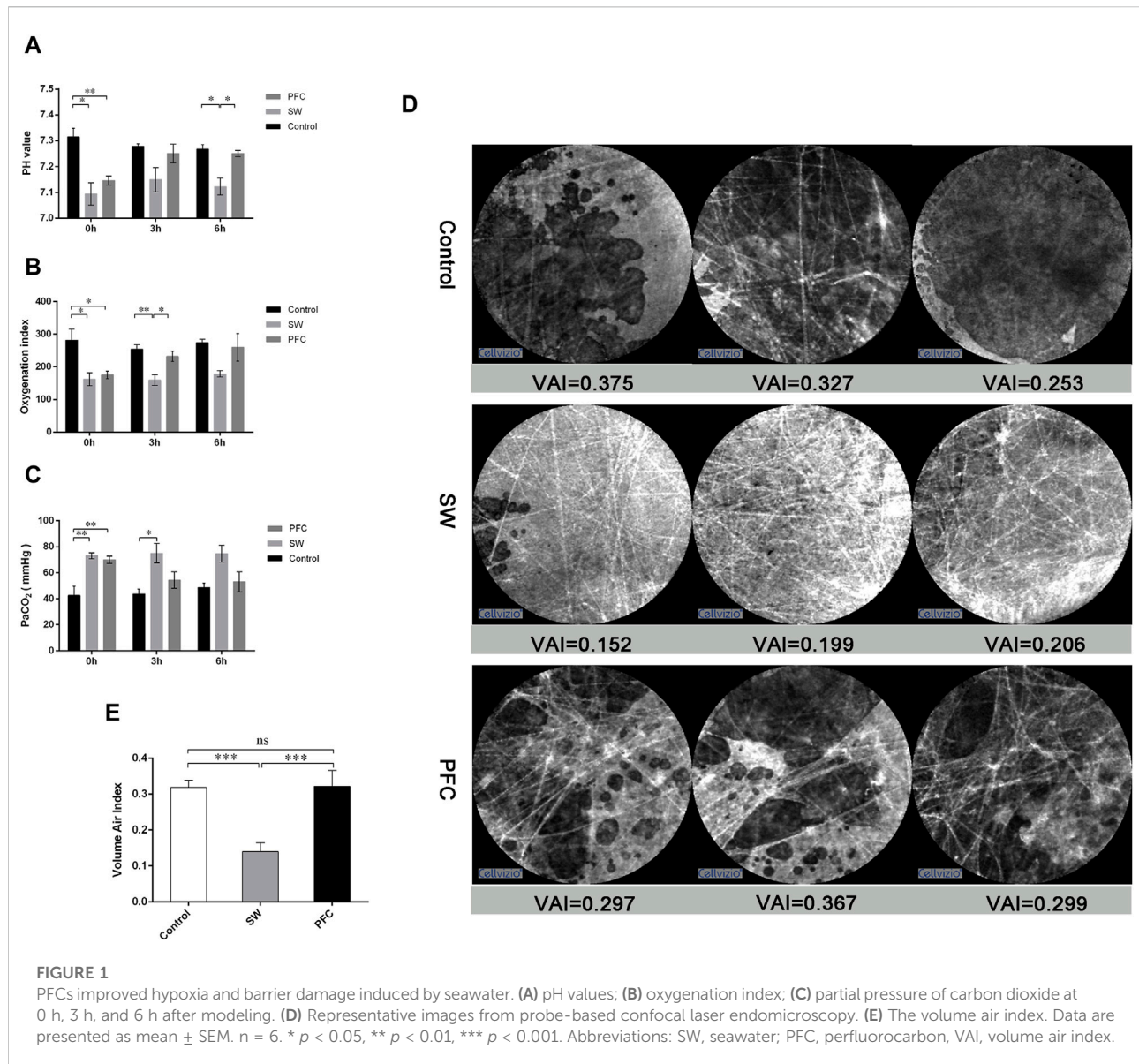
between the control group and the SW group was observed ($p < 0.05$), and PFC administration could significantly upregulate VAI compared with the SW group.

Pathological changes

The pathological assessment of the SW group (Figure 2A) exhibited alveolar destruction, edema, hemorrhages, the extensive infiltration of inflammatory cells, and alveolar collapse (Figure 2B), and the lung injury scores (Figure 2D) were significantly increased compared to those for the control group. In the PFC group, the lung injuries, including alveolar destruction, edema, and hemorrhages, were alleviated (Figure 2C), and the lung injury scores were significantly reduced (Figure 2D) compared with those for the SW group.

Additionally, we performed total cell counting and differential cell counting using the H&E staining of BALF cells. Compared with the control group, the SW group exhibited a significantly elevated total cell count and higher macrophage, neutrophil and lymphocyte counts, while PFC inhalation effectively reversed the infiltration of total cells, neutrophils and lymphocytes induced by seawater ($p < 0.05$) (Figures 2F–I).

Then, we used the W/D ratios to evaluate the severity of the lung edema. The W/D ratios of the SW group were significantly increased compared with the control group ($p < 0.001$), while



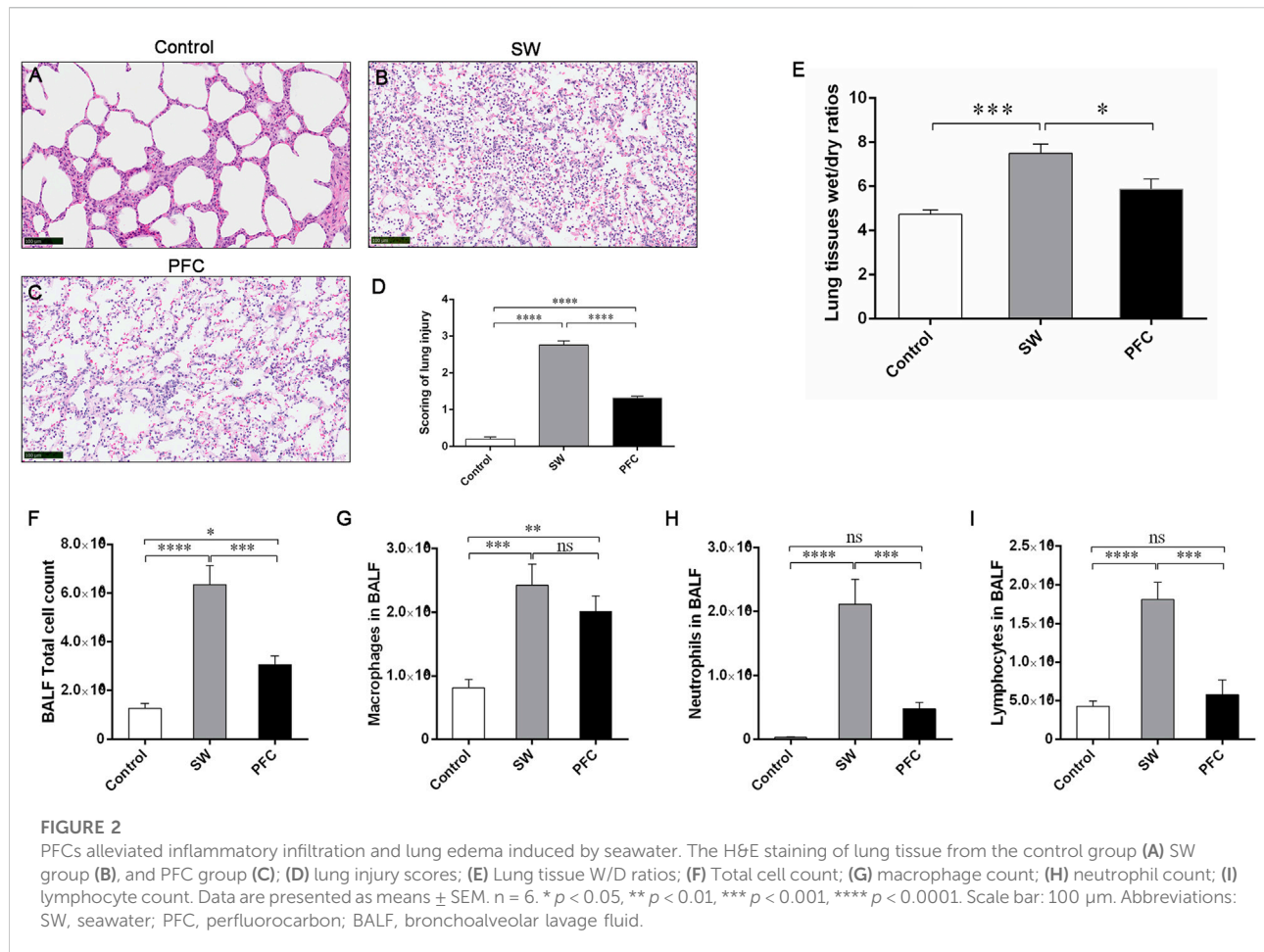
PFC administration downregulated the W/D ratios dramatically ($p < 0.05$) (Figure 2E).

PFCs improved barrier injuries induced by seawater

E-cadherin is an adherens junctional protein with functions in the regulation of the epithelial architecture, regulating the paracellular permeability. As shown by the representative immunofluorescence images of E-cadherin in Figure 3A, seawater induced obvious epithelial swelling, structural rupture, and thickening, in contrast to the control group, while PFC treatment tended to relieve the aforementioned changes.

PFCs improved type II alveolar epithelial (AT-II) and mitochondria damages induced by seawater

Ultrastructural analysis was performed using TEM. AT II cells from the SW group showed less microvilli (yellow arrows) and obvious swollen, fragmented mitochondria with disrupted cristae (red arrows), and PFC treatment alleviated the AT II injury, as shown in Figure 3B. Macrophages, one of the most important immune cells in respiratory system, showed damaged morphological mitochondria (red arrows), and red blood cells (green asterisks) infiltrated the alveoli in the SW group, while PFCs reversed the damage induced by seawater (Figure 3C).



Moreover, to elucidate the function of AT II, we performed ELISA to reveal the SP-A and SP-B concentrations in the BALF. Seawater induced a significant SP-A and SP-B deficiency, but PFCs increased the SP-B levels in the BALF dramatically ($p < 0.05$) (Figures 3D, E).

PFCs upregulated HO-1 and NRF1 and downregulated NLRP3 inflammasome levels

We employed qRT-PCR to quantify the mRNA expression levels of NRF1, HO-1, and NLRP3 inflammasomes. The PFC treatment increased the NRF1 and HO-1 expression levels and decreased NLRP3 expression levels compared with those in the control group and SW group ($p < 0.05$). Furthermore, the mRNA expression levels of caspase-1, IL-1 β , and IL-18 were dramatically elevated after a seawater challenge, while PFC treatment significantly reversed these changes ($p < 0.05$) (Figure 4A). The results suggest that PFCs downregulated the NLRP3 inflammasomes as well as their downstream molecules and upregulated HO-1 and NRF1.

To further explore the mechanisms underlying PFCs' therapeutic effects, we performed immunohistochemistry staining to detect the expression of HO-1, NRF1 and NLRP3 inflammasomes in lung tissues. We observed fewer HO-1-positive cells and NRF1-positive cells and more NLRP3 inflammasome-positive cells in the lung tissues of the SW group, while PFC treatment significantly reversed the HO-1, NRF1 and NLRP3 inflammasome expression induced by seawater (Figure 4B).

Discussion

Drowning is one of the three major causes of death from unintentional injury in the world [26]. The lack of effective treatments is the main cause of death from drowning [2]. Seeking new drugs and methods to treat SD-ALI is important. Previous studies found that PFCs were effective in improving oxygenation in animals with lung injury and hypoxia, with the therapeutic effect mainly being ascribed to anti-inflammation and anti-oxidative stress effect by NF- κ B pathway [18, 27, 28]. Our study established a SD-ALI model that fulfilled the standard for acute lung injury models updated in 2021 by the American

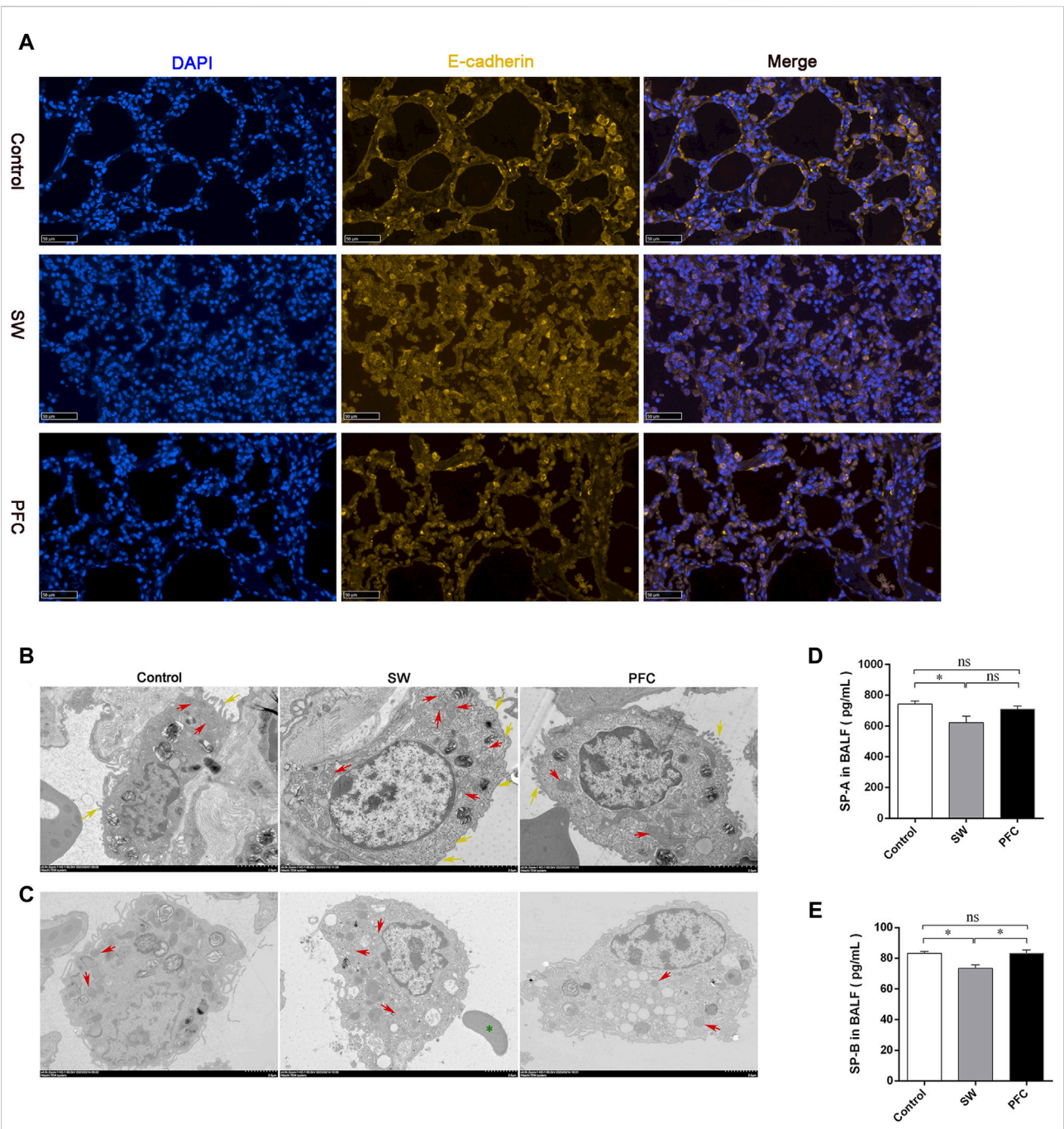
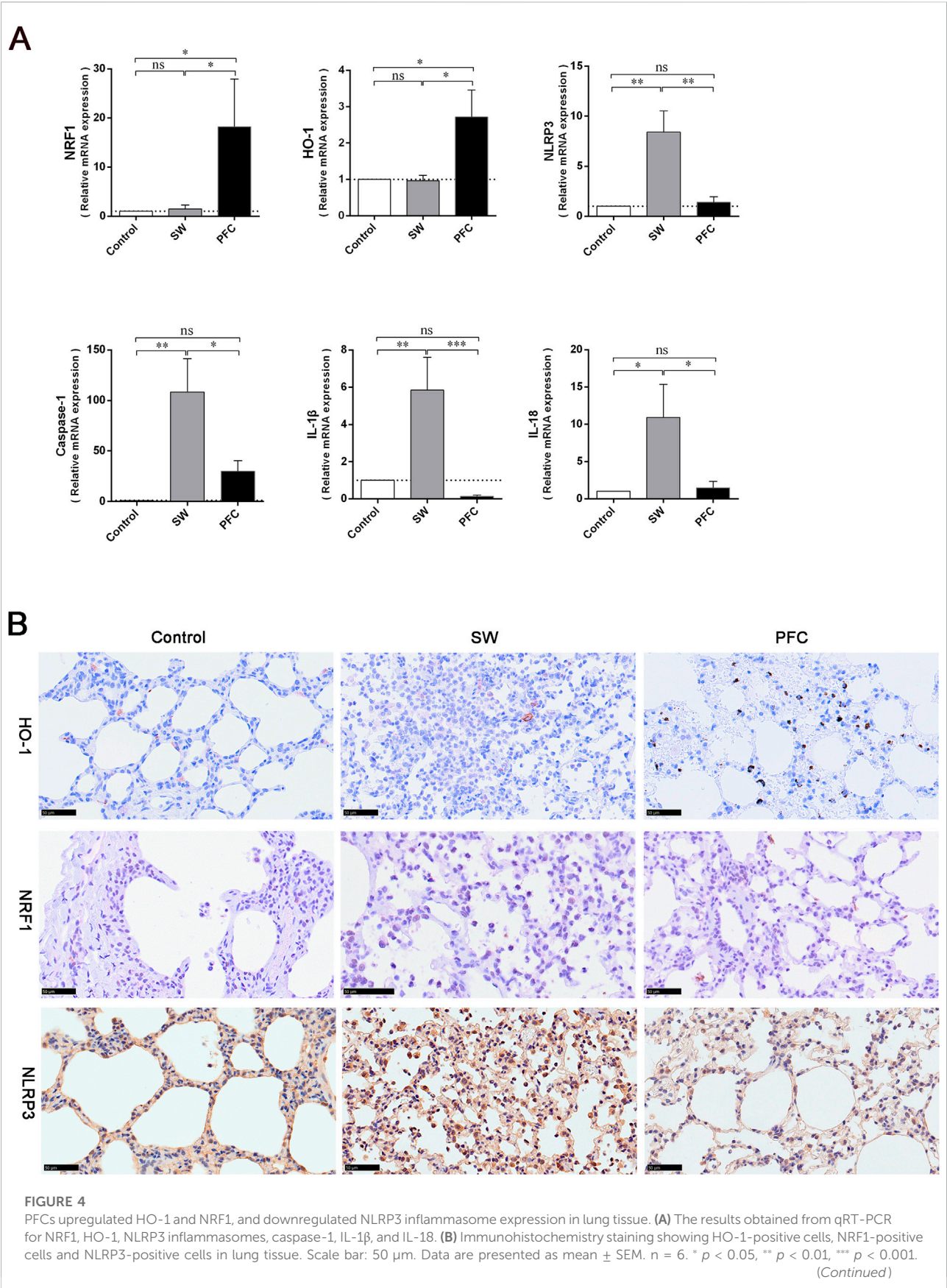
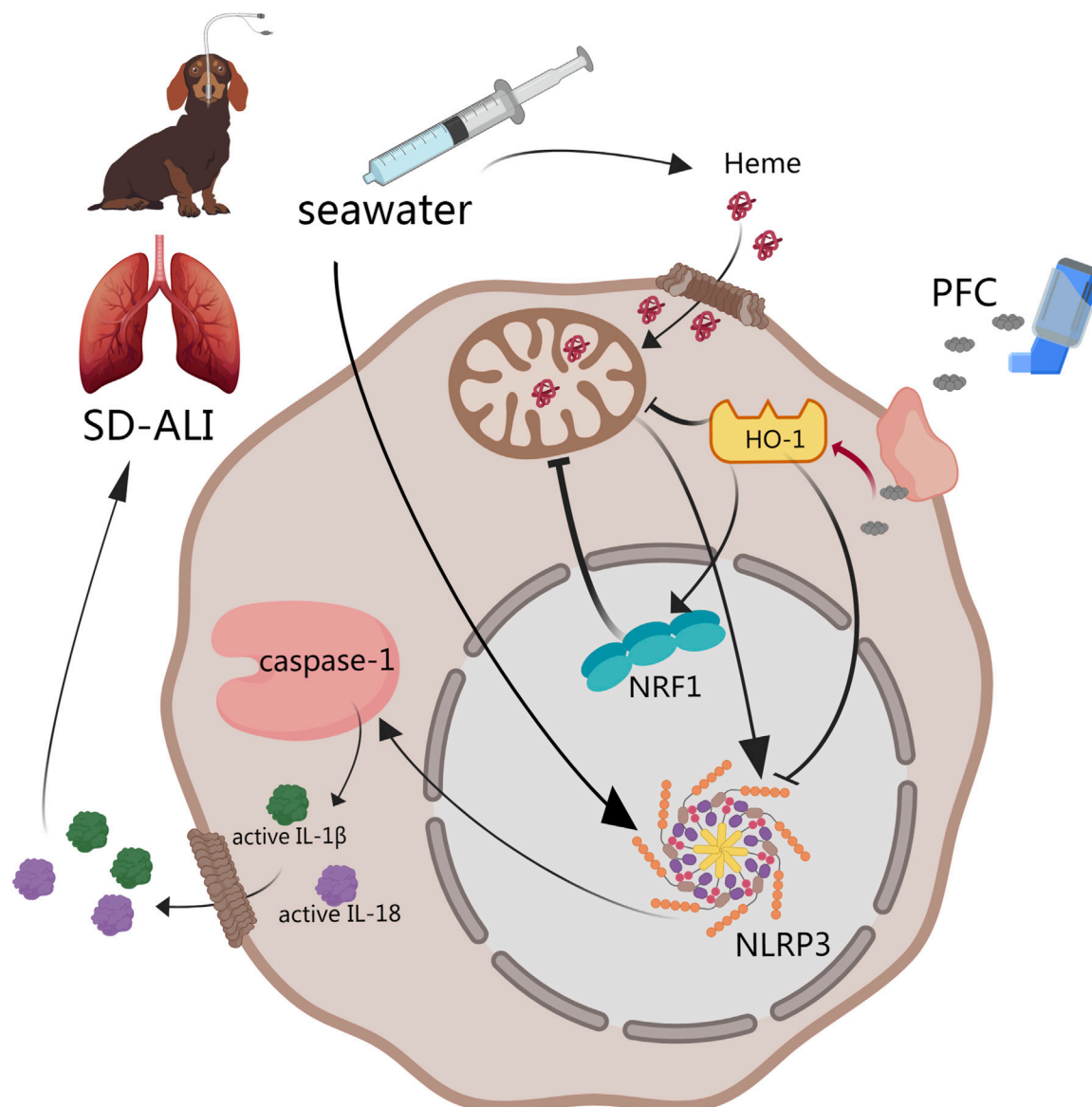


FIGURE 3
PFCs improved lung barrier injury and mitochondria morphological alterations induced by seawater. **(A)** The lung tissue is presented by immunofluorescence. Blue: nuclear staining (DAPI); yellow: E-cadherin. Scale bar: 50 μ m. **(B)** Mitochondria TEM images of type II alveolar epithelial cells after treatment with seawater and seawater + PFC. Red arrows: swollen and damaged morphological mitochondria; yellow arrows: microvilli. Scale bar: 2 μ m. **(C)** Mitochondria TEM images of macrophages after treatment with seawater and seawater + PFC. Red arrows: swollen and damaged morphological mitochondria; green asterisks: red blood cell. Scale bar: 2 μ m. **(D)** SP-A protein levels in BALF; **(E)** SP-B protein levels in BALF. Data are presented as mean \pm SEM. n = 6. * $p < 0.05$. Abbreviations: SW, seawater; PFC, Perfluorocarbon; DAPI, 4',6-diamidino-2'-phenylindole; TEM, transmission electron microscopy; SP-A, pulmonary surfactant A; SP-B, pulmonary surfactant B; BALF, bronchoalveolar lavage fluid.



Abbreviations: SW, seawater; PFC, perfluorocarbon; NRF1, nuclear respiratory factor-1; HO-1, heme oxygenase-1; NLRP3, NOD-like-receptor family pyrin domain-containing-3; IL-1 β , interleukin-1 β ; IL-18, interleukin-18.



Abstract of our work. PFCs could downregulate NLRP3 inflammasome activation by the HO-1/NRF1 pathway and then decrease the release of mature IL-1 β and IL-18 to alleviate acute lung injury induced by seawater. ① HO-1 may directly downregulate NLRP3 inflammasome gene expression. ② NRF1 may deactivate NLRP3 inflammasomes through mitochondrial quality control. Black line: pathway described in previous study. Red line: results obtained from our study. Abbreviations: SD-ALI, seawater-drowning-induced acute lung injury; PFC, perfluorocarbon; NRF1, nuclear respiratory factor-1; HO-1, heme oxygenase-1; NLRP3, NOD-like-receptor family pyrin domain-containing-3; IL-1 β , interleukin-1 β ; IL-18, interleukin-18.

Thoracic Society (ATS) [29], and it was the first time that dogs were used as SD-ALI model animals. The physiological structure characteristics and organ sizes of dogs are similar to those of humans, including the pulmonary, cardiovascular and cerebrovascular, and visual organs, which means they are suitable for the research and application of physical interventional therapy and intervention. The SD-ALI model showed significant pathological damage, a high W/D ratio, barrier damage and inflammatory cell infiltration. The results of our study showed that treatment with PFCs could ameliorate seawater-drowning-induced lung edema, barrier damage and inflammatory infiltration. The protective mechanism may involve the inhibition of NLRP3 activation via the HO-1/NRF1 pathway (Figure 5). To the best of our knowledge, this was the first time the effect of PFCs had been attributed to NLRP3 deactivation.

The blood–gas barrier, also known as the alveolar–capillary barrier, is the key functional element of the lung, serving as the site of oxygen and carbon dioxide exchange between the distal airspaces and the pulmonary vasculature [30]. West et al. previously described the stress failure of the blood–gas barrier in a rabbit lung using evidence from electron microscopy, with the concomitant translocation of red blood cells into the interstitium and/or airspaces [31]. The destruction of the blood–gas barrier could induce a perturbation in the fluid balance and result in pulmonary edema or acute lung injury [32]. The infection of alveolar epithelial cells and endothelial cells with severe acute respiratory syndrome coronavirus 2 (SARS-CoV-2) triggers an inflammatory response at the blood–gas barrier, inducing the release of IL-1 β , interleukin-6 (IL-6), and tumor necrosis factor- α (TNF- α), leading to the disintegration and thickening of the blood–gas barrier [33]. We established SD-ALI canine models with hypoxemia, hypercapnia, and acidism, which indicated the dysfunction of the blood–gas barrier. PFCs were administrated by inhalation, which can work immediately and directly on the lung. We then observed morphological changes in the blood–gas barrier by the immunofluorescence staining of lung tissue, characterized as epithelial swelling, structural rupture, and thickening. Our work demonstrated that PFC administration significantly improved the lung barrier structure and oxygenation. Moreover, PFCs could reduce injury to AT II cells, which produce and release pulmonary surfactant to maintain alveolar surface tension.

Our study attempted to visualize the structure of the pulmonary alveoli using pCLE in a living body. The pCLE technique uses a laser wavelength that mainly allows for the visualization of elastic fibers in lung tissue. Many studies have been conducted to assess the applicability of pCLE in central neoplasms, diffuse parenchymal lung disease, lung emphysema, pneumonia, acute lung injury, etc. [34–38]. Our study visualized the changes in images that occurred under acute

lung injury induced by seawater drowning in canine models, characterized by an increased density of elastic structures, and large drops of intra-alveolar secretions compared with the control group and PFC group, which were also supported by quantitative analysis using the VAI. The VAI may help us to assess the air content of lung tissue. To the best of our knowledge, this is the first pCLE image description and quantitative analysis of acute lung injury induced by seawater drowning.

Inflammatory responses are important mechanisms of SD-ALI. We found substantial inflammatory infiltrations in lung tissues from the SW group. Previous studies have found that seawater can increase the production of pro-inflammatory cytokines, including IL-6, interleukin-10 (IL-10), IL-1 β , and TNF- α , *in vivo* and *in vitro* [39–41]. We found that seawater challenge upregulated IL-1 β and IL-18. Moreover, the vaporization of PFCs could alleviate inflammatory cell infiltration and reduce the expression of IL-1 β and IL-18 in lung tissue. NLRP3 inflammasomes are cytoplasmic high-molecular-weight protein platforms of caspase-1 activation in response to microbial invasion and damage signals and have been found to be activated in macrophages and AT II cells by a wide spectrum of stimuli, including seawater [42]. The formation of these protein complexes activates caspase-1, which is involved in the maturation of the proinflammatory cytokines IL-1 β and IL-18 into their biologically active forms [42]. The regulation of the NLRP3 inflammasome activation state is a promising target for neuronal necroptosis, osteoarthritis, and respiratory system diseases [43, 44]. Based on the above, we hypothesized that the therapeutic effect of PFCs may be achieved through NLRP3 inflammasomes. To elucidate whether PFCs influence the seawater-induced activation of NLRP3 inflammasomes, we confirmed the seawater-induced activation of NLRP3 inflammasomes in lung tissue based on their mRNA and protein levels, which were consistent with previous studies [21]. Then, we found that PFC administration significantly deactivated NLRP3 inflammasomes, which was verified by means of qRT-PCR and immunohistochemistry. Moreover, PFC vaporization also downregulated caspase-1, a signal factor downstream of NLRP3 and the key molecule linking NLRP3 inflammasome activation and IL-1 β and IL-18 maturation.

Knowing that NLRP3 inflammasome activation is regulated by multiple complicated positive and/or negative regulatory pathways providing upstream signals [42, 45], we attempted to find pathways involved in this activity. HO-1 is a rate-limiting enzyme of heme degradation that catalyzes the degradation of free heme to biliverdin, ferrous iron, and carbon monoxide [46]. HO-1 is reported to have antioxidant and anti-inflammatory effects in acute lung injury, and also can decrease NLRP3 inflammasome deactivation induced by heme [39, 43, 44, 47, 48]. NRF1 is a phosphorylated nuclear protein

that functions as a transcription factor, activating the expression of key metabolic genes regulating cellular growth and nuclear genes required for respiration, heme biosynthesis, and mitochondrial DNA transcription and replication [49]. However, the function of NRF1 has not been fully elucidated. HO-1 regulates mitochondrial biogenesis and activates the redox-sensitive transcriptional program for mitochondrial quality control through NRF1. This pathway is implicated in the mitigation of various injuries, including organ fibrosis, ischemic and drug-induced cardiomyopathy, acute lung injury, and ARDS [48, 50]. A previous study reported that mitochondrial damage and dysfunction could promote epithelial barrier damage through calcium dysregulation, energy failure, apoptosis, and the loss of heme homeostasis [51, 52]. Our work observed mitochondrial damage in the SW group via TEM, characterized by obviously swollen, fragmented mitochondria with disrupted cristae, suggesting that the HO-1/NRF1 pathway may participate in mitochondrial quality control during the pathophysiological process of SD-ALI. NRF1 may directly downregulate NLRP3 inflammasome gene expression within the nucleus or promote mitochondrial quality control to influence heme metabolism. The elaboration of the HO-1/NRF1 pathway to NLRP3 inflammasome activation needs further investigation.

In summary, we provided evidence that the inhalation of vaporized PFCs suppressed SD-ALI in canine models, alleviated hypoxemia and blood-gas barrier injuries, and reduced inflammatory infiltration and cytokine release. The mechanisms of PFCs' therapeutic effects may be attributed to the regulation of NLRP3 inflammasomes' activation via the HO-1/NRF1 pathway. This study offers a meaningful exploration of PFCs' therapeutic mechanisms *in vivo*.

Author contributions

Conceptualization, L-AC; methodology, ZY and C-SL; software, C-CS, J-XL, J-BR; validation, ZY, Z-XL, and C-SL; formal

analysis, C-CS, Z-RZ, J-GM, J-XL; investigation, C-CS, Z-RZ; resources, L-AC; data curation, J-GM, J-XL, X-QM, Z-FM; writing—original draft preparation, CC-S, Z-RZ; writing—review and editing, L-AC, C-SL, J-XL, J-GM, X-QM, Z-FM, J-BR, ZY, Z-XL; visualization, Z-RZ, J-XL; supervision, L-AC; project administration, L-AC. All authors contributed to the article and approved the submitted version.

Data availability statement

The datasets presented in this article are not readily available because confidentiality period lasts for 10 years. Requests to access the datasets should be directed to suellen1988@163.com.

Ethics statement

The animal study was approved by the Experimental Animal Care Committee of the PLA General hospital. The study was conducted in accordance with the local legislation and institutional requirements.

Funding

The author(s) declare that financial support was received for the research, authorship, and/or publication of this article. This research was funded by Beijing Municipal Health Commission, grant number 2020-1-5011.

Conflict of interest

The authors declare that the research was conducted in the absence of any commercial or financial relationships that could be construed as a potential conflict of interest.

References

1. Tyler MD, Richards DB, Reske-Nielsen C, Saghafi O, Morse EA, Carey R, et al. The epidemiology of drowning in low- and middle-income countries: a systematic review. *BMC public health* (2017) 17(1):413. doi:10.1186/s12889-017-4239-2
2. Gregorakos L, Markou N, Psalida V, Kanakaki M, Alexopoulou A, Sotiriou E, et al. Near-drowning: clinical course of lung injury in adults. *Lung* (2009) 187(2): 93–7. doi:10.1007/s00408-008-9132-4
3. Abelairas-Gómez C, Tipton MJ, González-Salvado V, Bierens J. Drowning: epidemiology, prevention, pathophysiology, resuscitation, and hospital treatment. *Emergencias : revista de la Sociedad Española de Medicina de Emergencias* (2019) 31(4):270–80.
4. Li JH, Xu M, Xie XY, Fan QX, Mu DG, Zhang Y, et al. Tanshinone IIA suppresses lung injury and apoptosis, and modulates protein kinase B and extracellular signal-regulated protein kinase pathways in rats challenged with seawater exposure. *Clin Exp Pharmacol Physiol* (2011) 38(4):269–77. doi:10.1111/j.1440-1681.2011.05498.x
5. Zhang M, Jin F. 1 α ,25-Dihydroxyvitamin D3 ameliorates seawater aspiration-induced lung injury by inhibiting the translocation of NF- κ B and RhoA. *Inflammation* (2017) 40(3):832–9. doi:10.1007/s10753-017-0527-3
6. Liu W, Dong M, Bo L, Li C, Liu Q, Li Y, et al. Epigallocatechin-3-gallate ameliorates seawater aspiration-induced acute lung injury via regulating inflammatory cytokines and inhibiting JAK/STAT1 pathway in rats. *Mediators Inflamm* (2014) 2014:1–12. doi:10.1155/2014/612593
7. Zhang M, Xie L. MicroRNA-200c-3p regulates seawater-induced acute lung injury via ANGII and ACE2/ANG1-7 pathways. *Exp Ther Med* (2023) 26(6):582. doi:10.3892/etm.2023.12281
8. Mokrá D. Acute lung injury - from pathophysiology to treatment. *Physiol Res* (2020) 69(Suppl. 3):S353–S366. doi:10.33549/physiolres.934602
9. Jin F, Li C. Seawater-drowning-induced acute lung injury: from molecular mechanisms to potential treatments. *Exp Ther Med* (2017) 13(6):2591–8. doi:10.3892/etm.2017.4302

10. Khalighi Z, Rahmani A, Cheraghi J, Ahmadi MR, Soleimannejad K, Asadollahi R, et al. Perfluorocarbon attenuates inflammatory cytokines, oxidative stress and histopathologic changes in paraquat-induced acute lung injury in rats. *Environ Toxicol Pharmacol* (2016) 42:9–15. doi:10.1016/j.etap.2015.12.002
11. Chang N, Won H, Jung C, Kim S, Eun H, Kim Y. Behaviors of perfluorocarbon emulsion during dissolution of oxide layers. *Molecules (Basel, Switzerland)* (2021) 26(5):1329. doi:10.3390/molecules26051329
12. Arni S, Necati C, Maeyashiki T, Opitz I, Inci I. Perfluorocarbon-based oxygen carriers and subnormothermic lung machine perfusion decrease production of pro-inflammatory mediators. *Cells* (2021) 10(9):2249. doi:10.3390/cells10092249
13. Wei F, Wen S, Wu H, Ma L, Huang Y, Yang L. Partial liquid ventilation-induced mild hypothermia improves the lung function and alleviates the inflammatory response during acute respiratory distress syndrome in canines. *Biomed Pharmacother* (2019) 118:109344. doi:10.1016/j.biopha.2019.109344
14. Haque A, Scultetus AH, Arnaud F, Dickson LJ, Chun S, McNamee G, et al. The emulsified PFC Oxycyte® improved oxygen content and lung injury score in a swine model of oleic acid lung injury (OALI). *Lung* (2016) 194(6):945–57. doi:10.1007/s00408-016-9941-9
15. Hou S, Ding H, Lv Q, Yin X, Song J, Landén NX, et al. Therapeutic effect of intravenous infusion of perfluorocarbon emulsion on LPS-induced acute lung injury in rats. *PLoS One* (2014) 9(1):e87826. doi:10.1371/journal.pone.0087826
16. Xu Y, Wu T, Wang P, Liang ZX, Shi SS, Xu SF, et al. Perfluorocarbon protects against lipopolysaccharide-induced apoptosis of endothelial cells in pulmonary microvessels. *Bull Exp Biol Med* (2021) 170(4):410–4. doi:10.1007/s10517-021-05077-8
17. Wang X, Zhang J, Li X, Liu Y, Yang H, Zhao X, et al. Sustained improvement of gas exchange and lung mechanics by vaporized perfluorocarbon inhalation in piglet acute lung injury model. *Clin Respir J* (2014) 8(2):160–6. doi:10.1111/crj.12053
18. Zhang Z, Liang Z, Li H, Li C, Yang Z, Li Y, et al. Perfluorocarbon reduces cell damage from blast injury by inhibiting signal paths of NF- κ B, MAPK and Bcl-2/Bax signaling pathway in A549 cells. *PLoS One* (2017) 12(3):e0173884. doi:10.1371/journal.pone.0173884
19. Bickenbach J, Czaplik M, Dembinski R, Pelosi P, Schroeder W, Marx G, et al. *In vivo* microscopy in a porcine model of acute lung injury. *Respir Physiol Neurobiol* (2010) 172(3):192–200. doi:10.1016/j.resp.2010.05.021
20. Vasilev IV, Mamenko IS, Makarova AV, Sokolova OP, Lee VF, Mortada MM, et al. Probe-based confocal laser endomicroscopy in COVID-19. *Adv Respir Med* (2021) 89(4):456–9. doi:10.5603/ARM.a2021.0067
21. Zhang L, Kong D, Huang J, Wang Q, Shao L. The therapeutic effect and the possible mechanism of C-phycoerythrin in lipopolysaccharide and seawater-induced acute lung injury. *Drug Des Dev Ther* (2022) 16:1025–40. doi:10.2147/dddt.S347772
22. Percie du Sert N, Hurst V, Ahluwalia A, Alam S, Avey MT, Baker M, et al. The ARRIVE guidelines 2.0: updated guidelines for reporting animal research. *PLoS Biol* (2020) 18(7):e3000410. doi:10.1371/journal.pbio.3000410
23. Czaplik M, Rossaint R, Koch E, Fahlenkamp A, Schröder W, Pelosi P, et al. Methods for quantitative evaluation of alveolar structure during *in vivo* microscopy. *Respir Physiol Neurobiol* (2011) 176(3):123–9. doi:10.1016/j.resp.2011.02.009
24. Xiang GA, Zhang YD, Su CC, Ma YQ, Li YM, Zhou X, et al. Dynamic changes of mononuclear phagocytes in circulating, pulmonary alveolar and interstitial compartments in a mouse model of experimental silicosis. *Inhalation Toxicol* (2016) 28(9):393–402. doi:10.1080/08958378.2016.1188186
25. Quintel M, Heine M, Hirschl RB, Tillmanns R, Wessendorf V. Effects of partial liquid ventilation on lung injury in a model of acute respiratory failure: a histologic and morphometric analysis. *Crit Care Med* (1998) 26(5):833–43. doi:10.1097/00003246-199805000-00013
26. Engel SC. Drowning episodes: prevention and resuscitation tips. *J Fam Pract* (2015) 64(2):E1–6.
27. Kakaie N, Amirian R, Azadi M, Mohammadi G, Izadi Z. Perfluorocarbons: a perspective of theranostic applications and challenges. *Front Bioeng Biotechnol* (2023) 11:1115254. doi:10.3389/fbioe.2023.1115254
28. Zhang Z, Li H, Liang Z, Li C, Yang Z, Li Y, et al. Vaporized perfluorocarbon inhalation attenuates primary blast lung injury in canines by inhibiting mitogen-activated protein kinase/nuclear factor- κ B activation and inducing nuclear factor, erythroid 2 like 2 pathway. *Toxicol Lett* (2020) 319:49–57. doi:10.1016/j.toxlet.2019.10.019
29. Kulkarni HS, Lee JS, Bastarache JA, Kuebler WM, Downey GP, Albaiceta GM, et al. Update on the features and measurements of experimental acute lung injury in animals: an official American thoracic society workshop report. *Am J Respir Cell Mol Biol* (2022) 66(2):e1–e14. doi:10.1165/rcmb.2021-0531ST
30. Leiby KL, Raredon MSB, Niklason LE. Bioengineering the blood-gas barrier. *Compr Physiol* (2020) 10(2):415–52. doi:10.1002/cphy.c190026
31. Tsukimoto K, Mathieu-Costello O, Prediletto R, Elliott AR, West JB. Ultrastructural appearances of pulmonary capillaries at high transmural pressures. *J Appl Physiol* (1991) 71(2):573–82. doi:10.1152/jappl.1991.71.2.573
32. Haeger SM, Liu X, Han X, McNeil JB, Oshima K, McMurtry SA, et al. Epithelial heparan sulfate contributes to alveolar barrier function and is shed during lung injury. *Am J Respir Cell Mol Biol* (2018) 59(3):363–74. doi:10.1165/rcmb.2017-0428OC
33. Shirvaliloo M. The blood-gas barrier in COVID-19: an overview of the effects of SARS-CoV-2 infection on the alveolar epithelial and endothelial cells of the lung. *Tissue barriers* (2021) 9(4):1937013. doi:10.1080/21688370.2021.1937013
34. Salaün M, Guisier F, Dominique S, Genevois A, Jounieaux V, Bergot E, et al. *In vivo* probe-based confocal laser endomicroscopy in chronic interstitial lung diseases: specific descriptors and correlation with chest CT. *Respirology* (2019) 24(8):783–91. doi:10.1111/resp.13507
35. Kennedy GT, Azari FS, Bernstein E, Nadeem B, Chang A, Segil A, et al. Targeted detection of cancer cells during biopsy allows real-time diagnosis of pulmonary nodules. *Eur J Nucl Med Mol Imaging* (2022) 49(12):4194–204. doi:10.1007/s00259-022-05868-9
36. Lesur O, Chagnon F, Lebel R, Lepage M. *In vivo* endomicroscopy of lung injury and repair in ARDS: potential added value to current imaging. *J Clin Med* (2019) 8(8):1197. doi:10.3390/jcm8081197
37. Silbernagel E, Stacher-Priehse E, Dinkel J, Stepp H, Gesierich W, Lindner M, et al. Bronchoscopic probe-based confocal laser endomicroscopy to diagnose diffuse parenchymal lung diseases. *Sarcoidosis Vasc Diffuse Lung Dis* (2022) 39(2):e2022016. doi:10.36141/svld.v39i2.11280
38. Danilevskaya O, Averyanov A, Lesnyak V, Chernyaev A, Sorokina A. Confocal laser endomicroscopy for diagnosis and monitoring of pulmonary alveolar proteinosis. *J bronchology Interv pulmonology* (2015) 22(1):33–40. doi:10.1097/lbr.0000000000000126
39. Sun XQ, Wu C, Qiu YB, Wu YX, Chen JL, Huang JF, et al. Heme oxygenase-1 attenuates seawater drowning-induced acute lung injury through a reduction in inflammation and oxidative stress. *Int immunopharmacology* (2019) 74:105634. doi:10.1016/j.intimp.2019.05.019
40. Li C, Liu M, Bo L, Liu W, Liu Q, Chen X, et al. NFAT5 participates in seawater inhalation-induced acute lung injury via modulation of NF- κ B activity. *Mol Med Rep* (2016) 14(6):5033–40. doi:10.3892/mmr.2016.5860
41. Ma J, Wang Y, Wu Q, Chen X, Wang J, Yang L. Seawater immersion aggravates burn-associated lung injury and inflammatory and oxidative-stress responses. *Burns* (2017) 43(5):1011–20. doi:10.1016/j.burns.2017.01.028
42. Paik S, Kim JK, Silwal P, Sasakawa C, Jo EK. An update on the regulatory mechanisms of NLRP3 inflammasome activation. *Cell Mol Immunol* (2021) 18(5):1141–60. doi:10.1038/s41423-021-00670-3
43. Chen Z, Zhong H, Wei J, Lin S, Zong Z, Gong F, et al. Inhibition of Nrf2/HO-1 signaling leads to increased activation of the NLRP3 inflammasome in osteoarthritis. *Arthritis Res Ther* (2019) 21(1):300. doi:10.1186/s13075-019-2085-6
44. Liu Z, Cheng P, Feng T, Xie Z, Yang M, Chen Z, et al. Nrf2/HO-1 blocks TXNIP/NLRP3 interaction via elimination of ROS in oxygen-glucose deprivation-induced neuronal necroptosis. *Brain Res* (2023) 1817:148482. doi:10.1016/j.brainres.2023.148482
45. Salgar S, Bolivar BE, Flanagan JM, Anum SJ, Bouchier-Hayes L. The NLRP3 inflammasome fires up heme-induced inflammation in hemolytic conditions. *Translational Res* (2023) 252:34–44. doi:10.1016/j.trsl.2022.08.011
46. Facchinetti MM. Heme-Oxygenase-1. *Antioxid Redox signaling* (2020) 32(17):1239–42. doi:10.1089/ars.2020.8065
47. Cheng X, Yin M, Sun X, Zhang Z, Yao X, Liu H, et al. Hemin attenuated LPS-induced acute lung injury in mice via protecting pulmonary epithelial barrier and regulating HO-1/Nlrp3-Mediated pyroptosis. *Shock (Augusta, Ga)* (2023) 59(5):744–53. doi:10.1097/shk.0000000000002101
48. Shi J, Yu J, Zhang Y, Wu L, Dong S, Wu L, et al. PI3K/Akt pathway-mediated HO-1 induction regulates mitochondrial quality control and attenuates endotoxin-induced acute lung injury. *Lab Invest* (2019) 99(12):1795–809. doi:10.1038/s41374-019-0286-x
49. Zhao T, Zhang J, Lei H, Meng Y, Cheng H, Zhao Y, et al. NRF1-mediated mitochondrial biogenesis antagonizes innate antiviral immunity. *EMBO J* (2023) 42(16):e113258. doi:10.15252/embj.2022113258
50. Suliman HB, Healy Z, Zobi F, Kraft BD, Welty-Wolf K, Smith J, et al. Nuclear respiratory factor-1 negatively regulates TGF- β 1 and attenuates pulmonary fibrosis. *iScience* (2022) 25(1):103535. doi:10.1016/j.isci.2021.103535
51. Li N, Liu B, Xiong R, Li G, Wang B, Geng Q. HDAC3 deficiency protects against acute lung injury by maintaining epithelial barrier integrity through preserving mitochondrial quality control. *Redox Biol* (2023) 63:102746. doi:10.1016/j.redox.2023.102746
52. Schumacker PT, Gillespie MN, Nakahira K, Choi AM, Crouser ED, Piantadosi CA, et al. Mitochondria in lung biology and pathology: more than just a powerhouse. *Am J Physiol Lung Cell Mol Physiol* (2014) 306(11):L962–74. doi:10.1152/ajplung.00073.2014

Experimental Biology & Medicine Conference

Orlando, FL - October 13 -16, 2024

Please visit

**exbiomed
con.org**

or scan the QR
code for more
info.



Keynote Lecturers



Namandjè Bumpus, Ph.D.

Chief Scientist -
US Food and Drug Administration

**Advancing Emerging Technologies
in Regulatory Science**



Michael Friedlander, Ph.D.

Vice President - Health Sciences and
Technology at Virginia Tech

All events will take place at
the Embassy Suites by
Hilton, Orlando Lake
Buena Vista South

Cardiovascular



Delphine Gomez, Ph.D.

University of Pittsburgh



Karen Hirschi, Ph.D.

University of Virginia



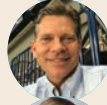
Jay Humphrey, Ph.D.

Yale University



Ali J. Marian, M.D.

The University of Texas Health
Science Center at Houston



Joseph Miano, Ph.D.

Medical College of Georgia



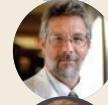
**Dianna Milewicz, M.D.,
Ph.D.**

University of Texas
Health Science Center Houston



Robert Schwartz, Ph.D.

University of Houston



George Taffet, M.D.

Baylor College of Medicine



David Zawieja, Ph.D.

Texas A&M University
Health Science Center

Neuroscience



Lique Coolen, Ph.D.

Kent State university



Michael Fehlings, M.D.

University of Toronto



Susan Harkema, Ph.D.

University of Louisville



Maria Lehtinen, Ph.D.

Harvard University



Fang Liu, Ph.D.

NCTR/US Food and Drug
Administration



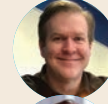
Agnes Luo, Ph.D.

University Cincinnati



Mervyn Maze, MBChB

University of California
San Francisco



Dorian McGavern, Ph.D.

National Institute of Neurological
Disorders and Stroke



**Vesna Jevtovic-Todorovic,
M.D., Ph.D.**

University of Colorado
School of Medicine

Regenerative Medicine



Arnold I. Caplan, Ph.D.

Case Western Reserve



Jian Feng, Ph.D.

State University of New York
at Buffalo



Joshua Hare, M.D.

University of Miami



Karen Hasty, Ph.D.

University of Tennessee Health
Science Center



Rajasingh Johnson, Ph.D.

University of Tennessee
Health Science Center



Y. James Kang, DVM, Ph.D.

Sichuan University



Kwang-Soo Kim, Ph.D.

Harvard University



Joanne Kurtzberg, M.D.

Duke University



Jun Wu, Ph.D.

UT Southwestern

Trainees



Justin Boyd, Ph.D.

Vaxxinity



Udayan Apte, Ph.D.

U of Kansas Medical Center



Ram Kumar, Ph.D.

U of Kansas Medical Center

And More

**Career Development
Short Talks
Poster Sessions
Member Blitz**



Scope

Experimental Biology and Medicine (EBM) is a global, peer-reviewed journal dedicated to the publication of multidisciplinary and interdisciplinary research in the biomedical sciences. The journal covers the spectrum of translational research from T0, basic research, to T4, population health. Articles in EBM represent cutting edge research at the overlapping junctions of the biological, physical and engineering sciences that impact upon the health and welfare of the world's population. EBM is particularly appropriate for publication of papers that are multidisciplinary in nature, are of potential interest to a wide audience, and represent experimental medicine in the broadest sense of the term. However, manuscripts reporting novel findings on any topic in the realm of experimental biology and medicine are most welcome.

EBM publishes Research, Reviews, Mini Reviews, and Brief Communications in the following categories.

- Anatomy/Pathology
- Artificial Intelligence/
Machine Learning Applications
to Biomedical Research
- Biochemistry and Molecular Biology
- Bioimaging
- Biomedical Engineering
- Bionanoscience
- Cell and Developmental Biology
- Clinical Trials
- Endocrinology and Nutrition
- Environmental Health/Biomarkers/
Precision Medicine
- Genomics, Proteomics, and
Bioinformatics
- Immunology/Microbiology/Virology
- Mechanisms of Aging
- Neuroscience
- Pharmacology and Toxicology
- Physiology and Pathophysiology
- Population Health
- Stem Cell Biology
- Structural Biology
- Synthetic Biology
- Systems Biology and
Microphysiological Systems
- Translational Research

Submit your work to Experimental Biology and Medicine at
ebm-journal.org/submission

More information
ebm-journal.org/journals/experimental-biology-and-medicine



**EBM is the official journal of the Society
for Experimental Biology and Medicine**

Led by Dr Steven Goodman, Experimental
Biology and Medicine (EBM) is a global, peer-
reviewed journal dedicated to the publication of
multidisciplinary and interdisciplinary research in
the biomedical sciences.

Discover more of our Special Issues

See more →

Contact

development@ebm-journal.org

See more

ebm-journal.org

publishingpartnerships.frontiersin.org/our-partners

